Extension of the Euler/Euler formalism for numerical simulations of fluidized beds of Geldart A particles

Jean-François Parmentier

THÈSE

En vue de l'obtention du

DOCTORAT DE L'UNIVERSITÉ DE TOULOUSE

Délivré par *Institut National Polytechnique de Toulouse*

Spécialité : *Dynamique des fluides*

Présentée et soutenue par J.-F. PARMENTIER

le 28 Juin 2010

Extension du formalisme Euler/Euler pour la simulation des lits fluidisés de particules du groupe A dans la classification de Geldart

Extension of the Euler/Euler formalism for numerical simulations of fluidized beds of Geldart A particles

---

JURY

Eric Climent	Examinateur
J.A.M. Kuipers	Rapporteur
Juan-David Llamas	Examinateur
Benoît Oesterlé	Examinateur
Olivier Simonin	Directeur de thèse
Sankaran Sundaresan	Rapporteur

École doctorale: Mécanique, Energétique, Génie Civil, Procédés (MEGeP)
Unité de recherche: Institut de Mécanique des Fluides de Toulouse (IMFT)
Directeur de thèse: Olivier Simonin
Encadrant TOTAL: Olivier Delsart

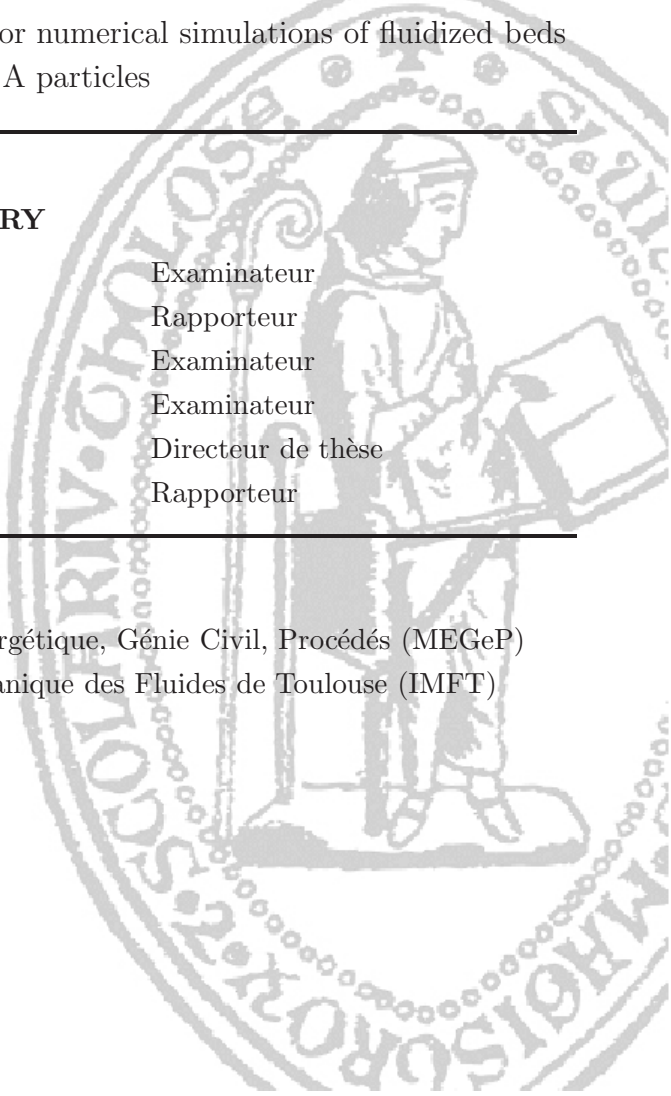

Contents

Remerciements

Ce travail a été effectué à l'IMFT, au sein du groupe PSC. Je voudrais ici remercier tous les acteurs qui y ont contribué.

Je remercie tout d'abord Olivier Simonin, mon directeur de thèse. J'ai eu la chance de profiter de ses connaissances scientifiques précises, ainsi que, et surtout, de sa démarche de chercheur. J'ai appris beaucoup à ses côtés et je lui en suis extrêmement reconnaissant. Je voudrais ensuite remercier l'équipe du CReG de Total. En particulier Olivier Delsart et Juan-David Llamas, avec qui j'ai apprécié travailler. Ils ont portés de l'intérêt à mon travail et leurs discussions m'ont permis de bien en comprendre le contexte industriel. Je remercie les Pr. Sundaresan et Pr. Kuipers pour avoir évalué mon manuscrit ainsi que tous les autres membres du jury d'avoir accepté de juger mon travail: Pr. Oesterlé, Pr. Climent et le Dr. Llamas. A l'IMFT rien ne fonctionnerait sans l'aide des services techniques, en particulier le service informatique et le service cosinus, que je remercie pour leur aide.

Tourne vite la page pour le grand jeu des remerciements ! ⇒

Grand jeu des remerciements

Amuse toi à relier les noms avec les bons remerciements ! Un seul remerciement par nom est autorisé (solution à la prochaine thèse.)

Adrien	•	•	pour tout ça tout ça, les tomates et les jeux de geek.
Ali	•	•	pour ne pas t'avoir trouvé à 14h.
Alice	•	•	pour le repas auquel tu vas m'inviter la semaine prochaine.
Arthur	•	•	pour ton tatouage d'extraterrestre.
Aurélien	•	•	pour avoir joué aux jeux du midi avec moi.
Dominique A.A.	•	•	pour avoir été MA stagiaire.
Dirk	•	•	pour avoir pu te présenter M.C.
Enrica	•	•	pour ta photo dont mon mari est jalouse.
Eric B.	•	•	pour tes conseils de bricolo pro.
Florence	•	•	pour ton estime égale des enfants et des chiens
Floflo	•	•	pour avoir testé mes 324 modifications de lois de traînée.
Gérard	•	•	zaï zaï zaï zaï.
Guillaume	•	•	pour avoir supporté mon caractère insupportable.
Hervé A.	•	•	un oscilloscope et des bons conseils.
Hervé	•	•	ma poel ! (ah ah ah, on ne te l'avais jamais faite celle la !)
Jérôme	•	•	pour ton pote qui l'a déjà fait en mieux.
Laurent	•	•	pour tout ça tout ça, les tomates et les voitures.
Magali	•	•	pour boom tchac.
Marco	•	•	pour ta bonne humeur quotidienne.
Marion L.	•	•	pour un magnifique four.
Marion P.	•	•	d'avoir nettoyé les kilos de fécule de pomme de terre.
M.C.	•	•	pourquoi je le remercie au fait ? ah oui, sinon il va se vexer.
Mehdi	•	•	pour la coiffure de Mr. Spock.
Micheline	•	•	pour la moustache, le casque et le glaive.
Mr. Tacos	•	•	d'étre venu me poser toutes tes questions.
Nico	•	•	pour tes frites de luxes.
Nicolix	•	•	parce que tu le vaux bien, guy.
Olivier P.	•	•	pour ton stagiaire Mathématica.
Olivier S.	•	•	qui ça ?
Renaud	•	•	pour toi yau de poêle.
Roel	•	•	pour avoir été une super cobureaute.
Romain	•	•	pour ta tolérance musicale.
Toi	•	•	car tu es le seul qui ne se moquait pas de moi pour l'aquagym !
Yannick	•	•	pour ton accueil et ton efficacité quand j'ai eu besoin de toi.
Zafer	•	•	*(inscris ici ce que tu veux)*

Résumé

Cette thèse porte sur l'amélioration du modèle à deux fluides utilisé pour simuler la fluidisation des particules de type Geldart A. L'attention est portée sur la surestimation de la hauteur du lit trouvée lors des simulations des lits bullants.

Le Chapitre 2 traite de l'approche statistique des écoulements gas-particules. Tout d'abord, les termes de collisions sont modifiés pour prendre complètement en compte les collisions induites par le cisaillement, dans le cas particulier d'un cisaillement simple. Le paramètre pertinent est alors le rapport

$$T^* = T \,/\, (\gamma\, a)^2 \tag{1}$$

où T est l'agitation des particules, a leur diamètre et γ le tau de cisaillement. Pour les valeurs élevées de l'agitation, les collisions sont majoritairement dues à l'agitation et les modèles standards sont applicables. Au contraire, pour les faibles agitations, les collisions sont dues au cisaillement et l'approche "quenched" doit être utilisée. En calculant explicitement les termes collisionnels comme des fonctions de T^*, les écoulements à forts et faibles nombres de Stokes peuvent être correctement prédits.

Les effets hydrodynamiques agissant lors des collisions des particules sont ensuite été étudiés. Le modèle local suggéré par Legendre et al. (2006), qui propose de modifier le coefficient de restitution des chocs, est intégré à l'échelle macroscopique dans le modèle à deux fluides. Les coefficients de restitutions apparaissants dans les termes de collisions deviennent des fonctions de

$$T_\beta = \frac{T}{V_\beta^2} \tag{2}$$

où $V_\beta = \frac{\beta}{2}\frac{a}{\tau_p}$ est la vitesse caractéristique décrivant l'effet hydrodynamique et β un paramètre mesuré par Legendre et al. (2006). Les résultats théoriques trouvés sont en bon accord avec les simulations lagrangiennes effectuées.

Enfin, les forces de van der Waals sont implémentées dans le modèle à deux fluides en utilisant la hiérarchie BBGKY. La conséquence directe et l'ajout d'un terme de pression

négative, P_c, à la pression particulaire totale:

$$P_c = -\alpha_p \rho_p \; \alpha_p g_0^b \; \frac{A}{m_p} \; \frac{1}{2} \; ln\left(\frac{d_p}{z_0}\right) \tag{3}$$

où A est la constante de Hamaker représentant l'intensité des forces, z_0 la distance interatomique, m_p la masse des particules et g_0^b une fonction de la α_p qui se comporte comme g_0

L'étude montre qu'aucun des phénomènes physiques identifiés n'est une explication plausible à la forte surestimation trouvée. En conséquence la suite de l'étude porte sur la manière dont sont résolues les équations du modèle à deux fluides, et en particulier sur l'influence de l'usage d'un maillage grossier.

Le Chapitre 3 montre que la convergence en maillage est obtenue pour de petites tailles adimensionnelles de maille Δ_G^*, où Δ_G^* est définie par:

$$\Delta_G^* = \frac{\Delta_G}{L} \; \left(\frac{L}{\tau_p^0 \, U_f}\right)^{\frac{1}{2}} \tag{4}$$

Le formalisme filtré est ensuite appliqué au modèle à deux fluides et on montre que la partie non résolue de la traînée joue un rôle majeur dans l'expansion du lit. Une analyse corrélative montre que la traînée filtrée peut s'exprimer ccomme:

$$\overline{\left(\frac{\alpha_p \rho_p}{\tau_p} \, \mathbf{V_r}\right)} = \frac{\overline{\alpha}_p \rho_p}{\widetilde{\tau}_p} \; \left(\widetilde{\mathbf{W}}_\mathbf{r} + \widetilde{\mathbf{V}}_\mathbf{d}\right) \tag{5}$$

où $\widetilde{\mathbf{V}}_\mathbf{d}$ est une vitesse de dérive de sous maille, provenant des homogénéités à l'intérieur du volume de filtrage. Celle-ci est définie par:

$$\widetilde{\mathbf{V}}_\mathbf{d} \; = \; \widetilde{\mathbf{U}}_{\mathbf{g@p}} - \widetilde{\mathbf{U}}_\mathbf{g} \tag{6}$$

avec $\widetilde{\mathbf{U}}_{\mathbf{g@p}}$ qui est la vitesse filtrée du gaz vue par les particules.

Une fermeture dite fonctionnelle de la vitesse de dérive est proposée au chapitre 4. Cette fermeture suppose que la rôle de celle-ci est de réduire la vitesse relative effective. Cela conduit alors à:

$$\overline{\left(\frac{\alpha_p \rho_p}{\tau_p} \, V_{r,\alpha}\right)} = \frac{\overline{\alpha}_p \rho_p}{\widetilde{\tau}_p} \left(1 + f(\overline{\Delta}^*) \; h(\overline{\alpha}_p) \; K_{\alpha\alpha}\right) \widetilde{W}_{r,\alpha} \tag{7}$$

où $f(\overline{\Delta}^*)$ et $h(\overline{\alpha}_p)$ sont fermés en utilisant des mesures obtenues par des simulations pleinement résolues. $K_{\alpha\alpha}$ sont des constantes ajustées par une procédure dynamique. Les

résultats des simulations obtenues sur des maillages grossiers sont en bon accord avec les résultats des simulations pleinement résolues. Grâce au modèle développé, l'expansion du lit simulé est indépendante de la taille du maillage utilisée.

Le chapitre 5 présente l'application des modèles dits structurels, développés pour la viscosité turbulente dans les écoulements turbulents monophasiques, à la modélisation de la vitesse de dérive de sous maille. On applique en particulier le modèle gradient, dont la forme est la suivante:

$$\overline{\alpha}_g \, \overline{\alpha}_p \, \widetilde{V}_{d,i} = \; C \, \overline{\Delta}^2 \; \frac{\partial \overline{\alpha}_p}{\partial x_j} \; \frac{\partial \widetilde{U}_{g,i}}{\partial x_j} \tag{8}$$

La corrélation a-priori est très forte, et les résultats obtenus a-postériori sur des maillages grossiers sont améliorés vis à vis des simulations en l'absence de modèles. Cependant, des maillages suffisamment raffinés sont nécessaires pour obtenir la bonne hauteur de lit avec l'utilisation de ce type de modèles.

Enfin, dans le Chapitre 6, les deux modèles développés sont testés sur une configuration expérimentale de lit fluidisé turbulent de particules FCC. Les mesures de densités et de débits massiques de solides fournies par TOTAL, CReG, sont comparées aux résultats des simulations. Le modèle fonctionnel permet de prédire correctement la hauteur du lit, alors que le modèle structurel prédit le bon débit massique de solide quand un maillage suffisamment raffiné est utilisé. Les résultats sont encourageants mais nécessitent d'être testés pour des maillages plus raffinés.

Chapter 1

Introduction

1.1 Context of the study

This study is concerned with the problem of the prediction of gas-particle flows in the specific domain of fluidized beds. Fluidization is the operation by which solid particles are transformed into a fluid-like state through suspension in a gas or liquid. When a fluid is passed upward through a bed of particles at a sufficient flow rate, particles become agitated and large instabilities with bubbling and channelling of gas are observed. When the flow rate is large enough to transport particles, the fluidized bed is said to be circulating. Bubbling fluidized beds and circulating fluidized beds are widely used in several industrial applications (Kunii and Levenspiel, 1991). The rapid mixing of solids, leading to close to isothermal conditions throughout the reactor, as well as the fluid-like flow of particles allowing continuous operations, make the fluidized bed an advantageous process. Nevertheless, due to large instabilities, flow is difficult to describe and predict. Computational fluid dynamics (CFD) offers a powerful tool to analyze flow inside fluidized beds. We are interested in the development of reliable models enabling the prediction inside the regenerator of a fluid catalytic cracking (FCC) unit.

The catalytic breakdown of hydrocarbons into lower-molecular-weight materials (cracking reactions) is dominated by two features: the reactions are endothermic and they are accompanied by carbon deposition on solid surfaces (Kunii and Levenspiel, 1991). Therefore the process is composed of two fluidized-bed units (*cf.* Figure 1.1). The first one, called the reactor, is the location for the absorption of heat, for reaction, and for carbon decomposition. The second one, called the regenerator, is the location where the deposited carbon is burned off and heat is released. The heat is then returned to the reactor to feed the reaction. Solid transport is the means of heat transport between the the two units.

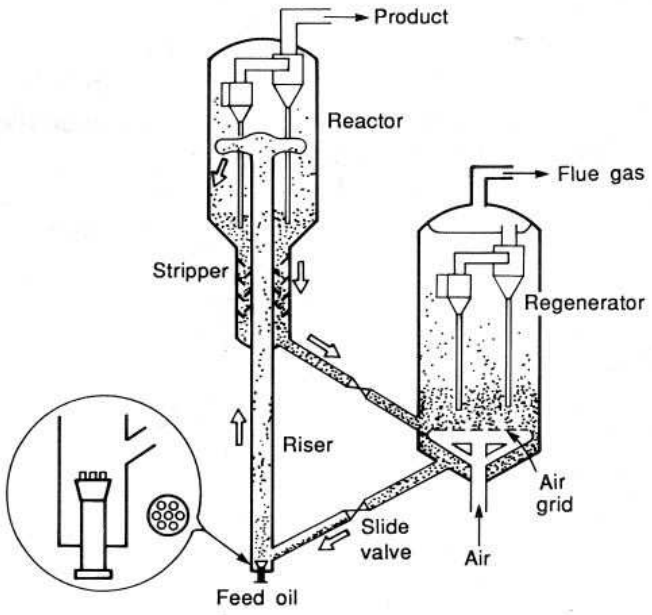

Figure 1.1: A typical riser cracking FCC unit (from Kunii and Levenspiel (1991)).

The generator is typically 8 m ID, 15 m high. Superficial gas velocity is about 1 m/s and particles with a mean diameter around 70 μm and a density of 1 400 kg/m^3 belong to group A, according to the Geldart classification (Geldart, 1973). The correct prediction of the bed expansion and the transport disengaging height is crucial for the design and scale-up of the generator.

Various CFD methods are used to simulate gas-particle flows. Traditionally, three different levels of approximation are made (Van der Hoef et al., 2006). The most detailed level is usually called the direct numerical simulation, or the Lattice Boltzmann model. Few particles move in a surrounding fluid where all spatial and temporal scales are fully resolved. No-slip boundary conditions are set at the fluid-particle interface. Due to expensive computational cost, the number of particles in such simulations is typically around 500. Simulation data are used to construct closure laws needed at larger scale, such as the drag law (Beetstra et al., 2007; Hill et al., 2001; Van der Hoef et al., 2005).

At a higher level, the fluid is still a continuous media but the particles are discrete spheres that move following Newton's law of motion and interact with each other by collisions. This is call the discrete particle model, or Lagrangian simulations. The scale at which the fluid is solved is an order of magnitude larger than the particles (a fluid cell typically contains 10^2 or 10^3 particles). A drag closure law is needed to model the interaction

between gas and particles as well as a collisional model between particles. Two collisional models, respectively called the hard- and soft-sphere approaches, are used (see for instance Deen et al. (2007) for a review). Numbers of particles is about 10^6, which corresponds to a system of which the width is of the order of 0.1 m. Such simulations can be used to study the effect of particle and gas properties on the collective behaviour of particles (Hoomans et al., 1996; Li and Kuipers, 2003; Tsuji et al., 1993) as well as the effect of inter-particle forces (Ye et al., 2004, 2005b). Discrete particle simulations in simple configurations are also used to validate closures issued from kinetic theory, such as particle pressure, particle viscosity or radial distribution function (Sangani et al., 1996; Tsao and Koch, 1995; Ye et al., 2005a).

Finally, among the various CFD methods available, the two-fluid method, also called the Eulerian approach, is the most suitable for engineering applications. A continuum description is employed for both the gas phase and the solid phase. Closures are needed for both the drag force and the stress tensor of the particle phase (particle pressure and viscosity). An adapted kinetic theory of granular flows is employed to provide closures for the particle stress tensor. This approach has been applied with success to group B particles (Balzer et al., 1995; Ding and Gidaspow, 1990; Peirano et al., 2001; Van Wachem et al., 2001) - which have a greater diameter and density than group A particles, as seen in Figure 1.2. However, the application of this method to bubbling and turbulent fluidized beds of fine Geldart A particles leads to severe overestimation of the bed expansion (Ferschneider and Mege, 1996; Gao et al., 2009; Hosseini et al., 2009; Makkawi et al., 2006; McKeen and Pugsley, 2003; Wang, 2009; Zimmermann and Taghipour, 2005). The drag law is a key parameter in the prediction of the bed expansion and several closures can be found in the litterature (Ergun, 1952; Gibilaro et al., 1985; Gidaspow, 1994; Van der Hoef et al., 2005; Syamlal and O'Brien, 1989; Wen and Yu, 1966). Nevertheless all the closures lead to the same order of overestimation.

The origin of the problem is still under discussion. McKeen and Pugsley (2003) argued that this difference could be related to the presence of inter-particle forces (IPF) such as Van deer Waals forces. IPF lead to the formation of clusters and consequently to a modification of the effective particle size in the drag law. By fitting their numerical results to their experimental data, McKeen and Pugsley (2003) found an effective particle agglomerate diameter of around 150 μm. However, the bed expansion predicted by their numerical simulation decreases as the mesh size decreases. As they do not achieve mesh convergence, their results are questionable. Moreover, Wang et al. (2009) performed highly resolved three-dimensional simulations of a bubbling fluidized bed at moderate superficial gas velocity. By comparing their results to those obtained using Lagrangian simulations, they

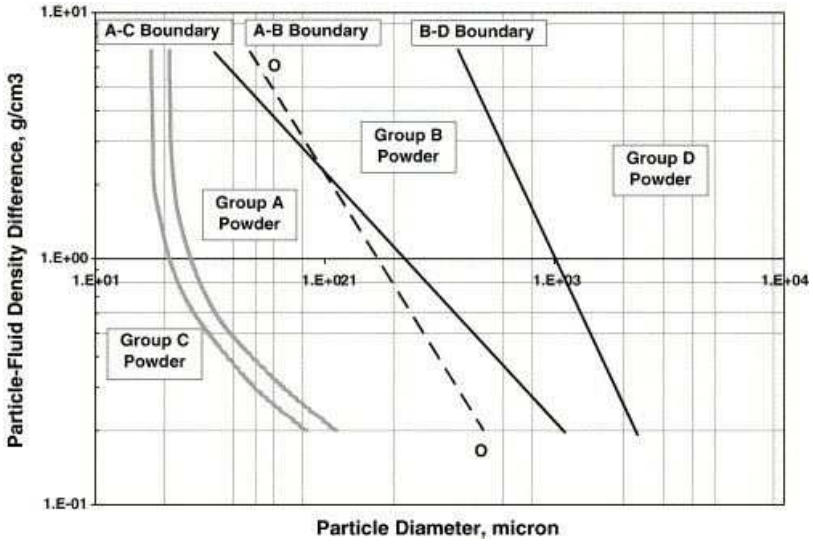

Figure 1.2: Original Geldart's classification of particles. 0-0 line is the Oltrogge (1972) limit. From Yang (2007).

concluded that the standard two-fluid model with the standard Gidaspow et al. (1992) drag law does not lead to an overestimation of the bed expansion when sufficiently fine meshes are used. Moreover, the influence of the mesh size on the macroscopic behaviour is also found in circulating fluidized bed (Agrawal et al., 2001; Andrews IV et al., 2005; Heynderickx et al., 2004; Igci et al., 2008; Zhang and VanderHeyden, 2002). Agrawal et al. (2001) show that if small structures present in the bed are not completely solved, the drag force is overestimated. This fact support the idea that the mesh size is a key parameter in the numerical simulation fluidized bed using the two-fluid model.

1.2 Plan

The present study is composed as follows. In Chapter 2, we focus on the modelling of physical phenomena that are not yet taken into account in the standard two-fluid model. After a description of the closures used to describe the particle phase when the presence of the interstitial fluid is taken into account, a comparison with discrete particle simulations in a simple shear flow is made. An upgrade of the collisional terms is suggested, leading to a good prediction for low Stokes number flows which are poorly described when using the standard models. Then, we look at the hydrodynamic effects that occur during particles collisions. An apparent restitution coefficient is suggested to describe this effect at the macroscopic level, depending on both the particle-fluid properties and the particle agitation.

Finally a methodology to implement the van der Waals forces in the two-fluid model is presented. This leads to a cohesive pressure term in the momentum equation of the particle phase.

Chapter 3 is devoted to the study of the influence of the mesh size on the numerical resolution of the two-fluid model. In particular, we are interested in the prediction of bed expansion. A preliminary study shows that the bed height depends very strongly on the mesh resolution. Consequently, the filtered formalism is applied to the two-fluid model equations and the unresolved part of the drag is shown to play a major role in the bed expansion. Then the unresolved part of the drag is expressed in the form of a subgrid drift velocity coming from subgrid inhomogeneities as well as the correlation between gas velocity and particle concentration.

In Chapters 4 and 5 two distinct ways to model the subgrid drift velocity are suggested. A functional model that assumes that the function of the subgrid drift velocity is to reduce the effective relative velocity is described in Chapter 4. A structural model that relies on mathematical properties of the filtering operation is proposed in Chapter 5. These two models are compared to highly resolved simulations and promising results are found.

Finally, in Chapter 6, the two models developed are tested on an experimental pilot-scale turbulent fluidized bed of FCC particles. Measurements of the density within the bed and solid mass flux were provided by TOTAL, CReG, and are compared to results obtained with the models developed.

Chapter 2

Statistical modelling of dense fluidized beds

2.1 Introduction

In this Chapter we focus on the statistical modelling of dense fluidized beds. We particularly look at physical phenomena that may contribute to Geldart A fluidization and that are not yet taken into account in the standard two-fluid models. Geldart A particles differ from Geldart B particles by their smaller diameter and density. In consequence, their relaxation time is an order of magnitude lower. Hence, phenomena that are negligible for group B particles, and therefore not taken into account in the standard two-fluid model, can have an influence for Geldart A particles.

Firstly, as the particles have a smaller relaxation time, they experience flow at a smaller Stokes number. It is known that kinetic theory failed to predict flow at law Stokes numbers. After a description of the standard kinetic theory used in Section 2.2, Section 2.3 describe an extension of the kinetic theory for such flows, in the particular case of the simple shear flow. Secondly, as particles have less inertia, the interstitial fluid can play a role during particle collisions. Before colliding, their relative velocity decreases, leading to an apparent restitution coefficient. Section 2.4 describes the implementation of this effect in the two-fluid model. Finally the presence of inter-particle forces is investigated. Their effect is clearly observed for Geldart C particles which are smaller than A particles and Section 2.5 describe the implementation of Van der Waals forces in the two-fluid model.

2.2 Two-fluid modelling

2.2.1 Introduction

In the two-fluid model, both phases are considered to be continuous and interpenetrating. Gas and particle phases are described, at minima, by the corresponding phase volume fractions and velocities and a kinetic agitation for the particle phase. Constitutive equations are needed to calculate the spatial and temporal variations of quantities. The Navier-Stokes equations are used for the gas phase, while several closures exist for the particle-phase equations, specifically for the particle-stress tensor and particle agitation transport equation. In the early hydrodynamic models, the viscosity and the pressure of the particle phase were determined from experiments (Kuipers et al., 1992). Ding and Gidaspow (1990) used the closures developed by Lun et al. (1984) in the kinetic theory of dry granular flow. Momentum equation of particle phase was completed by the interfacial momentum transfer between the gas and particles. Adapting the work of Jenkins and Richman (1985) developed for dry granular flow, Balzer et al. (1995) took the gas influence into account during the development of closures for the particle-stress tensor and the transport equation of the kinetic particle agitation. These closures will be used as a starting point to incorporate new physical phenomena.

We briefly summarize the way closures of Balzer et al. (1995) were derived. Particular attention will be paid to collisional terms because they will be modified in the following sections in order to take shear-induced collisions or hydrodynamic effects into account. The methodology was originally developed by Jenkins and Richman (1985) for rapid granular flow and was adapted for gas-particle flow simultaneously by Balzer et al. (1995) and Koch and co-workers (Tsao and Koch, 1995; Sangani et al., 1996), while the later focus on simple shear flow.

2.2.2 Statistical description

We consider spherical particles, of diameter d_p and radius $a = d_p/2$, moving in a surrounding fluid. Only binary collisions are considered and no friction or rotation is taken into account. The post-collision velocities $\mathbf{c_a}^*$ and $\mathbf{c_b}^*$ of two colliding particles a and b are determined in function of $\mathbf{c_a}$ and $\mathbf{c_b}$, the particle velocities at impact:

$$\mathbf{c_a}^* = \mathbf{c_a} - \frac{1}{2}(1+e_c)\ (\mathbf{g}\cdot\mathbf{k})\ \mathbf{k} \tag{2.1}$$

$$\mathbf{c_b}^* = \mathbf{c_b} + \frac{1}{2}(1+e_c)\ (\mathbf{g}\cdot\mathbf{k})\ \mathbf{k} \tag{2.2}$$

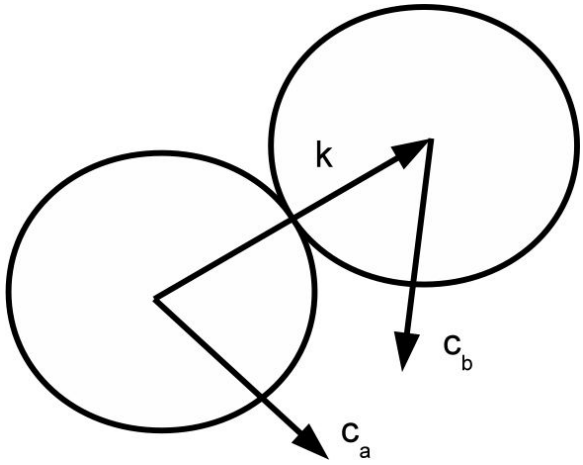

Figure 2.1: Collision between particle a, at the left, and particle b, at the right.

with $\mathbf{g} = \mathbf{c_a} - \mathbf{c_b}$, the particle relative velocity at the impact, and $\mathbf{k} = (\mathbf{x}_b - \mathbf{x}_a)/d_p$, the unit vector pointing from the center of particle a to the center of particle b (cf. Figure 2.1). The elasticity coefficient e_c is the only collision parameter and will be considered constant in this section. The kinetic energy loss of the pair of particles is given by $\Delta E_c = -(1-e_c^2)\ (\mathbf{g}\cdot\mathbf{k})^2/\ 2$.

Between two collisions, the velocity $\mathbf{V_p}$ and the position $\mathbf{X_p}$ of the particle are given by Newton's laws of motion:

$$\frac{d\mathbf{X_p}}{dt} = \mathbf{V_p} \tag{2.3}$$

$$\frac{d\mathbf{V_p}}{dt} = -\frac{1}{\tau_p}(\mathbf{V_p} - \mathbf{U_g}(\mathbf{X_p})) + \mathbf{a} - \frac{1}{\rho_p}\,\mathbf{grad}P_g \tag{2.4}$$

where τ_p is the particle relaxation time given by the drag law and $\mathbf{a}$ the gravity contribution.

The kinetic theory start by a statistical description of the flow using a Boltzmann-Liouville equation, following Chapman and Cowling (1970):

$$\frac{\partial f_p}{\partial t} + \frac{\partial}{\partial x_i}(c_{p,i} f_p) + \frac{\partial}{\partial c_{p,i}}\left(< \frac{F_i}{m_p} \mid \mathbf{V_p} = \mathbf{c_p}, \mathbf{X_p} = \mathbf{x} > f_p \right) = \left(\frac{\partial f_p}{\partial t}\right)_{coll} \tag{2.5}$$

where $f_p(\mathbf{c_p}, \mathbf{x}, t)$ is the one-particle distribution function and $F_i/m_p = d\mathbf{V_p}/dt$ is the acceleration of a particle given by Eq. 2.4. $< A \mid B >$ is the conditioned average of A by B. The right hand side of Eq. 2.5 is the collisional rate of change of the distribution function. Eq. 2.5 is not directly solved, and only balance laws of moments of f_p are looked for. The

average $< \Psi >_p$ of a function $\Psi = \Psi(\mathbf{c_p}, \mathbf{x})$ is given by:

$$n_p < \Psi >_p = \iiint \Psi \; f_p \; \mathbf{dc_p} \tag{2.6}$$

where $n_p = \iiint f_p \; \mathbf{dc_p}$ is the number of particles per unit of volume. The balance law for $< \Psi >_p$ may be obtained by multiplying Eq. 2.5 by $\mathbf{dc_p}$ and then integrating over $\mathbf{dc_p}$. The mean particle velocity is defined by $\mathbf{U_p} = < \mathbf{c_p} >_p$ and the kinetic stress tensor is $R_{p,ij} = < C_{p,i} C_{p,j} >_p$, where $\mathbf{C_p} = \mathbf{c_p} - \mathbf{U_p}$ is the fluctuating velocity relative to the mean. Kinetic particle agitation is given by $q_p^2 = < C_{p,i} C_{p,i} >_p /2$. The balance laws for the component of the particle velocity are given by:

$$\begin{aligned} \alpha_p \, \rho_p \, \frac{DU_{p,i}}{Dt} &= \alpha_p \, \rho_p \, g_i - \alpha_p \, \frac{\partial P_g}{\partial x_i} + \frac{\alpha_p \, \rho_p}{\tau_p} \, (U_{g,i} - U_{p,i}) \\ &- \frac{\partial}{\partial x_j} (\alpha_p \, \rho_p \, R_{p,ij}) + C_i \end{aligned} \tag{2.7}$$

where $\alpha_p = n_p m_p / \rho_p$ is the particle volume fraction and C_i the collisional rate of change of $\alpha_p \, \rho_p \, U_{p,i}$. The balance laws for the components of the kinetic stress tensor are given by:

$$\begin{aligned} \alpha_p \, \rho_p \, \frac{DR_{p,ij}}{Dt} &= -2 \, \frac{\alpha_p \, \rho_p}{\tau_p} \, R_{p,ij} - \frac{\partial}{\partial x_k} (\alpha_p \, \rho_p \, S_{p,ijk}) \\ &- \alpha_p \rho_p \, R_{p,ik} \, \frac{\partial U_{p,j}}{\partial x_k} - \alpha_p \rho_p \, R_{p,jk} \, \frac{\partial U_{p,i}}{\partial x_k} \\ &+ C_{ij} \end{aligned} \tag{2.8}$$

where $S_{p,ijk} = < C_{p,i} C_{p,j} C_{p,k} >_p$ and C_{ij} is the collisional rate of change of $\alpha_p \rho_p R_{p,ij}$.

The collisional rate of change of C_i and C_{ij} are defined by $C_i = \mathbb{C}(m_p C_{p,i})$ and $C_{ij} = \mathbb{C}(m_p C_{p,i} C_{p,j})$ where $\mathbb{C}(\Psi) = \iiint \Psi \left(\frac{\partial f_p}{\partial t} \right)_{coll} \mathbf{dc_p}$. This one could also be written as:

$$\mathbb{C}(\Psi) = d_p^2 \iiint_{\mathbf{g} \cdot \mathbf{k} > 0} \delta \Psi_a \; f_p^{(2)}(\mathbf{c_a}, \mathbf{x}, \mathbf{c_b}, \mathbf{x} + d_p \mathbf{k}, t) \; (\mathbf{g} \cdot \mathbf{k}) \, \mathbf{dk} \; \mathbf{dc_a dc_b} \tag{2.9}$$

where $\delta \Psi$ is the variation of Ψ during a collision, given by Eqs. 2.1 and 2.2 and $f_p^{(2)}$ is the complete pair distribution function. In dilute flows, the assumption of molecular chaos is generally used to relate the complete pair distribution function to the one-particle velocity distribution function. In the case of high volume fraction, the radial distribution function at contact, g_0, is introduced. Hence in a homogenous flow, the complete pair distribution

function is given by:

$$f_p^{(2)}(\mathbf{c_a}, \mathbf{x_a}, \mathbf{c_b}, \mathbf{x_b}, t) = g_0(\alpha_p)\ f_p(\mathbf{c_a}, \mathbf{x_a}, t)\ f_p(\mathbf{c_b}, \mathbf{x_b}, t) \tag{2.10}$$

For a hard-sphere distribution, a good approximation of g_0 for $\alpha_p < 0.5$ is obtained from Carnahan and Starling (1969):

$$g_0 = \frac{1 - \alpha_p/2}{(1-\alpha_p)^3} \tag{2.11}$$

The expression of the one-particle velocity distribution function is needed to enable calculation of C_{ij}. Different closures of f_p and different ways of calculating Eq. 2.9 will lead to different theories.

2.2.3 Rapid granular flows

In a highly agitated regime resulting from a homogeneous shear of a granular flow, Grad (1949) describe the velocity distribution function as a deviated Maxwellian:

$$f_p(\mathbf{c_p}, \mathbf{x}, t) = \left(1 + \frac{\widehat{R}_{p,ij}}{2T^2}\ C_{p,i}C_{p,j}\right) f_0(\mathbf{c_p}, \mathbf{x}, t) \tag{2.12}$$

where $\widehat{R}_{p,ij} = R_{p,ij} - T\delta_{ij}$ is the anisotropic part of the kinetic stress tensor and f_0 the Maxwellian given by:

$$f_0 = \frac{n_p}{(2\pi T)^{3/2}}\ exp(-\frac{\mathbf{C_p}^2}{2T}) \tag{2.13}$$

$\mathbf{C_p} = \mathbf{c_p} - \mathbf{U_p}(\mathbf{x})$ is the fluctuating velocity relative to the mean velocity at the $\mathbf{x}$ position and $T = 2/3\ q_p^2$ is the granular temperature. .

Jenkins and Richman (1985) proposed to express $\mathbb{C}(\Psi)$ as a function of a source term and a flux term, by noting that an equivalent expression for $\mathbb{C}(\Psi)$ is:

$$C(\Psi) = d_p^2 \iiint_{\mathbf{g}\cdot\mathbf{k}>0} \delta\Psi_b\ f_p^{(2)}(\mathbf{c_a}, \mathbf{x} - d_p\mathbf{k}, \mathbf{c_b}, \mathbf{x}, t)\ (\mathbf{g}\cdot\mathbf{k})\ \mathbf{dk}\ \mathbf{dc_a dc_b} \tag{2.14}$$

The reader should note that $\delta\Psi_b$ in Eq. 2.14 is defined with reference to the x position. For example, if $\Psi = \mathbf{C_p}$, $\delta\Psi_b = \delta(\mathbf{c_p} - \mathbf{U_p}(\mathbf{x}))$. Then $f_p^{(2)}$ is expanded in a Taylor series:

$$f_p^{(2)}(\mathbf{c_a}, \mathbf{x} - d_p\mathbf{k}, \mathbf{c_b}, \mathbf{x}, t) \simeq \left\{1 - d_p k_i\ \frac{\partial}{\partial x_i}\right\} f_p^{(2)}(\mathbf{c_a}, \mathbf{x}, \mathbf{c_b}, \mathbf{x} + d_p\mathbf{k}, t) \tag{2.15}$$

By putting Eq. 2.15 in Eq. 2.14 and taking one half of the sum of Eq. 2.9 and Eq. 2.14, $\mathbb{C}(\Psi)$ can be written:

$$\mathbb{C}(\Psi) = \chi(\Psi) - \frac{\partial}{\partial x_i}\ \theta_i(\Psi) - \zeta(\Psi) \tag{2.16}$$

where

$$\chi(\Psi) = \frac{1}{2} d_p^2 \iiint_{\mathbf{g}\cdot\mathbf{k}>0} \Delta\Psi\ f_p^{(2)}(\mathbf{c_a}, \mathbf{x}, \mathbf{c_b}, \mathbf{x} + d_p\mathbf{k}, t)\ (\mathbf{g}\cdot\mathbf{k})\ \mathbf{dk}\ \mathbf{dc_a dc_b} \tag{2.17}$$

$$\theta_i(\Psi) = \frac{1}{2} d_p^3 \iiint_{\mathbf{g}\cdot\mathbf{k}>0} \delta\Psi_b\ k_i\ f_p^{(2)}(\mathbf{c_a}, \mathbf{x}, \mathbf{c_b}, \mathbf{x} + d_p\mathbf{k}, t)\ (\mathbf{g}\cdot\mathbf{k})\ \mathbf{dk}\ \mathbf{dc_a dc_b} \tag{2.18}$$

$$\zeta(\Psi) = \frac{1}{2} d_p^3 \iiint_{\mathbf{g}\cdot\mathbf{k}>0} \frac{\partial \delta\Psi_b}{\partial C_{b,k}} \frac{\partial U_{p,k}}{\partial x_i}(\mathbf{x} + d_p\mathbf{k})\ k_i\ f_p^{(2)}(\mathbf{c_a}, \mathbf{x}, \mathbf{c_b}, \mathbf{x} + d_p\mathbf{k}, t)\ (\mathbf{g}\cdot\mathbf{k})\ \mathbf{dk}\ \mathbf{dc_a dc_b} \tag{2.19}$$

where $\Delta\Psi = \delta\Psi_a + \delta\Psi_b$ is defined with respect to the x position. For a homogeneous simple shear flow and $\Psi = m_p C_{p,i} C_{p,j}$, Eq. 2.16 yields:

$$C_{ij} = \chi_{ij} - \theta_{ik}\frac{\partial U_{p,j}}{\partial x_k} - \theta_{jk}\frac{\partial U_{p,i}}{\partial x_k} \tag{2.20}$$

where $\chi_{ij} = \chi(m_p C_{p,i} C_{p,j})$ and $\theta_{ij} = \theta_i(m_p C_{p,j})$. In this case, the balance laws for the components of the kinetic stress tensor becomes in steady state:

$$(\alpha_p \rho_p R_{p,ik} + \theta_{ik})\frac{\partial U_{p,j}}{\partial x_k} + (\alpha_p \rho_p R_{p,jk} + \theta_{jk})\frac{\partial U_{p,i}}{\partial x_k} = -\frac{2\,\alpha_p\,\rho_p}{\tau_p} R_{p,ij} + \chi_{ij} \tag{2.21}$$

As the total momentum of the pair of particles is conserved during a collision, we have $\chi_i = 0$. The modified molecular chaos assumption, Eq. 2.10, and the Grad development, Eq. 2.12, are used to calculate χ_{ij}, θ_{ij} and θ_{ijk} . Moreover, $f_p(\mathbf{c_b}, \mathbf{x} + d_p\mathbf{k}, t)$ is expanded in a Taylor series around x:

$$f_p(\mathbf{c_b}, \mathbf{x} + d_p\mathbf{k}, t) \simeq f_p(\mathbf{c_b}, \mathbf{x}, t) + d_p k_i\ \frac{\partial}{\partial x_i}\ f_p(\mathbf{c_b}, \mathbf{x}, t) \tag{2.22}$$

Consequently, all fluctuating velocities in the expression of χ_{ij}, θ_{ij} are expressed with reference to the x position. When defining $\mathbf{C_a} = \mathbf{c_a} - \mathbf{U_p}(\mathbf{x})$ and $\mathbf{C_b} = \mathbf{c_b} - \mathbf{U_p}(\mathbf{x})$, χ_{ii} is written:

$$\chi_{ii} = \frac{m_p\, g_0\, d_p^2\, n_p^2}{16\,(\pi T)^3} \iiint_{\mathbf{G}\cdot\mathbf{k}>0} \Delta(C_{a,i} C_{a,i})\ exp(-\frac{\mathbf{C_a}^2}{2T})\ exp(-\frac{\mathbf{C_b}^2}{2T})\ (\mathbf{g}\cdot\mathbf{k})\ \mathbf{dk}\ \mathbf{dC_a dC_b} \tag{2.23}$$

where the relative velocity $\mathbf{g} = \mathbf{c_a} - \mathbf{c_b}$ can be expressed according to the fluctuating relative velocity $\mathbf{G} = \mathbf{C_a} - \mathbf{C_b}$ by:

$$\mathbf{g} = \mathbf{G} \tag{2.24}$$

The following expressions for collisional terms C_{ii} are obtained for a simple shear flow where $\partial U_{p,i}/\partial x_j = \gamma\ \delta_{i,1}\ \delta_{j,3}$, with γ the shear rate:

$$C_{ii} = \chi_{ii} - 2\ \theta_{13}\ \gamma \tag{2.25}$$
$$C_{33} = \chi_{33} \tag{2.26}$$
$$C_{13} = \chi_{13} - \theta_{33}\ \gamma \tag{2.27}$$
$$\tag{2.28}$$

with:

$$\chi_{ii} = -(1-e_c^2)\ \frac{\alpha_p\rho_p}{\tau_c}\ T \tag{2.29}$$
$$\chi_{33} = -\frac{1}{3}\ (1-e_c^2)\ \frac{\alpha_p\rho_p}{\tau_c}\ T - \frac{1}{5}\ (1+e_c)(3-e_c)\ \frac{\alpha_p\rho_p}{\tau_c}\ \widehat{R}_{p,33} \tag{2.30}$$
$$\chi_{13} = -\frac{6}{5}\ \alpha_p\rho_p\ \alpha_p g_0\ (1+e_c)(e_c-2)\ T\ \gamma - \frac{1}{5}\ (1+e_c)(3-e_c)\ \frac{\alpha_p\rho_p}{\tau_c}\ \widehat{R}_{p,13} \tag{2.31}$$
$$\theta_{33} = 2\ \alpha_p\rho_p\ \alpha_p g_0\ (1+e_c)\ (T + \frac{2}{5}\ \widehat{R}_{p,33}) \tag{2.32}$$
$$\theta_{13} = -\frac{4}{5}\ \alpha_p\rho_p\ \alpha_p g_0\ (1+e_c)\ (d_p\sqrt{\frac{T}{\pi}}\ \gamma - \widehat{R}_{p,13}) \tag{2.33}$$

τ_c is the collisional time given by:

$$\frac{1}{\tau_c} = 24\ \frac{\alpha_p g_0}{d_p}\ \sqrt{\frac{2}{3}\frac{q_p^2}{\pi}} \tag{2.34}$$

Using these closures for the collisional terms, Sangani et al. (1996) solved Eqs. 2.21 analytically in the case of the simple shear flow. The corresponding solution is called the ignited state theory.

Balzer et al. (1995) use the same expression for the collisional terms C_{ij}, but use a Boussinesq assumption to solve Eqs. 2.21. The total stress tensor $\Sigma_{p,ij} = R_{p,ij} + \alpha_p\rho_p\theta_{ij}$ is given by:

$$\Sigma_{p,ij} = \left(P_p - \lambda_p\frac{\partial U_{p,m}}{\partial x_m}\right)\delta_{ij} - \mu_p\left(\frac{\partial U_{p,i}}{\partial x_j} + \frac{\partial U_{p,j}}{\partial x_i} - \frac{2}{3}\frac{\partial U_{p,m}}{\partial x_m}\ \delta_{ij}\right) \tag{2.35}$$

where the expressions of P_p is the particle pressure, $\mu_p = \alpha_p \rho_p \ (\nu_p^{kin} + \nu_p^{coll})$ the shear viscosity and λ_p the volume viscosity, are given in Appendix A. This solution leads to the same results as those obtained by Sangani et al. (1996) in simple shear flow when $St \geq 10$, where $St = \gamma \, \tau_p$ is the Stokes number (Boelle et al., 1995). The closure provided by Balzer et al. (1995) and summarized in Appendix A takes the effect of the interstitial fluid into account. For instance, the kinetic viscosity is written as:

$$\nu_p^{kin} = \frac{2}{3} \, q_p^2 \, \frac{\tau_c}{\sigma_c} \, (1 + \alpha_p g_0 \phi_c) \, (1 + \frac{2}{\sigma_c} \, \frac{\tau_c}{\tau_p})^{-1} \tag{2.36}$$

where $\sigma_c = (1 + e_c)(3 - e_c)/5$ and $\phi_c = 2/5 \ (1 + e_c)(3e_c - 1)$. For a dry granular flow, $\tau_p \to \infty$. In consequence, ν_p^{kin} tends to the value given by the dry granular flow theory of Jenkins and Richman (1985).

2.2.4 The quenched state theory

The quenched state theory was developed by Tsao and Koch (1995) in the particular case of simple shear flows when both the particle volume fraction and the particle inertia are low. In this case, the relaxation time of the particle τ_p is of the same order or lower than the average time between successive collisions τ_c. Particles have very weak velocity fluctuations as they are more likely to recover the fluid streamlines after a collision. This specific regime was called the quenched state (Tsao and Koch, 1995) as opposed to the ignited theory for agitated systems. Tsao and Koch (1995) proposed to close the collisional term Eq. 2.9 assuming a Dirac function for the velocity distribution function:

$$f_p(\mathbf{c_p}, \mathbf{x}) = n_p \ \delta(\mathbf{c_p} - \mathbf{U_p}(\mathbf{x})) \tag{2.37}$$

This assumes that shear-induced collisions are dominant compared to agitation-induced collisions. Collisional term C_{ij}, Eq. 2.9, becomes:

$$\mathbb{C}(\Psi) = g_0 \, n_p^2 \, d_p^2 \int_{\mathbf{g}\cdot\mathbf{k}<0} (\delta\Psi_a \ (\mathbf{g} \cdot \mathbf{k}) | \mathbf{c_a} = \mathbf{U_p}(\mathbf{x}), \mathbf{c_b} = \mathbf{U_p}(\mathbf{x} + d_p \mathbf{k})) \ \mathbf{dk} \tag{2.38}$$

The relative velocity $\mathbf{g} = \mathbf{c_a} - \mathbf{c_b}$ in Eq. 2.38 is reduced to:

$$\mathbf{g} = -\delta \mathbf{U_p} \tag{2.39}$$

where $\delta \mathbf{U_p}$ is the increment of mean velocity given by:

$$\delta \mathbf{U_p} = \mathbf{U_p}(\mathbf{x} + d_p \mathbf{k}) - \mathbf{U_p}(\mathbf{x}) \tag{2.40}$$

Here we find $\delta\mathbf{U_p} = \gamma\ d_p\ k_z\ \mathbf{e_x}$. Hence the relative velocity induced by the shear is taken into account and the relative velocity induced by the particle agitation is neglected. The characteristic relative velocity of two colliding particles induced by the agitation can be estimated by $\sqrt{q_p^2}$. The characteristic relative velocity of two colliding particles induced by the shear can be estimated by $\gamma\, a$, where a is the particle radius. The first mechanism is dominant when the relative velocity between two colliding particles is mainly due to their agitation corresponding to $T^* \gg 1$, with:

$$T^* = T/(\gamma a)^2 \tag{2.41}$$

At opposite, shear-induced collisions will be dominant behind agitation-induced collisions when $T^* \ll 1$. Consequently the quenched state theory will hold when $T^* \ll 1$. The resulting expression for collisional terms is:

$$C_{ij}^* = \left(\frac{1+e_c}{2}\right)^2 \alpha_p g_0\ \frac{24}{\pi}\ I_{ij} \tag{2.42}$$

with $C_{ij}^* = C_{ij}/(\gamma^3 a^2 \alpha_p \rho_p)$ and I_{ij} are defined by $I_{ij} = -\iint_{k_x k_z<0} (k_x k_z)^3 k_i k_j\, \mathbf{dk}$. Useful values of I_{ij} are: $I_{ii} = 16/105$, $I_{33} = 64/945$ and $I_{13} = -2\pi/105$. The resulting collisional terms are independent of the granular temperature. In particular, they are non-null when T is null. Moreover, as we have:

$$\frac{T}{(\gamma a)^2} = \frac{1}{6}\ St\ C_{ii}^* - \frac{1}{6}\ St^2\ C_{13}^* + \frac{1}{12}\ St^3\ C_{33}^* \tag{2.43}$$

all collisional terms contribute to the production of particle agitation. Finally, the granular temperature is given by:

$$T = \frac{128}{945\pi}\ \left(\frac{1+e_c}{2}\right)^2 \alpha_p g_0\ (\gamma a)^2\ St^3 \left(1 + \frac{9\pi}{16} St^{-1} + \frac{9}{2} St^{-2}\right) \tag{2.44}$$

Eqs. 2.42, 2.43 and 2.44 correspond to the quenched state theory corrected by a factor $2\, g_0$ (Abbas et al., 2009).

2.2.5 Comparison to Lagrangian simulations in shear flows

The simple shear flow is used to investigate the effect of the Stokes number and the particle volume fraction. Particles are put in an infinite sheared gas flow. Fluid velocity $\mathbf{U_g}(\mathbf{x})$ is

taken to be unperturbed by the presence of particles, and is given by:

$$\frac{\partial U_{g,i}}{\partial x_j} = \gamma \ \delta_{i,1} \ \delta_{j,3} \tag{2.45}$$

with γ the shear rate and $\delta_{i,j}$ the Kronecker delta. γ^{-1} is the characteristic time scale of the shear. Flow is assumed to be homogeneous. External forces on particles are reduced to the Stokes drag. Hence the particle relaxation time is given by the Stokes time $\tau_p = \rho_p d_p^2/(18\mu_g)$. In the steady state, the particle velocity field is equal to the gas velocity field: $\mathbf{U_p}(\mathbf{x}) = \mathbf{U_g}(\mathbf{x})$. Steady states are determined by the value of three dimensionless parameters: α_p, the particle volume fraction, $St = \gamma\tau_p$ the Stokes number and e_c the elasticity coefficient.

Sangani et al. (1996), Tsao and Koch (1995), Boelle et al. (1995), Abbas et al. (2009) and Abbas et al. (2010) compared theoretical expressions with results obtained by periodic Lagrangian simulations of hard spheres in a homogeneous shear. Various regimes were found depending on St and α_p.

When $St > 5$, Tsao and Koch (1995) found that particles were highly agitated and ignited state theory gave satisfactory results. When $St \ll 1$, hydrodynamic interactions between particles have a major effect. Such an effect is not taken into account in the theories of quenched or ignited state.

Abbas et al. (2009) performed numerical simulations for $1 \leq St \leq 10$ and a volume fraction between 5 % and 30 %. Particles were perfectly elastic ($e_c = 1$). Their results are shown in Figure 2.2. For $St \geq 5$, two distinct trends are observed at low and high particle volume fraction. In dilute suspensions, the particle agitation decreases with the concentration. In dense suspensions, the particle agitation increases with the concentration. For $St \leq 3.5$, the particle agitation always increases with the concentration. When increasing St from 1 to 10 for a given α_p, the agitation level is enhanced by three orders of magnitude. For moderate to high St numbers ($St = 5$ and 10), the level of particle agitation obtained by the simulations or predicted by the kinetic theory for the ignited state match very well. In contrast, for lower Stokes numbers the theoretical predictions underestimate the particle agitation at low concentrations (by two orders of magnitude when $\alpha_p = 5\%$ and $St = 3.5$). Similar results were obtained by Boelle et al. (1995). The particle agitation given by quenched state theory is in agreement with numerical results for $St = 1$ and $\alpha_p < 30\%$. Nevertheless, when the Stokes number or the particle volume fraction increases, quenched state theory underestimates the particle agitation. The next section will show that the underestimation of the particle agitation predicted by the ignited state theory for low Stokes number is a direct consequence of shear-induced collisions being

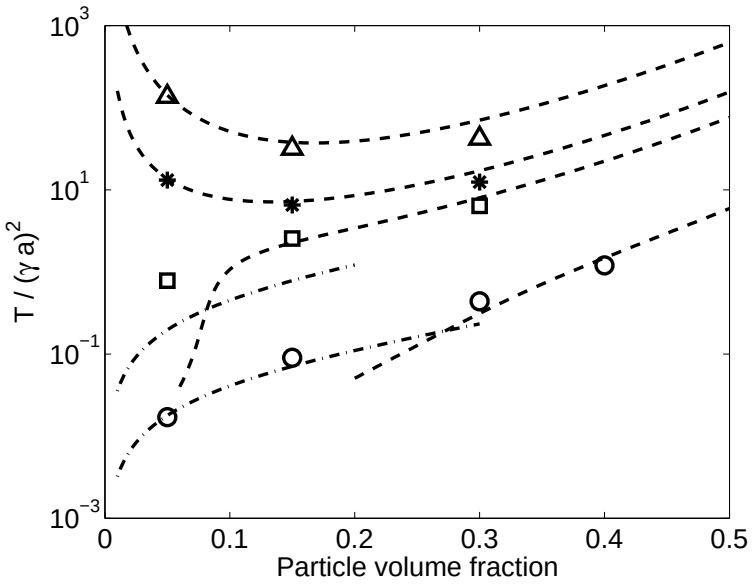

Figure 2.2: Particle agitation as a function of the particle volume fraction for different Stokes numbers (from Abbas et al. (2009)). △, ∗, □ and O: numerical simulations for $St = 10$, 5, 3.5 and 1 respectively. ---- : ignited state theory (from top to bottom, $St = 10$, 5, 3.5 and 1). -·-·- : quenched state theory (from top to bottom, $St = 3.5$ and 1).

only slightly taken into account. Hence, collisional terms tend to zero when the particle agitation decreases, whereas the quenched state theory predicts that collisions are a source of particle agitation. A major input in the closure of collisional terms is the velocity distribution function. It was assumed to be a deviated Maxwellian in the ignited state theory and a Dirac function in the quenched state theory. The velocity distribution function is shown in Figure 2.3 for $\alpha_p = 5$ %. It is close to the Maxwellian when $St = 5$ whereas it is highly peaked around the zero fluctuation when $St = 1$, indicating that most of the particles follow the fluid streamlines.

2.3 Unified theory

2.3.1 Basic idea

In the ignited state theory, the velocity distribution function is closed by a deviated Maxwellian, while it is closed by a Dirac distribution in the quenched state theory. Nevertheless, a Maxwellian converges pointwise to a Dirac distribution when the granular temperature tends to zero. Hence, a Dirac distribution can be said, from this point of view,

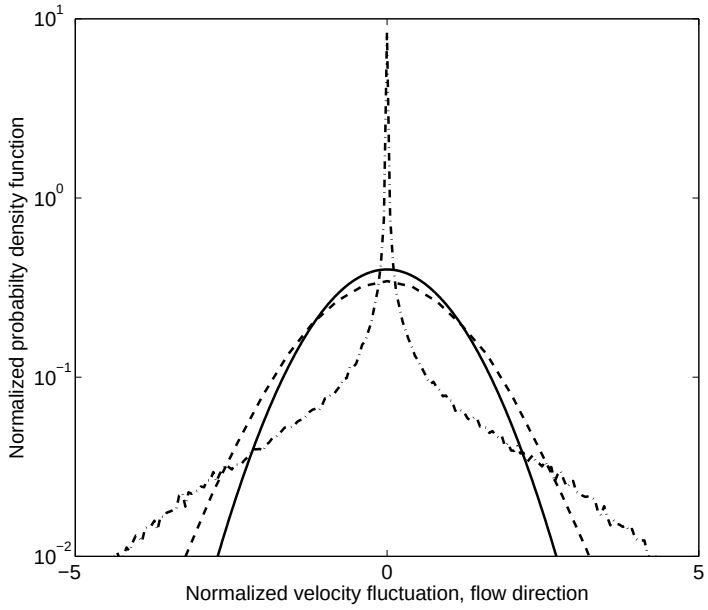

Figure 2.3: Velocity distribution function *vs.* normalized velocity fluctuations in the flow direction for $\alpha_p = 5$ %. ——— : Mawellian, - - - : $St = 5$, -·-·- : $St = 1$.

to be included in a Mawellian. The starting point for the unified theory is that a deviated Maxwellian is sufficient to predict both the ignited state and the quenched state if the collisional terms are calculated by taking all the contributions of the shear-induced collisions into account - i.e. not using Taylor developments. Hence we propose in this section to upgrade collisional terms of the ignited state theory in order to predict both high Stokes numbers and low Stokes numbers flows. We restrict our attention to the simple shear flow as described in Section 2.2.5.

2.3.2 Closure hypothesis

Collisional terms Eq. 2.9 are calculated using the modified molecular chaos assumption Eq. 2.10 to close the complete pair distribution function. In a first step, the velocity distribution function is assumed to be a Maxwelian, yielding for Eq. 2.9:

$$C(\Psi) = \frac{g_0\, d_p^2\, n_p^2}{(2\pi T)^3} \iiint_{\mathbf{g}\cdot\mathbf{k}>0} \delta\Psi_a \; exp(-\frac{\mathbf{C_a}^2}{2T}) \; exp(-\frac{\mathbf{C_b}^2}{2T}) \; (\mathbf{g}\cdot\mathbf{k}) \; \mathbf{dk} \; \mathbf{dc_a dc_b} \qquad (2.46)$$

where $\mathbf{C_a} = \mathbf{c_a} - \mathbf{U_p}(\mathbf{x})$ and $\mathbf{C_b} = \mathbf{c_b} - \mathbf{U_p}(\mathbf{x} + d_p\mathbf{k})$. In this case, the relative velocity $\mathbf{g} = \mathbf{c_a} - \mathbf{c_b}$ can be expressed according to the relative fluctuating velocity $\mathbf{G} = \mathbf{C_a} - \mathbf{C_b}$

and the increment of mean velocity $\delta\mathbf{U_p}$, defined Eq. 2.40, as:

$$\mathbf{g} = \mathbf{G} - \delta\mathbf{U_p} \tag{2.47}$$

The two terms of the right-hand-side of Eq. 2.47 are respectively the contribution of the particle agitation and of the shear. In a highly agitated suspension $T \gg \gamma^2 a^2$, hence $\mathbf{g} \sim \mathbf{G}$. In contrast, in a weakly agitated suspension $T \ll \gamma^2 a^2$, hence $\mathbf{g} \sim -\delta\mathbf{U_p}$. Consequently the two sources of collisions are taken into account. In this case, the $\mathbf{g}\cdot\mathbf{k} > 0$ condition appearing in Eq. 2.46 becomes:

$$x > \frac{k_x k_z}{\sqrt{T^*}} \tag{2.48}$$

where $x = (\mathbf{G}\cdot\mathbf{k})/(2\sqrt{T})$. Eq. 2.46 is integrated using the variable change $(\mathbf{C_a}, \mathbf{C_b}) \rightarrow (\mathbf{G}, \mathbf{Q} = (\mathbf{C_a} + \mathbf{C_b})/2)$, leading to:

$$C(\Psi) = \frac{g_0\, d_p^2\, n_p^2}{(2\pi T)^3} \iiint_{\mathbf{g}\cdot\mathbf{k}>0} \delta\Psi_a \; exp(-\frac{\mathbf{G}^2}{4T}) \; exp(-\frac{\mathbf{Q}^2}{T}) \; (\mathbf{g}\cdot\mathbf{k}) \; \mathbf{dG}\, \mathbf{dQ}\, \mathbf{dk} \tag{2.49}$$

C_{ij} can be directly calculated from Eq. 2.49 but we propose to decompose it into the sum of a source term and a flux term.

2.3.3 Source-flux decomposition

The collisional terms C_{ij} can be decomposed into a source contribution and a flux decomposition. By noting $\Psi_{a,ij} = m_p C_{a,i} C_{a,j}$ and $\Psi_{b,ij} = m_p C_{b,i} C_{b,j}$, we define:

$$\Delta\Psi_{ij} = \delta\Psi_{a,ij} + \delta\Psi_{b,ij} \tag{2.50}$$

$$D\Psi_{ij} = \delta\Psi_{a,ij} - \delta\Psi_{b,ij} \tag{2.51}$$

$$\tag{2.52}$$

Consequently, $\delta\Psi_{a,ij} = (\Delta\Psi_{ij} + D\Psi_{ij})/2$ and $\delta\Psi_{b,ij} = (\Delta\Psi_{ij} - D\Psi_{ij})/2$ and Eq. 2.46 can be written as:

$$C_{ij} = \Xi_{ij} + D_{ij} \tag{2.53}$$

where Ξ_{ij} and D_{ij} are defined by:

$$\Xi_{ij} = \frac{1}{2}\, d_p^2 \iiint_{\mathbf{g}\cdot\mathbf{k}>0} \Delta\Psi_{ij} \; f_p^{(2)}(\mathbf{c_a}, \mathbf{x}, \mathbf{c_b}, \mathbf{x} + d_p\mathbf{k}, t) \; (\mathbf{g}\cdot\mathbf{k}) \; \mathbf{dk}\, \mathbf{dc_a}\, \mathbf{dc_b} \tag{2.54}$$

$$D_{ij} = \frac{1}{2}\, d_p^2 \iiint_{\mathbf{g}\cdot\mathbf{k}>0} D\Psi_{ij} \; f_p^{(2)}(\mathbf{c_a}, \mathbf{x}, \mathbf{c_b}, \mathbf{x} + d_p\mathbf{k}, t) \; (\mathbf{g}\cdot\mathbf{k}) \; \mathbf{dk}\, \mathbf{dc_a}\, \mathbf{dc_b} \tag{2.55}$$

It should be noted that Ξ_{ij} is different from χ_{ij} as defined by Eq. 2.17 because, in this case, the fluctuating velocities are defined with reference to the position of the particles - i.e. the $\mathbf{x}$ position for the a particle, and the $\mathbf{x} + d_p\mathbf{k}$ for the b particle - whereas they were defined in reference of the $\mathbf{x}$ position in Eq. 2.17. In other words, $\mathbf{C_b} = \mathbf{c_b} - \mathbf{U_p}(\mathbf{x} + d_p\mathbf{k})$ in this theory, whereas $\mathbf{C_b} = \mathbf{c_b} - \mathbf{U_p}(\mathbf{x})$ in the ignited state theory.

Collision laws Eqs. 2.1 and 2.2 give:

$$\begin{aligned} \Delta\Psi_{ij} &= \frac{m_p}{2}\,(1+e_c)^2\,(\mathbf{g}\cdot\mathbf{k})^2\,k_i k_j \\ &- \frac{m_p}{2}\,(1+e_c)\,(\mathbf{g}\cdot\mathbf{k})\,(G_i\,k_j + G_j\,k_i) \end{aligned} \tag{2.56}$$

$$D\Psi_{ij} = -\,m_p\,(1+e_c)\,(\mathbf{g}\cdot\mathbf{k})\,(Q_i\,k_j + Q_j\,k_i) \tag{2.57}$$

As the integration over $\mathbf{Q}$ is performed for both positive and negative values, we have $D_{ij} = 0$. Consequently:

$$C_{ij} = \Xi_{ij} \tag{2.58}$$

The collisional terms C_{ij} are equal to the half of the variation for the pair of particles when the fluctuating velocities are defined in reference to the position of the particles. Moreover, $\Delta\Psi_{ij}$ could be expressed as:

$$\begin{aligned} \Delta\Psi_{ij} &= \Delta(m_p c_i c_j) \\ &- \delta U_{p,i}\cdot\delta(m_p c_{b,j}) - \delta U_{p,j}\cdot\delta(m_p c_{b,i}) \end{aligned} \tag{2.59}$$

where $\Delta(m_p c_i c_j) = \delta(m_p c_{a,j}) + \delta(m_p c_{b,j})$. The increment of mean velocity is related to the velocity gradient by:

$$\delta U_{p,i} = d_p\,k_k\,\frac{\partial U_{p,i}}{\partial x_k} \tag{2.60}$$

Substituting Eqs. 2.59 with Eq. 2.60 in Eq. 2.58 leads to:

$$C_{ij} = \chi_{ij} - \theta_{ik}\frac{\partial U_{p,j}}{\partial x_k} - \theta_{jk}\frac{\partial U_{p,i}}{\partial x_k} \tag{2.61}$$

where χ_{ij} and θ_{ij} are defined by:

$$\chi_{ij} = \frac{1}{2}\,d_p^2 \iiint_{\mathbf{g}\cdot\mathbf{k}>0} \Delta(m_p c_i c_j)\; f_p^{(2)}(\mathbf{c_a}, \mathbf{x}, \mathbf{c_b}, \mathbf{x} + d_p\mathbf{k}, t)\;(\mathbf{g}\cdot\mathbf{k})\;\mathbf{dk}\;\mathbf{dc_a dc_b} \tag{2.62}$$

$$\theta_{ij} = \frac{1}{2}\,d_p^3 \iiint_{\mathbf{g}\cdot\mathbf{k}>0} \delta(m_p c_{b,i})\;k_j\;f_p^{(2)}(\mathbf{c_a}, \mathbf{x}, \mathbf{c_b}, \mathbf{x} + d_p\mathbf{k}, t)\;(\mathbf{g}\cdot\mathbf{k})\;\mathbf{dk}\;\mathbf{dc_a dc_b} \tag{2.63}$$

In contrast to Eq. 2.20 obtained by Taylor developments, the proposed decomposition Eq. 2.61 is an exact expression. As in Eq. 2.49, the integration is performed using $\mathbf{G}$ and $\mathbf{Q}$ instead of $\mathbf{c_a}$ and $\mathbf{c_b}$.

2.3.4 Collisional terms expression

Resulting expressions for C_{ij} are given in Appendix B. For instance, C_{ii} appearing in the balance law of the particle agitation is:

$$\begin{aligned} C_{ii} &= -(1-e_c^2)\ \frac{\alpha_p\rho_p}{\tau_c}\ T\ A_{3,0} \\ &+ 2\gamma\ \frac{4}{5}\ \alpha_p\rho_p\ \alpha_p g_0\ d_p\ (1+e_c)\gamma\sqrt{\frac{T}{\pi}}\ B_{2,0} \end{aligned} \tag{2.64}$$

where $\tau_c = (24\alpha_p g_0\sqrt{T/\pi}/d_p)^{-1}$ is the expression of the collisional time given by the ignited state theory and $A_{3,0}$ et $B_{2,0}$ are functions of T^* defined by:

$$A_{3,0}(T^*) = \frac{1}{2\pi}\ \int_{\mathbf{k}} f_{3,0}\left(\frac{k_x\,k_z}{\sqrt{T^*}}\right)\ \mathbf{dk} \tag{2.65}$$

$$B_{2,0}(T^*) = -\frac{15}{4\pi}\ \sqrt{T^*}\ \int_{\mathbf{k}} f_{2,0}\left(\frac{k_x\,k_z}{\sqrt{T^*}}\right)\ (k_x\,k_z)\ \mathbf{dk} \tag{2.66}$$

where $f_{n,p}(u) = \int_u^{+\infty}(x-u)^n\ x^p\ e^{-x^2}dx$. Figure 2.4 shows the evolution of $A_{3,0}$ and $B_{2,0}$ in function of T^*. When $T^* \gg 1$, $A_{3,0}$ and $B_{2,0}$ tend to one. Then C_{ii} Eq. 2.64 tends to the expression given by the ignited state theory. In contrast, for $T^* \ll 1$, $A_{3,0}$ and $B_{2,0}$ are equivalent to:

$$A_{3,0} \sim_0 \frac{1}{T^{*3/2}} \times \frac{8}{105\sqrt{\pi}} \tag{2.67}$$

$$B_{2,0} \sim_0 \frac{1}{T^{*1/2}} \times \frac{4}{7\sqrt{\pi}} \tag{2.68}$$

Then C_{ii} is equal to the expression given by the quenched state theory Eq. 2.42. Hence, the expression given by Eq. 2.64 is able to predict the value given by both the quenched state theory and the ignited state theory. The transition between the two theories depends on the value of T^*.

The previous development was performed with the velocity distribution function taken as a Maxwellian. When the latter is assumed to be a deviated Maxwellian, Eq. 2.12, terms proportional to $\widehat{R}_{p,ij}$ appear. To complete the previous development, those terms were assumed to be the same as the corresponding terms given by the ignited state theory. The resulting expressions are given in Appendix. B. This hypothesis was made for reasons of

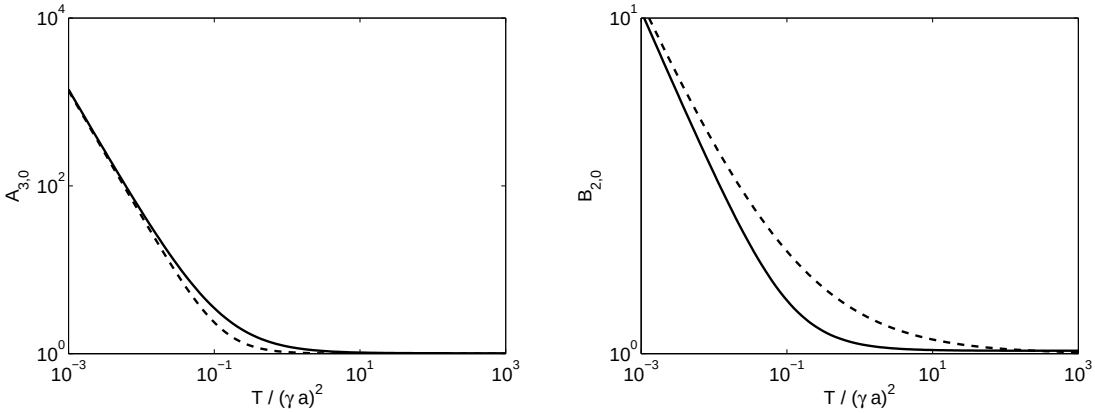

Figure 2.4: $A_{3,0}$ and $B_{2,0}$ *vs.* $T^* = T/(\gamma a)^2$. ——— : exact values, - - - : Eqs. 2.75 (left) and 2.76 (right).

simplicity but is justified *a posteriori* by the results obtained. It should be noted that this does not lead to isotropic results for small Stokes numbers because the proposed theory tends to the quenched state theory, which gives anisotropic results.

2.3.5 Comparison to Lagrangian simulations

Particle agitation

Theoretical predictions obtained with the unified theory and results of the Lagrangian simulation performed by Abbas et al. (2009) are compared in Figure 2.5. For $St > 5$, the unified theory leads to the same agitation as the one given by the ignited state theory. For $St = 1$, the proposed theory is in agreement with numerical results, yielding a transition from the quenched state theory to the ignited theory as the concentration increases. For $St = 3.5$, good agreement is found between the proposed theory and the numerical results. In particular for $\alpha_p = 5\%$, where both the quenched state theory and the ignited state theory lead to poor agreement. The transition between the ignited state and the quenched state occurs for $0.05 < T^* < 5$.

Anisotropy

The coefficient of anisotropy of the kinetic stress tensor is defined by:

$$a_{ij} = \frac{R_{p,ij} - T\,\delta_{ij}}{T} \tag{2.69}$$

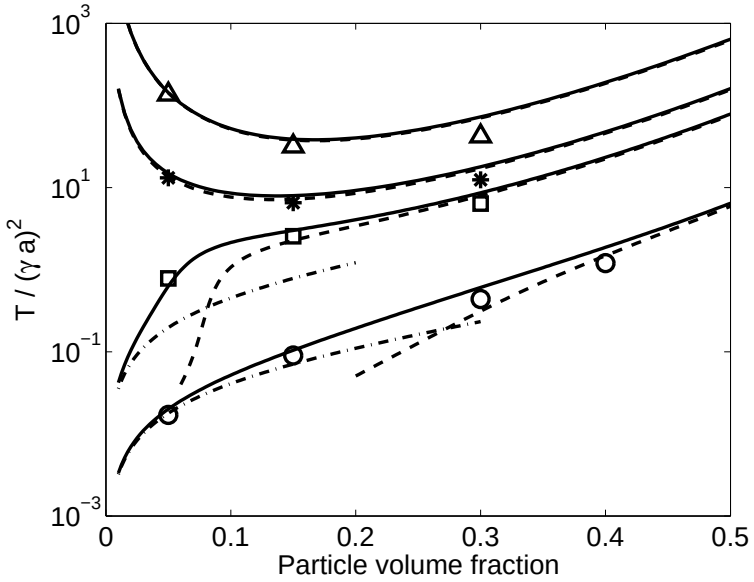

Figure 2.5: Particle agitation $T/(\gamma a)^2$ as a function of the particle volume fraction for different Stokes numbers. $\triangle$, $*$, $\square$ and O: numerical simulations for St = 10, 5, 3.5 and 1 respectively. —— : unified theory (from top to bottom, St = 10, 5, 3.5 and 1), - - - : ignited state theory (from top to bottom, St = 10, 5, 3.5 and 1), -·-·- : quenched state theory (from top to bottom, St = 3.5 and 1).

Boelle et al. (1995) measured a_{zz} and a_{xz} for a Lagrangian simulation with $St = 5$ and $e_c = 0.8$. They showed that the prediction of the ignited state theory highly overestimated a_{zz}, particularly in dense regions. According to the authors, this poor agreement can be attributed to the Taylor developments used to establish the ignited state theory. Consequently, the results predicted by the unified theory should lead to a better agreement. This is verified in Figure 2.6 where measures are compared to theoretical predictions. It is clearly shown that results are improved when the unified theory is used, while the particle agitation is well predicted by both theories. This fact is in agreement with the interpretation given by Boelle et al. (1995).

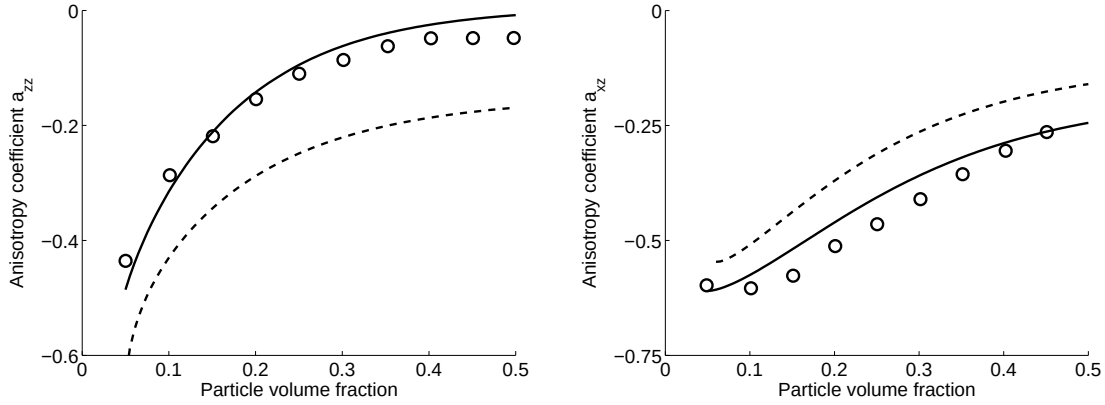

Figure 2.6: Anisotropy coefficients a_{zz} and a_{xz} as a function of the particle volume fraction, for $St = 5$ and $e_c = 0.8$. O: Lagrangian simulations (from Boelle et al. (1995)), ——: unified theory, - - - : ignited state theory.

Figures 2.7 and 2.8 compare predictions made by the theories with the results obtained by Abbas et al. (2010) for $e_c = 1$ and $St = 3.5$ and 1. The quenched state theory predicts a value independent of the particle volume fraction, which is reached for small particle volume fractions. A good agreement is found between the unified theory and the numerical results for the two Stokes numbers, in particular for $St = 1$, where both the quenched state theory and the ignited state theory fail to predict the anisotropy coefficients.

Multiple steady states

Using numerical simulations, Tsao and Koch (1995) have shown that multiple steady states can exist for low concentrations. Moreover, a hysteresis is observed when increasing the Stokes number at a fixed concentration and particle elasticity. As shown in Figure 2.9 where $\alpha_p = 5 \cdot 10^{-4}$ and $e_c = 1$, if the system is in the quenched state and St is increased

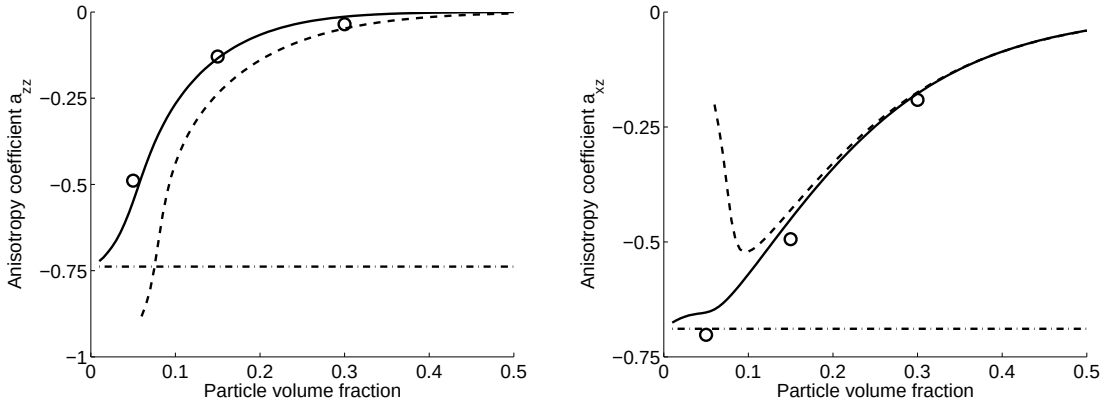

Figure 2.7: Anisotropy coefficients a_{zz} and a_{xz} as a function of the particle volume fraction, for $St = 3.5$ and $e_c = 1$. O: Lagrangian simulations (from Abbas et al. (2010)), ——: unified theory, – – – : ignited state theory, –·–·– : quenched state theory.

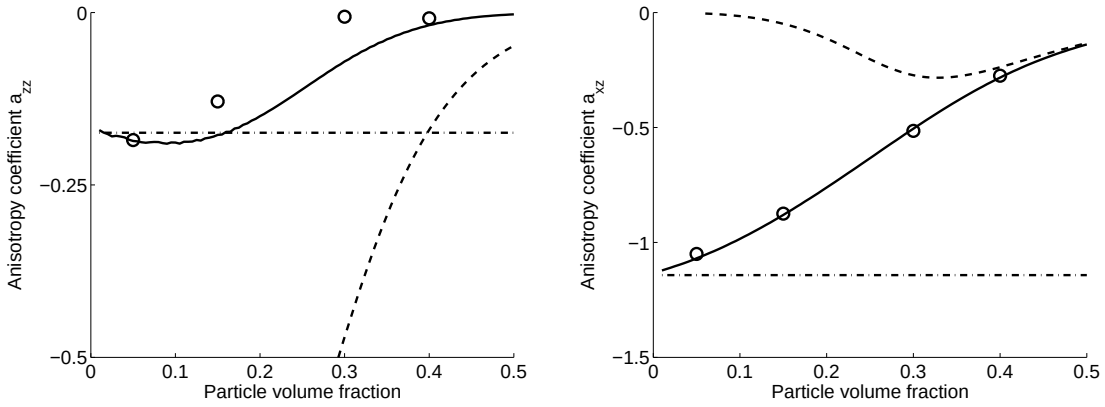

Figure 2.8: Anisotropy coefficients a_{zz} and a_{xz} as a function of the particle volume fraction, for $St = 1$ and $e_c = 1$. O: Lagrangian simulations (from Abbas et al. (2010)), ——: unified theory, – – – : ignited state theory, –·–·– : quenched state theory.

gradually, the system jumps to the ignited state for $St = St_{c2} \simeq 13$. If St is decreased gradually for a system in the ignited state, the system jumps down to the quenched state for $St = St_{c1} = \sqrt{24}$. Therefore, one may have either the ignited or quenched state for $St_{c1} < St < St_{c2}$ depending on the previous history of the shear rate experienced by the suspension. As shown in Figure 2.9, the unified theory is able to predict this hysteresis effect and the corresponding multiple steady states. The predicted critical Stokes numbers are $St_{c1} = \sqrt{24}$ and $St_{c2} \simeq 15$. The latter slightly overestimates the value given by numerical simulations.

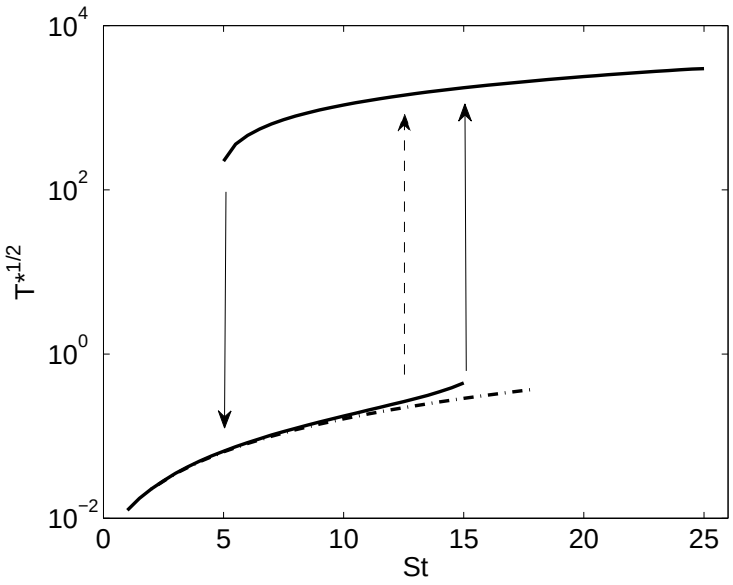

Figure 2.9: Particle agitation as a function of Stokes numbers for $\alpha_p = 5 \cdot 10^{-4}$ and $e_c = 1$. ——— : unified theory, -·-·- : quenched state theory, dashed arrow: transition obtained from numerical simlations (from Tsao and Koch (1995)).

2.3.6 Boussinesq assumption

A Boussinesq assumption could be made to establish the expressions for the kinematic and collisional viscosities:

$$\widehat{R}_{p,ij} = -2\ \nu_p^{kin} \widehat{D}_{p,ij} \tag{2.70}$$

$$\widehat{\theta}_{p,ij} = -2\ \nu_p^{coll} \widehat{D}_{p,ij} \tag{2.71}$$

Putting Eqs. 2.70 and 2.71 in the balance law of $R_{p,13}$ leads to:

$$\nu_p^{kin} = \frac{2}{3}\ q_p^2\ \frac{\tau_c}{\sigma_c}\ (1 + \alpha_p g_0 \phi_c^*)\ (1 + \frac{2}{\sigma_c}\ \frac{\tau_c}{\tau_p})^{-1} \tag{2.72}$$

where $\phi_c^* = \phi_c + 2\,(1+e_c)^2/(35\,T^*)$, $\phi_c = 2/5\ (1+e_c)(3e_c - 1)$ and $\sigma_c = (1+e_c)(3-e_c)/5$. The collisional viscosity is given by:

$$\nu_p^{coll} = \frac{4}{5}\,\alpha_p g_0\,(1+e_c)\ (\nu_p^{kin} + d_p \sqrt{\frac{T}{\pi}}\,B_{2,0}) \tag{2.73}$$

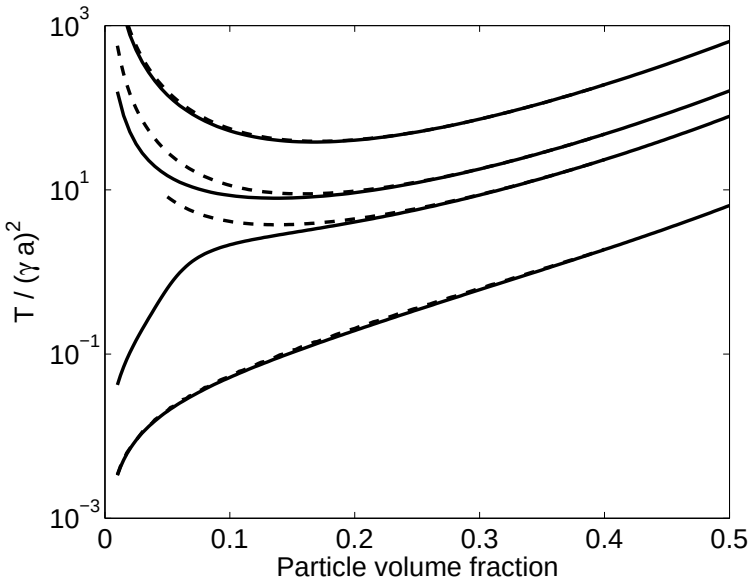

Figure 2.10: $T/(\gamma a)^2$ as a function of the particle volume fraction for $e_c = 1$. From bottom to top St = 10, 5, 3.5 and 1. ——— : unified theory, - - - : Boussinesq assumption for the unified theory.

When $T^* \gg 1$ the viscosity given by Boelle et al. (1995) is found. For $T^* \ll 1$, there is a non-null viscosity, which is the viscosity of the quenched state.

Solutions found by using the Boussinesq assumption and by solving the complete system are shown in Figure 2.10. For $St = 10$, the two solutions give identical results. For $St = 5$ and 3.5, the Boussinesq assumption leads to an overestimation of the particle agitation for low particle volume fraction ($\alpha_p \leq 20\,\%$). For $St = 1$ the Boussinesq assumption leads to the correct particle agitation for any particle volume fraction. Consequently, the Boussinesq assumption can be used for $St \geq 10$ or $St \leq 1$. However, the transition between the two states is not well predicted for low particle volume fraction.

The total particle pressure found is given by:

$$P_p = \frac{2}{3}\,\alpha_p \rho_p\, q_p^2\,(1 + 2\alpha_p g_0\,(1 + e_c)) + \frac{4}{15}\,\alpha_p \rho_p\,\alpha_p g_0\,(1 + e_c)\,(\gamma\, a)^2 \tag{2.74}$$

The last term of Eq. 2.74 is the contribution of shear-induced collisions.

2.3.7 Collisional terms additions

Tsao and Koch (1995) calculate collisional terms by adding contributions of the ignited state theory and the quenched state theory. This is equivalent to approximating $A_{n,p}$, $B_{n,p}$

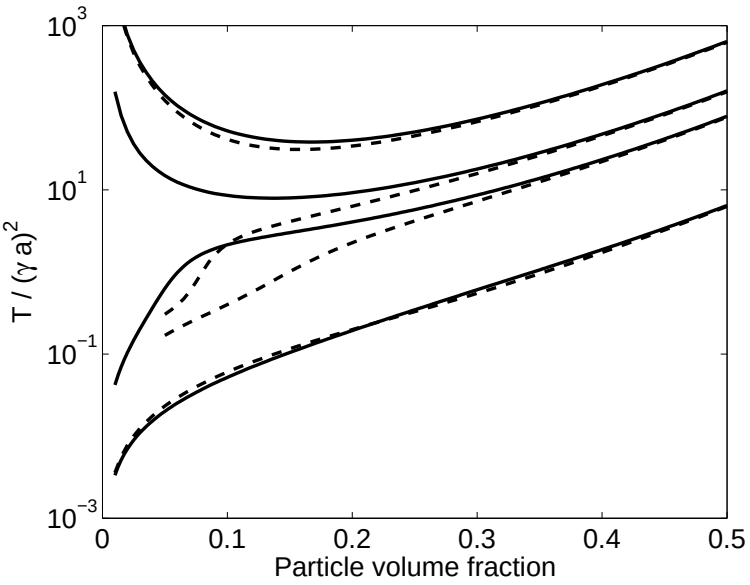

Figure 2.11: $T/(\gamma a)^2$ as a function of the particle volume fraction for $e_c = 1$. From bottom to top $St = 10$, 5, 3.5 et 1. ——— : unified theory, - - - : theory resulting to the collisional terms addition.

and $D_{n,p}$ functions by the sum of their asymptotic behaviour. For instance, for $A_{3,0}$ and $B_{2,0}$ this leads to:

$$A_{3,0} \simeq 1 + \frac{1}{T^{*3/2}} \times \frac{8}{105\sqrt{\pi}} \tag{2.75}$$

$$B_{2,0} \simeq 1 + \frac{1}{T^{*1/2}} \times \frac{4}{7\sqrt{\pi}} \tag{2.76}$$

Eqs. 2.75 and 2.76 and exact values of $A_{3,0}$ and $B_{2,0}$ are compared in Figure 2.4. The resulting particle agitations are shown in Figure 2.11. In the limit of $St \geq 10$ and $St \leq 1$, this assumption leads to the same results as the exact values. Nevertheless, when $St = 5$ or $St = 3.5$, this approximation is only adequate for $\alpha_p \geq 30\,\%$.

Correction of the ignited theory

A Taylor development of C_{ii}, Eq. 2.64, for high values of T^* leads to:

$$\begin{aligned} C_{ii} &\simeq -(1-e_c^2)\,\frac{\alpha_p \rho_p}{\tau_c}\,T \\ &+ 2\gamma\,\frac{4}{5}\,\alpha_p\rho_p\,\alpha_p g_0\,d_p\,(1+e_c)\gamma\sqrt{\frac{T}{\pi}} \end{aligned}$$

$$- \quad 2\gamma \, \frac{3}{5} \, \alpha_p \rho_p \, \alpha_p g_0 \, d_p \, (1 - e_c^2) \gamma \sqrt{\frac{T}{\pi}} \tag{2.77}$$

The first term of the r.h.s of Eq. 2.77 comes from χ_{ii} in the ignited sate theory. The second term is the isotropic contribution of θ_{13}. The last term, which does not appear in the ignited state theory, comes from the second order term in the expression of χ_{ii}. This term is of the same order as the other terms and should be taken into account as noted by Jenkins and Richman (1985).

2.3.8 Conclusion

We have proposed a new way of calculating the collisional terms appearing in the balance laws of the kinetic stress tensor. Good agreement is found with Lagrangian simulation for both the particle agitation and the anisotropy coefficient for Stokes numbers between 1 and 10 and particle volume fractions between 5 % and 30 %. For small particle volume fraction, the theory shows the hysteresis behaviour found in numerical simulations. Moreover, this theory allow us to highlight some missing terms in the ignited state theory.

Lagrangian simulations have shown that particle agitation is underestimated by the standard two-fluid model when the Stokes number is small. In this case, the effect of clustering of particles is overestimated because the particle pressure is diminished. Consequently, if corrections are made, leading to the correct particle agitation in a fluidized bed, the effect would be to increase the bed expansion. As the bed expansion is considerably overestimated when using standard two-fluid models, such modifications would not lead to a better agreement with measurements.

2.4 Hydrodynamic effects

2.4.1 Introduction

In Section 2.3, we looked at the macroscopic behaviour of suspensions where drag and particle inelasticity are the only mechanisms of energy dissipation. Actually, other physical mechanisms of dissipation may exist: local hydrodynamic interactions (possibly multi-body for dense suspensions), film drainage during a collision and inelastic deformation of the particles. All these phenomena modify the energy budget and may induce a significant reduction of the particle agitation.

In addition to the drag and collision dissipation mechanisms, Sangani et al. (1996) took the local hydrodynamic interactions into account in the energy conservation equation in the limit of vanishing Reynolds number and moderate to high Stokes number. The

authors showed that the effect of hydrodynamic interactions could be simply modelled by a corrective function $R_{diss}(\alpha_p)$ applied to the Stokes drag on each particle trajectory. This model compared favourably with simulations accounting for hydrodynamic interactions through the Stokesian Dynamics approach. Using this correction prefactor is similar to a reduction of the overall Stokes number of the suspension flow.

The influence of lubrication effects is investigated using the model provided by Legendre et al. (2006), which include the lubrication effects occurring during a collision by modifying the restitution coefficient. The modification of the collisional terms is looked at. Theoretical developments are assessed using discrete particle simulations of a shear flow. The range of parameters will lead to both the quenched and ignited states and results will be compared with the reference case of perfectly elastic particles.

2.4.2 Restitution coefficient including hydrodynamic effects

Local hydrodynamic interactions occurring during a collision lead to significant reduction of the particle relative velocity before and after impact on a length scale of the same order as or shorter than the radius of particles (see experiments for particles in glycerol solution (Joseph et al., 2001; Yang and Hunt, 2006) or drops in water (Legendre et al., 2006)). Lubrication forces during the film drainage delay the physical contact and induce a strong dissipation of the kinetic energy of the particles involved in the collision. This can be viewed as an effective restitution coefficient related to the real inelasticity of the particle material supplemented by the local dissipation of the particle kinetic energy by the surrounding fluid. Legendre et al. (2006) propose an empirical law for the effective coefficient of restitution for a particle-wall collision $e_{pw} = e_0\ exp(-\frac{\beta}{St_\infty})$ where V_∞ is the velocity of the particle before its interaction with the wall, and $St_\infty = \frac{m_p V_\infty}{6\pi\mu a^2}$ is the corresponding Stokes number. e_0 is the maximum restitution coefficient obtained in a dry collision and β an empirical parameter equal to 35.

For a collision of two identical particles, Yang and Hunt (2006) found that the evolution of the restitution coefficient followed the same trend as for particle-wall collisions with a Stokes number based on a reduced particle mass m^* and radius a^* ($m^* = m_p$ and $a^* = a$ for particle-wall collisions whereas $m^* = m_p/2$ and $a^* = a/2$ for two-particle collisions). The effective particle-particle restitution coefficient e_{pp} depends on impact parameters and particle characteristics as follows:

$$e_{pp} = e_0\ exp(-\frac{V_\beta}{V_{r,\infty}}) \tag{2.78}$$

where $V_\beta = \frac{\beta}{2}\frac{a}{\tau_p}$ and $V_{r,\infty}$ is the relative velocity of the two particles before collision.

2.4.3 Simple shear flow

The simple shear flow is used to investigate the effect of the restitution coefficient depending of the relative velocities of colliding particles. Spherical particles are put in an infinite sheared gas flow. The fluid velocity $\mathbf{U_g}(\mathbf{x})$ is assumed to be unperturbed by the presence of particles, and given by:

$$\frac{\partial U_{g,i}}{\partial x_j} = \gamma\ \delta_{i,1}\ \delta_{j,3} \tag{2.79}$$

with γ the shear rate and $\delta_{i,j}$ the Kronecker delta. Flow is assumed to be homogeneous. Particles are considered as hard spheres that experience only Stokes drag force and binary collisions, which is valid for low to moderate solid concentration. The post-collision velocities $\mathbf{c_a}^*$ and $\mathbf{c_b}^*$ of two colliding particles a and b are determined in function of $\mathbf{c_a}$ and $\mathbf{c_b}$, the particles' velocities at impact:

$$\mathbf{c_a}^* = \mathbf{c_a} - \frac{1}{2}(1+e_{pp})\ (\mathbf{g}\cdot\mathbf{k})\ \mathbf{k} \tag{2.80}$$

$$\mathbf{c_b}^* = \mathbf{c_b} + \frac{1}{2}(1+e_{pp})\ (\mathbf{g}\cdot\mathbf{k})\ \mathbf{k} \tag{2.81}$$

where e_{pp} is the elasticity coefficient given by Eq. 2.78, with $V_{r,\infty} = \mathbf{g}\cdot\mathbf{k}$. In the steady state, the particle velocity field is equal to the gas velocity field: $\mathbf{U_p}(\mathbf{x}) = \mathbf{U_g}(\mathbf{x})$.

2.4.4 Numerical simulations

Discrete particle simulations in a periodic cubic box are carried out to test the accuracy of the theoretical predictions. Particles are initially seeded at non-overlapping random positions within the entire domain and their velocity is randomly choose. A fixed time step dt is used for time integration of the trajectories using a first-order scheme. After the end of the new time step, overlapping particles are detected and the exact collision time of each collision ($t + \delta t$ where $\delta t < dt$) is precisely determined between t and $t + dt$. The post-collision velocities are determined in function of the particles' velocities at the exact time of collision, using Eqs. 2.80 and 2.81.

The ratio between the cubic box width L and particle size is kept constant (L/a). Periodic boundary conditions in the three directions of space help to preserve the homogeneity of the suspension under shear. When a particle leaves the simulation domain from the bottom (respectively top) boundary, it appears on the opposite side and its velocity is adapted by adding (respectively subtracting) the velocity γL. This is equivalent to apply-

ing the shear in a dynamic way by means of the Lees-Edward boundary conditions (Allen and Tildesley, 1990). The ratio $L/a \approx 48$ between the domain width L and the particle radius was selected by fitting the two following constraints: not too large so as to prevent the formation of layers populated with particles (Campbell, 1990) and not too small, so that each particle may encounter many collisions when travelling between two opposite boundaries. Various volumetric concentrations of the suspension are simulated by varying the total number of particles (1 320, 3 960 and 7 920 particles corresponding to $\alpha_p = 5\%$, 15% and 30% respectively). The time step is initially set small relative to particle relaxation time and collision time estimated using kinetic theory. Then it is decreased until the statistical convergence of particle agitation is reached. After the initial seeding, all the statistics evolve in a transient regime which is not considered in the analysis. Then, the flow of the suspension is simulated for a time long enough to guarantee the convergence of the statistics. Typically, each particle was allowed to experience at least 600 collisions.

The particle radius a and the shear rate γ^{-1} are used respectively as length and time scales for normalizing all the statistical quantities. As no multiple steady states are found in the range of parameters used, the dimensionless particle agitation is a function of α_p, e_0, β and $St = \gamma\tau_p$.

2.4.5 Integration into the Eulerian formalism

The particle-fluid interaction can be modelled by two contributions: the standard drag force when particles are far apart from each other, and the direct hydrodynamic interaction (or lubrication effect) taken into account through the modification of the restitution coefficient (Eq. 2.78). Our approach is based on the description of the hydrodynamic effects in an efficient restitution coefficient. It is only valid when the time scale of the drag force τ_p is much larger than the time scale of the lubrication forces τ_L.

In the ignited regime, the lubrication time scale can be estimated by $\tau_L = \frac{a}{2}\sqrt{\frac{\pi}{T}}$ since lubrication effects occur over a distance typically $O(2a)$ (Legendre et al., 2006) with a mean relative velocity $O(\sqrt{\frac{24}{\pi}T})$. The condition $\tau_p \gg \tau_L$ is then satisfied when $T/(\gamma^2 a^2) \gg \pi/(4St^2)$.

In the quenched state, the typical particle-particle relative velocity can be estimated by γa, and the condition $\tau_p \gg \tau_L$ therefore leads to $St \gg 1$, in contradiction with the moderate particle inertia assumption. Consequently, the application of the proposed approach for direct hydrodynamic interaction modelling should be restricted to the ignited regime.

Based on similar assumptions of the highly agitated regime for the velocity distribution function (see Section 2.2.3), we obtain the distribution function of the relative velocity at

impact **g.k**. Then, using Eq. 2.78 with $V_{r,\infty} = \mathbf{g.k}$, we can deduce the distribution of the restitution coefficient $f(e^*)$, with $e^* = e_{pp}/e_0$:

$$f(e^*) = -\frac{1}{T_\beta}\ \frac{1}{e^*\ ln^3(e^*)}\ exp(-\frac{1}{4\ T_\beta\ ln^2(e^*)}) \tag{2.82}$$

where $T_\beta = \frac{T}{V_\beta^2} = \frac{4}{\beta^2}\ St^2\ \frac{T}{\gamma^2 a^2}$. The average restitution coefficient is obtained by integrating

$$< e_{pp} >= e_0\ \int_0^1 e^*\ f(e^*)\ de^* = 2\ e_0 \int_0^{+\infty} u\ e^{-u^2}\ e^{-1/(2\ T_\beta^{1/2} u)}\ du \tag{2.83}$$

Assuming that $T_\beta \gg 1$, which is a reliable assumption for high Stokes numbers, an analytic expression for $< e_{pp} >$ is obtained by a Taylor expansion:

$$< e_{pp} > \simeq e_0\ \left(1 - \frac{1}{2}\ \sqrt{\frac{\pi}{T_\beta}}\right) \tag{2.84}$$

Theoretical expression of the restitution coefficient distribution Eq. 2.82 is compared to discrete particle simulations in Figures 2.12 and 2.13. The the maximum restitution coefficient is $e_0 = 1$. For $\alpha_p = 5\%$, a very good agreement is found for $St = 10$ and 50 while large discrepancies are found for $St = 5$ (see Figure. 2.12). It shows that the assumptions of the ignited regime do not apply for this Stokes number. When the Stokes number decreases, the particle agitation decreases, leading to a significant reduction of the mean restitution coefficient. Figure 2.13 shows the effect of increasing the particle volume fraction on the distribution function of the restitution coefficient, for $St = 10$. As the particle volume fraction increases, the mean restitution coefficient decreases. As shown by Eq. 2.84 this is consequence of the reduction of the particle agitation.

Modifications of the collisional terms in the balance laws of the kinetic stress tensor was investigated for both the quenched and agitated regimes. In the ignited regime, this leads to the modification of the collisional terms χ_{ij} and θ_{ij} where the coefficient of restitution has to be multiplied by correction prefactors R_{np} defined by:

$$R_{np} = \left(\frac{1}{I_n} \int_0^{+\infty} e^{-p/(2\ T_\beta^{1/2} u)}\ u^n\ e^{-u^2}\ du\right)^{\frac{1}{p}} \tag{2.85}$$

where I_n are constants defined by $I_n = \int_0^{+\infty} u^n\ e^{-u^2}\ du$. For instance, the kinetic agitation dissipation induced by the particle collisions is:

$$\frac{\chi_{ii}}{2} = -\frac{T}{2}\ \frac{\alpha_p\ \rho_p}{\tau_c}\ \left(1 - (R_{32}\ e_0)^2\right) \tag{2.86}$$

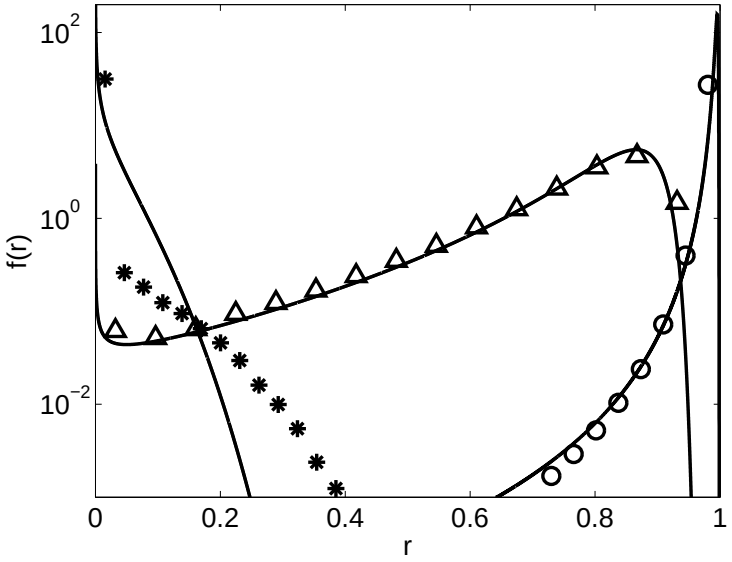

Figure 2.12: Probability density function of the restitution coefficient depending on the impact velocities for $\alpha_p = 5\%$. —— : Eq. 2.82, $\circ$, $\triangle$ and $*$: numerical simulations for $St = 50$, 10 and 5, respectively.

Assuming that R_{np} has an exponential form, a first order Taylor expansion of Eq. 2.85 yields $R_{np} \simeq e^{-I_{n-1}/(2I_n T_\beta^{1/2})} = R_n$. Therefore, the energy dissipation can be approximated by Eq. 2.87. For more details of the modification of the ignited theory the reader is referred to Appendix C.

$$\frac{\chi_{ii}}{2} \simeq -\frac{T}{2}\,\frac{\alpha_p\,\rho_p}{\tau_c}\,\left(1-(R_3\;e_0)^2\right) \tag{2.87}$$

In the quenched regime, the particle agitation is given by:

$$\frac{T}{\gamma^2 a^2} = \frac{1}{6}\;St\;C_{ii} - \frac{1}{6}\;St^2\;C_{13} + \frac{1}{12}\;St^3 C_{33} \tag{2.88}$$

where the terms C_{ij} denote the collisional terms equal to:

$$C_{ij} = -\frac{6}{\pi}\;\alpha_p g_0\;I_{ij}\;\left(1+2\;Q_{ij}(St)\;e_0 + Q_{ij}(St/2)\;e_0^2\right) \tag{2.89}$$

where I_{ij} are constants defined by $I_{ij} = \int_{k_x k_y<0}(k_x k_y)^3\;k_i k_j\;\mathbf{dk}$ and Q_{ij} are obtained by:

$$Q_{ij} = \frac{1}{I_{ij}}\;\int_{k_x k_y<0} exp(\frac{\beta}{4\;St\;k_x k_y})\;(k_x k_y)^3\;k_i k_j\;\mathbf{dk} \tag{2.90}$$

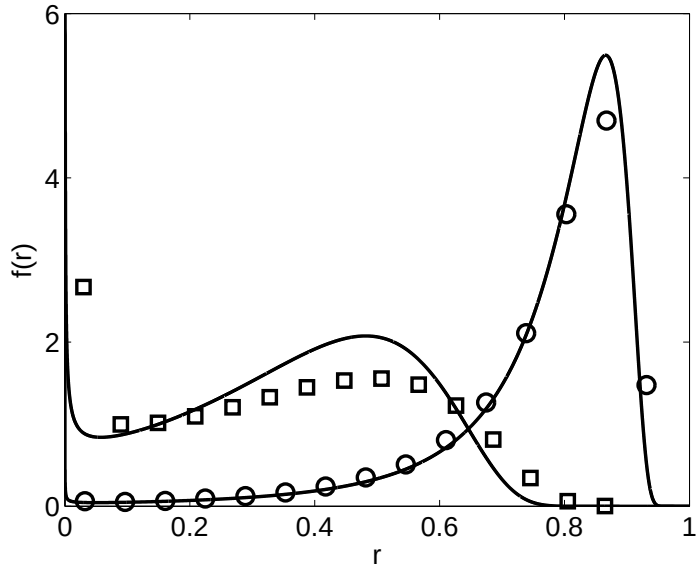

Figure 2.13: Probability density functions of the restitution coefficient depending on the impact velocities for $St = 10$. ——: Eq. 2.82, $\circ$ and $\square$: numerical simulations for $\alpha_p = 5\%$ and 15%, respectively.

Assuming that $Q_{ij} \simeq exp(-\frac{\beta\ a_{ij}}{4\ St})$, a first order Taylor expansion yields an analytic expression for the symmetric tensor a_{ij} in Q_{ij} ($a_{11} = a_{33} = \frac{27\pi}{32}$, $a_{22} = \frac{9\pi}{8}$, $a_{13} = \frac{8}{\pi}$ and $a_{12} = a_{23} = 0$). Finally, the collisional terms are obtained by:

$$C_{ij} \simeq -\frac{6}{\pi}\ \alpha_p g_0\ I_{ij}\ \ (1 +\ Q_{ij}\ e_0)^2 \tag{2.91}$$

Figure 2.14 shows the evolution of the particle agitation with concentration for $St = 5, 10$ and 50. The numerical results are compared to the corresponding modified theory. Very good agreement is obtained for $St = 50$ for any concentration and for $St = 5$ and 10 at low concentration (i.e. $\alpha_p = 5\%$). Figure 2.14 also shows the theoretical predictions for perfectly elastic collisions $e = 1$. Compared to the reference case $e = 1$, the level of particle agitation is significantly reduced. For instance when $St = 50$, the level of agitation is reduced by factors of 4 and 25 for $\alpha_p = 5\%$ and $\alpha_p = 15\%$, respectively.

Figure 2.15 shows the dependence of the effective restitution coefficient $R_3\ e_0$ (appearing in χ_{ii}, Eq. 2.87) on the Stokes number for several particle concentrations. At large Stokes number, the effective restitution coefficient tends asymptotically towards e_0. For $St = 50$, the effective restitution coefficient is equal to 0.995 e_0 and 0.98 e_0, for $\alpha_p = 5\%$ and

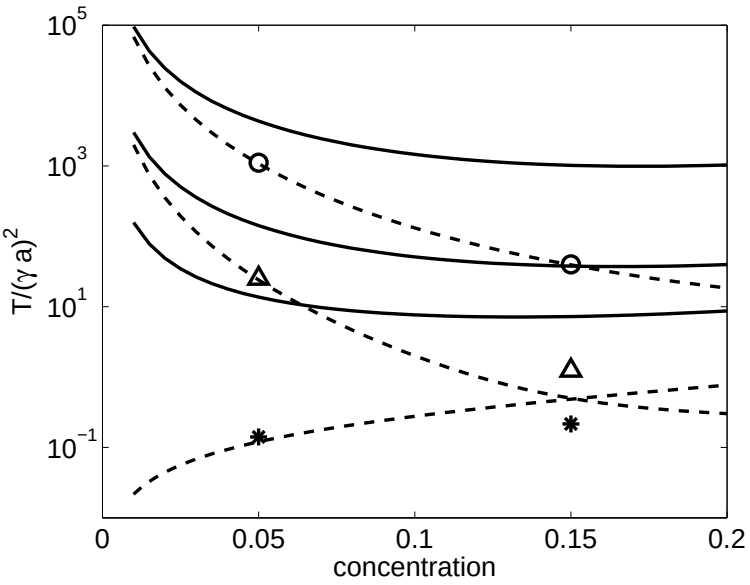

Figure 2.14: Particle agitation *vs.* concentration for different Stokes numbers. Symbols stand for the numerical simulations. ∘: $St = 50$, △: $St = 10$, ∗: $St = 5$. Lines are theoretical predictions. ——— : $e_c = 1$ (from top to bottom: $St = 50$, 10 and 5), - - - : modified ignited theory (from top to bottom: $St = 50$, 10) and modified quenched theory for $St = 5$.

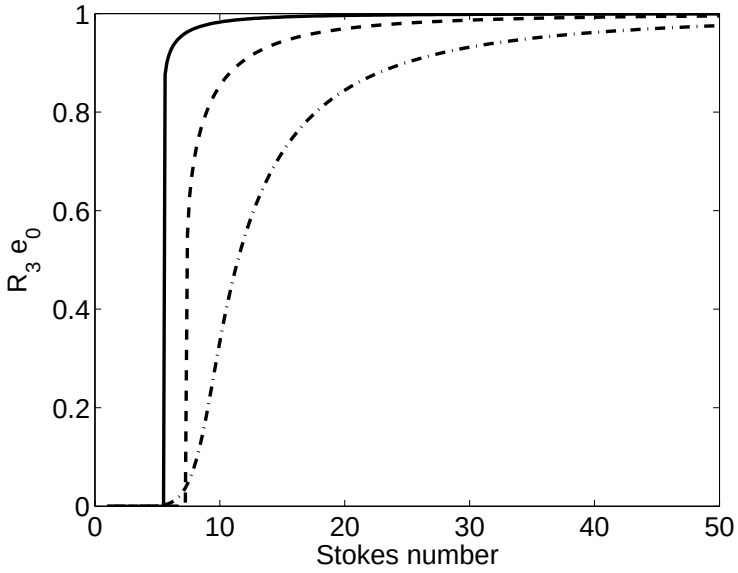

Figure 2.15: Effective coefficient of restitution $R_3\ e_0$ *vs.* Stokes number for different particle volume fraction, for $e_0 = 1$. —— : $\alpha_p = 5\%$, - - - : $\alpha_p = 10\%$, -·-·- : $\alpha_p = 15\%$.

$\alpha_p = 15\%$ respectively.

A comparison of the energy dissipation ratio (collision/drag dissipations) is presented in Figure 2.16 for the standard (constant restitution coefficient) and extended ignited theory (*i.e.* variable restitution coefficient). For $\alpha_p = 5\%$, we consider two cases in particular, corresponding to maximum restitution coefficients $e_0 = 1$ and $e_0 = 0.9$. In the case $e_0 = 1$, $St = 50$ and $\alpha_p = 5\%$, both dissipation mechanisms (inelastic collisions and drag) are of the same magnitude. This explains why a very weak variation of the effective restitution coefficient (ie. 0.5% for that case) has a dramatic effect on the particle agitation (reduced by a factor of 4 compared to the reference case). However, when $e_0 = 0.9$, the trend of the dissipation ratio increase is similar when the restitution coefficient is constant or varies with the impact parameters (at $St = 50$ there is only a 10% difference). This means that the modelling of direct hydrodynamic interactions has a weak influence on the particle agitation for inelastic particles.

Unexpectedly, when $e_0 = 1$, the energy dissipation ratio is constant when $St > 10$. Assuming that $T_\beta \gg 1$, the ratio of energy dissipation can be expressed as:

$$\frac{1}{2}\,\frac{\tau_p}{\tau_c}\,\left(1-(R_{32}\ e_0)^2\right) \simeq \frac{1}{2}\,\frac{\tau_p}{\tau_c}\,(1-e_0^2) + \frac{3}{2}\,\alpha_p\, g_0\ e_0^2\ \beta \tag{2.92}$$

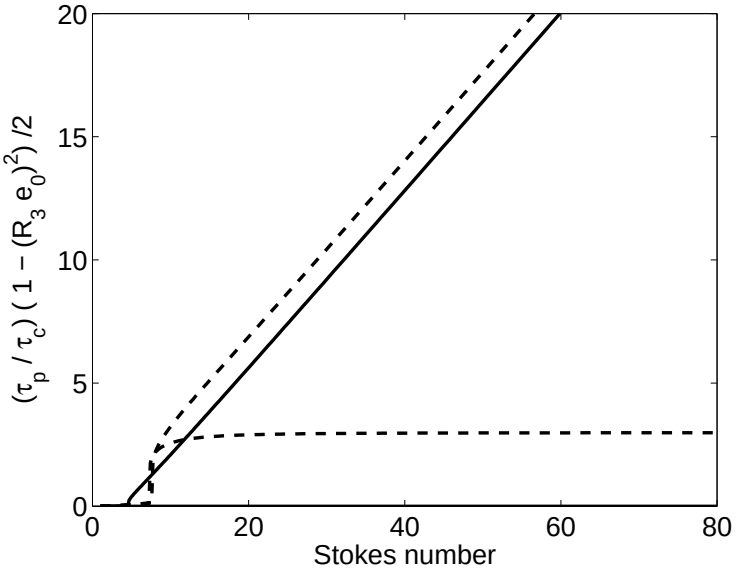

Figure 2.16: Ratio of the two mechanisms of energy dissipation (collision/drag) *vs.* Stokes number for $\alpha_p = 5\%$. —— : standard ignited theory with $e_c = 0.9$, - - - : modified ignited theory (from top to bottom: $e_0 = 0.9$ and $e_0 = 1$).

Eq. 2.92 shows that, in the particular case of $e_0 = 1$, the dissipation ratio is asymptotically independent of St. However, the magnitude of the dissipation ration is proportional to $\alpha_p g_0$ which accounts for the effect the particle volume fraction.

2.4.6 Conclusion

We used the simple modelling of local hydrodynamic interactions occurring during each binary collision proposed by Legendre et al. (2006). The damping effect of the fluid drainage was modelled by an equivalent restitution coefficient depending on the instantaneous particle impact velocities. The instantaneous restitution coefficient is related to the binary Stokes number based on impact parameters. The predictions based on the kinetic theory for the ignited and quenched states were extended to take this effect into account. We found very good agreement with numerical simulations at low concentration (ie. $\alpha_p = 5\%$). At moderate concentration (ie. $\alpha_p = 15\%$) the theory was very efficient for high Stokes number. The distribution of the restitution coefficient was compared to the assumption used in the theory as a validation step. This helped to limit the range of accuracy of our statistical approach. At high Stokes numbers, the effective restitution coefficient is slightly different

from the reference case. Including the effect of binary hydrodynamic interactions leads to more pronounced effects at moderately concentrated to dense suspensions or moderate Stokes numbers.

In consequence, the hydrodynamic effects between particles is to reduce the efficient restitution coefficient. However, as shown by Li and Kuipers (2003), the restitution coefficient does not have a significant impact on the bed expansion in the considered flow regimes.

2.5 Inter-particular forces

2.5.1 Introduction

Ferschneider and Mege (1996), McKeen and Pugsley (2003) and Makkawi et al. (2006) argue that the over-prediction of bed expansion with Geldart A particles can be attributed to the role of Van der Waals forces between particles. Such forces should lead to the formation of clusters, resulting in an overall smaller drag force acting on the particle bed. By performing discrete particle simulations of 2D fluidized bed, Ye et al. (2004) found that, in the bubbling regime, the effect of inter-particle van der Waals forces vanished and the fluid-particle interaction became the dominant factor determining the fluidization behaviour of Geldart A particles.

Our approach is to integrate such forces into the standard two-fluid model in a theoretical way by using the BBGKY hierarchy (He and Doolen, 2002) used to describe rarified gases. We will identify the first order effect, which is the introduction of a negative contribution to the particle pressure.

2.5.2 Interaction potential between two particles

Particle interactions can be decomposed into a repulsive short-range part and an attractive long-range part. The repulsive part is taken into account in the kinetic theory of granular flow during instantaneous collisions. The attractive part is the Van der Waals force. While the interaction potential is well known for two molecules, it remains difficult to estimate for two particles. It is strongly related to internal composition, surface roughness and surrounding gas. Elimelech et al. (1998) propose the following expression for the interaction potential between two perfect spheres:

$$V(u) = -\frac{A}{24}\left(\frac{1}{u+\frac{1}{2}u^2} + \frac{2}{(1+u)^2} + 4\ ln\frac{(2u+u^2)}{(1+u)^2}\right) \tag{2.93}$$

where A is the Hamaker constant, depending on the composition of the particle and the surrounding gas. A typical value is $A \sim 10^{-20}\ J$. D is the distance between the surfaces of the two particles and $u = D/d_p$ the ratio between D and d_p. The force associated with this potential is:

$$F_r(u) = -\frac{1}{6\,d_p}\,u^{-2}\,(2+u)^{-2}\,(1+u)^{-3} \tag{2.94}$$

For values of D smaller than the typical interatomic distance $z_0 \sim 4\ .\ 10^{-10}\ m$, repulsive forces dominate and Eqs. 2.93 and 2.94 are no longer valid. Then $F_r(u)$ is set to a constant value $F_r(u_0)$ for $0 < u < u_0 = z_0/d_p$. Hence the potential is given by:

$$V(u) = \frac{u}{u_0}\,V(u_0) \;\simeq -\frac{A}{24}\,\frac{u}{u_0^2} \quad \text{if} \quad 0 \le u \le u_0 \tag{2.95}$$

For $u \le 0$, the interaction between particles is treated as a collision.

For non-spherical particles the interaction potential can be as large as twice that of Eq. 2.93 (Xie, 1997). For the industrial fluidized beds considered, the relative uncertainty in the value of the Hamaker constant is much more than a factor of two. Therefore the assumption of spherical particles is not the limiting criterion and Eq. 2.93 will be considered as valid.

2.5.3 Implementation in the Eulerian two-fluid model

When particles do not aggregate, collisions can still be considered as instantaneous. Then, attractive forces can be introduced in the Boltzmann-Liouville equation using the BBGKY hierarchy (He and Doolen, 2002):

$$\begin{aligned}\frac{\partial f_p}{\partial t} + \frac{\partial}{\partial x_i}(c_{p,i} f_p) \;+\; & \frac{\partial}{\partial c_{p,i}}(< \frac{F_{p,i}}{m_p} \mid \mathbf{V_p} = \mathbf{c_p} > f_p) = \left(\frac{\partial f_p}{\partial t}\right)_{coll} \\ + \; & \iint \frac{\partial f_p^{(2)}}{\partial c_{p,i}} \frac{\partial}{\partial x_i}(\frac{V(\|\mathbf{x_2} - \mathbf{x}\|)}{m_p})\ \mathbf{dc_{p2}}\ \mathbf{dx_2}\end{aligned} \tag{2.96}$$

where $\mathbf{F_p}$ is the force acting on a particle and $f_p^{(2)}(\mathbf{c_p}, \mathbf{x}, \mathbf{c_{p2}}, \mathbf{x_2}, t)$ is the joint probability density function. Assuming that

$$f_p^{(2)} = g_r(\|\mathbf{x_2} - \mathbf{x}\|)\ f_p(\mathbf{c_p}, \mathbf{x}, t)\ f_p(\mathbf{c_{p2}}, \mathbf{x_2}, t) \tag{2.97}$$

where $g_r(\mathbf{x}, \mathbf{x_2})$ is the pairwise distribution function, Eq. 2.96 becomes:

$$\frac{\partial f_p}{\partial t} + \frac{\partial}{\partial x_i}(c_{p,i} f_p) + \frac{\partial}{\partial c_{p,i}}(\frac{F_{p,i}}{m_p} f_p) + \frac{\partial}{\partial c_{p,i}}(\frac{F_{a,i}}{m_p} f_p) + \frac{\partial}{\partial c_{p,i}}(\frac{F_{b,i}}{m_p} f_p) = \left(\frac{\partial f_p}{\partial t}\right)_{coll} \quad (2.98)$$

with $\mathbf{F_a}$ et $\mathbf{F_b}$ defined by:

$$F_{a,i} = -\frac{\partial}{\partial x_i} \int n_p(\mathbf{x_2})\ g_r(\|\mathbf{x_2} - \mathbf{x}\|)\ V(\|\mathbf{x_2} - \mathbf{x}\|)\ \mathbf{dx_2} \quad (2.99)$$

$$F_{b,i} = \int n_p(\mathbf{x_2})\ \frac{\partial g_r}{\partial x_i}(\|\mathbf{x_2} - \mathbf{x}\|)\ V(\|\mathbf{x_2} - \mathbf{x}\|)\ \mathbf{dx_2} \quad (2.100)$$

The momentum equation of the solid phase is obtained by multiplying Eq. 2.98 by $m_p \mathbf{c_p}$, then integrating over whole velocities $\mathbf{c_p}$. The result is similar to the one obtained by Balzer et al. (1995) except for the two last terms:

$$\begin{aligned} \alpha_p \rho_p \frac{DU_{p,i}}{Dt} = & - \frac{\partial}{\partial x_j}(\alpha_p \rho_p R_{p,ij} + \Theta_{ij}) \\ & - \alpha_p \frac{\partial P_g}{\partial x_i} - \frac{\alpha_p \rho_p}{\tau_p}\ (U_{p,i} - U_{g,i}) + \alpha_p \rho_p\ g_i \\ & - \alpha_p \frac{\partial P_a}{\partial x_i} + n_p F_{b,i} \end{aligned} \quad (2.101)$$

with P_a a negative pressure resulting from the attraction between particles:

$$P_a = \frac{6}{\pi\, d_p^3} \int n_p(\mathbf{x_2})\ g_r(\|\mathbf{x_2} - \mathbf{x}\|)\ V(\|\mathbf{x_2} - \mathbf{x}\|)\ \mathbf{dx_2} \quad (2.102)$$

The knowledge of n_p is required to integrate P_a and $\mathbf{F_b}$. However approximate expressions could be obtained.

2.5.4 Approximate expression

Exact calculation of P_a and $\mathbf{F_b}$ require the knowledge of n_p throughout the domain. However, the characteristic length scale of variation of V is very small compared to that of n_p. For particle of 70 μm diameter we have:

$$\frac{V(D = d_p/1000)}{V(D = z_0)} \simeq 0.6\ \% \quad (2.103)$$

For a distance a thousand times smaller than the particle diameter, the potential is smaller than 1 % of this contact value. Hence, assuming that g_r is nearly constant on this length

scale, P_a could be written as:

$$P_a = \frac{6g_0}{\pi d_p^3} \int_{\|\mathbf{x_2}-\mathbf{x}\|>d_p} n_p(\mathbf{x_2})\ V(\|\mathbf{x_2}-\mathbf{x}\|)\ \mathbf{dx_2} \tag{2.104}$$

with $g_0 = g_r(\|\mathbf{x_2}-\mathbf{x}\| = d_p)$ the pairwise distribution function at contact. This last one is traditionally assumed to be a function of α_p (Carnahan and Starling, 1969; Lun and Savage, 1986). Performing a zero-order expansion of n_p around $\mathbf{x}$ in Eq. 2.104 ($n_p(\mathbf{x_2}) \simeq n_p(\mathbf{x})$) leads to:

$$P_a = \frac{6\ n_p g_0}{\pi d_p^3} \int_{\|\mathbf{x_2}-\mathbf{x}\|>d_p} V(\|\mathbf{x_2}-\mathbf{x}\|)\ \mathbf{dx_2} \tag{2.105}$$

In the same way, $\mathbf{F_b}$ can be written as:

$$F_{b,i} \ \simeq\ n_p \int \frac{\partial g_r}{\partial x_i}(\|\mathbf{x_2}-\mathbf{x}\|)\ V(\|\mathbf{x_2}-\mathbf{x}\|)\ \mathbf{dx_2} \tag{2.106}$$

As $g_r(\|\mathbf{x_2}-\mathbf{x}\|)$ is an even function of $\mathbf{x_2}$, $\frac{\partial g_r}{\partial x_i}$ is an odd one. Moreover $V(\|\mathbf{x_2}-\mathbf{x}\|)$ is an even one. Consequently:

$$F_{b,i} \ = \ 0 \tag{2.107}$$

Using an adequate variable change, we obain for P_a:

$$P_a = 24\ A\ n_p g_0 \int_0^{+\infty} (1+u)^2\ V^*(u)\ du \tag{2.108}$$

were $V^* = V/A$ is the dimensionless potential. This integration can be decomposed into:

$$I \ = \ \int_0^{+\infty} (1+u)^2\ V^*(u)\ du = I_1 + I_2 \tag{2.109}$$

$$I_1 \ = \ \int_0^{u_0} (1+u)^2\ V^*(u)\ du \tag{2.110}$$

$$I_2 \ = \ \int_{u_0}^{+\infty} (1+u)^2\ V^*(u)\ du \tag{2.111}$$

A Taylor development for small values of u_0 leads to:

$$I_1 \ = \ -\frac{1}{48} + O(u_0) \tag{2.112}$$

$$I_2 \ = \ -\frac{1}{24}\ (ln\left(\frac{d_p}{z_0}\right) - \frac{4}{3} - \frac{5}{3}\ ln(2)) + O(u_0) \tag{2.113}$$

Putting Eqs. 2.112 and 2.113 into Eq. 2.108 leads to:

$$P_a \simeq -\frac{A}{m_p}\ \alpha_p\rho_p\ g_0\ ln\left(\frac{d_p}{z_0}\right) \tag{2.114}$$

Finally we obtain for the momentum equation of particulate phase:

$$\begin{aligned}\alpha_p\rho_p\frac{DU_{p,i}}{Dt} = &- \frac{\partial}{\partial x_j}(\alpha_p\rho_p R_{p,ij} + \Theta_{ij}) \\ &- \alpha_p\frac{\partial P_g}{\partial x_i} - \frac{\alpha_p\rho_p}{\tau_p}\ (U_{p,i} - U_{g,i}) + \alpha_p\rho_p\ g_i \\ &- \alpha_p\frac{\partial P_a}{\partial x_i}\end{aligned} \tag{2.115}$$

The isotropic part of the strain tensor $\Sigma_{p,ij} = \alpha_p\rho_p R_{p,ij} + \Theta_{ij}$ is the particle pressure P_p:

$$P_p = \frac{2}{3}\ \alpha_p\rho_p\ q_p^2\,(1 + 2(1+e_c)\alpha_p g_0) \tag{2.116}$$

in which the first part is the kinetic contribution and the second part the collisional contribution. The Van der Waals forces can be put into the particle pressure to give to the total pressure P_T:

$$P_T = \frac{2}{3}\ \alpha_p\rho_p\ q_p^2\,(1 + 2(1+e_c)\alpha_p g_0) - \alpha_p\rho_p\ \alpha_p g_0^b\ \frac{A}{m_p}\ \frac{1}{2}\ ln\left(\frac{d_p}{z_0}\right) \tag{2.117}$$

where g_0^b is defined by:

$$g_0^b = \frac{2}{\alpha_p^2}\ \int_0^{\alpha_p} \alpha_p f_0\ d\alpha_p \tag{2.118}$$

with $f_0 = (\alpha_p g_0)'$. Analytical integration of Eq. 2.118 can be performed when g_0 is given by the Carnahan and Starling (1969) expression. The exact expression is complicated but a Taylor development for small particle volume fraction leads to:

$$g_0^b = 1 + \frac{10}{3}\ \alpha_p + \frac{27}{4}\ \alpha_p^2 + \frac{56}{5}\ \alpha_p^3 + \frac{50}{3}\ \alpha_p^4 + O(\alpha_p^5) \tag{2.119}$$

The exact expression of g_0^b and the approximate form, Eq. 2.119, are compared in Figure 2.17. g_0 is also plotted as a reference.

Consequently, taking into account Van der Waals forces leads to the addition of a

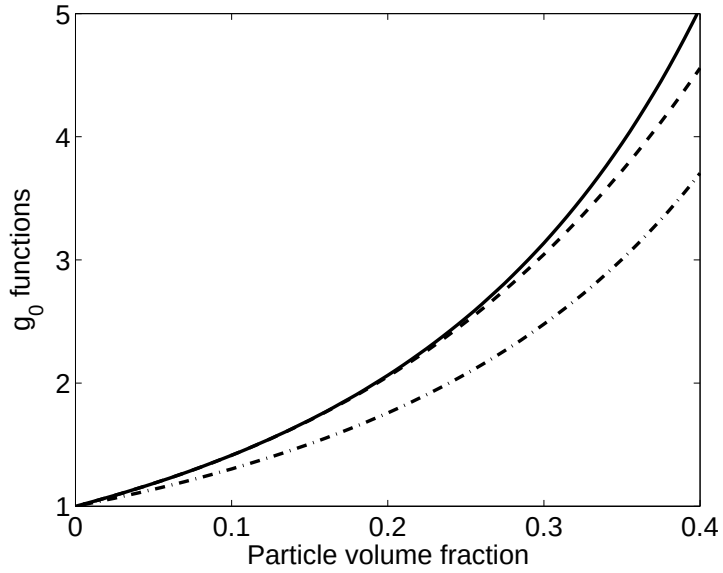

Figure 2.17: —— exact value of g_0^b, - - - approximate expression of g_0^b Eq. 2.119, -·-· g_0.

cohesive pressure P_c to the particle pressure, expressed as:

$$P_c = -\alpha_p \rho_p \; \alpha_p g_0^b \; \frac{A}{m_p} \; \frac{1}{2} \; ln\left(\frac{d_p}{z_0}\right) \tag{2.120}$$

The cohesive pressure is proportional to the Hamaker constant. The smaller the diameter is, the higher the intensity of the cohesive pressure becomes. The greater the particle volume fraction is, the higher this pressure becomes. When the particle volume fraction tends to the maximum compacting value, the cohesive pressure tends to infinity (when g_0^b is calculated with g_0 given by Lun and Savage (1986)).

2.5.5 Discussion

Eq. 2.117 shows that total particle pressure is decreases when inter-particle forces are present. This can lead to a an increase of the clustering effect because repulsion between particles is smaller. The influence of such forces can be evaluated by the P_p/P_c ratio. For a small particle volume fraction, the cohesive pressure is proportional to α_p^2 while particle pressure is proportional to $\alpha_p q_p^2$. As the particle agitation increases when particle the volume fraction decreases, cohesive pressure becomes negligible. For high particle volume

fraction, we obtain:

$$\frac{P_c}{P_p} \simeq \frac{3\ ln(d_p/z_0)}{8\ (1+e_c)}\ \frac{g_0^b}{g_0}\ \frac{A}{m_p q_p^2} \sim \frac{3}{16}\ ln(\frac{d_p}{z_0})\ \frac{A}{m_p q_p^2} \tag{2.121}$$

The Hamaker constant is between 10^{-22} and 10^{-20}. The particle agitation is evaluated using a numerical simulation with the standard two-fluid model of a fluidized bed of Geldart A particles, described in Chapter 3. The particle agitation is measured by:

$$q_{p,bed}^2 = \frac{<\alpha_p\ q_p^2>}{<\alpha_p>} \tag{2.122}$$

where <> is the average over the bed. Then this value is time-averaged:

$$<q_{p,bed}^2>_t \sim\ 7 \cdot 10^{-4}\ m^2/s^2 \tag{2.123}$$

For $A \sim 10^{-20}$ and $z_0 \sim 4 \cdot 10^{-10}$ we get:

$$\frac{P_c}{P_p} \sim\ 10^{-4} \tag{2.124}$$

Consequently, Van der Waals forces seem to have a negligible effect in our cases.

2.6 Conclusion

In this chapter, we successively suggested a way to modify the standard two-fluid model equations in order to take shear-induced collisions (Section 2.3), hydrodynamic effects (Section 2.4) and Van der Waals forces (Section 2.5) into account. None of these effects has appeared to be a good explanation of the great overestimation of the bed expansion found in numerical simulations. Hence, two-fluid models equations seem to be have a reasonable validity to predict flow inside fluidized bed of Geldart A particles. Therefore, the following chapters will focus on the way the two-fluid model equations are solved. In particular, the influence of the mesh size used to perform simulations is investigated.

Chapter 3

Filtered approach

3.1 Introduction

This chapter is devoted to the study of the way how two-fluid model equations are solved during numerical simulations. We particularly focus on the influence of the mesh size. As a starting point, a mesh-influence study is carried out for three fluidized beds with group B, A/B and A particles. The bed expansion is found to be sensitive to the mesh size in a drastic way for the fluidized bed with Geldart A particles, while it is only slightly sensitive for group A/B particles, and insensitive for group B particles. Then the problem is described in a dimensionless way and relevant dimensionless numbers are found. Three of them characterize the physical problem and the last one accounts for the mesh size. Hence the mesh sensitivity is shown to be a function of the dimensionless numbers and not an inherent property of the class of particles used. An empirical law giving the mesh size needed to ensure mesh-independent bed height is suggested. Application of this law highlights the fact that predicting correct bed expansion of a fluidized bed with Geldart A particles at laboratory or industrial scales is unaffordable due to computational limitations. Therefore, the resolved equations should be modified in order to correctly predict the bed expansion with coarse-grid simulations.

The filtered approach is used to provide such modifications. Numerical simulations are expected to provide spatially filtered quantities by solving the filtered two-fluid model but unknown terms such as the filtered drag force have to be closed. Highly resolved simulations are used to show that the overestimation of the filtered drag is linked to the existence of a subgrid drift velocity that should be taken into account.

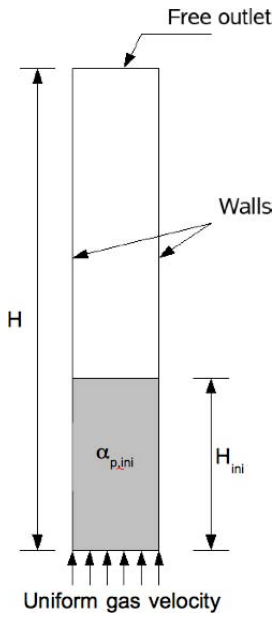

Figure 3.1: Geometry, initial and boundary conditions used in the 2D simulations of the bubbling fluidized beds.

3.2 Study of bubbling fluidized beds with group B, A/B and A particles

3.2.1 Cases description

2D simulations of freely bubbling beds of group A particles, group B particles and intermediate group A/B particles are carried out using NEPTUNE_CFD, an unstructured parallelized multiphase flow software. NEPTUNE_CFD is developed in the framework of the NEPTUNE project, financially supported by CEA (Commissariat à l'Énergie Atomique), EDF (Électricité de France), IRSN (Institut de Radioprotection et de Sureté Nucléaire) and AREVA- NP.

The geometry used for the three beds is identical and shown in Figure 3.1. The gas is uniformly injected at the bottom of the bed with a superficial velocity U_f. A free outlet is set at the top. Free-slip and no-slip are respectively set for the particle phase and gas phase for the wall boundary conditions. The bed is initially filled with particles at a solid volume fraction $\alpha_{p,ini}$ on a height H_{ini}. Particles, gas and geometrical properties are summarized in Table 3.1. They are extracted from experiments conducted by Makkawi et al. (2006) for group B and A/B particles. Conditions of typical FCC particles fluidized by ambient air are used for group A particles.

Particle type	**group A**	**group A/B**	**group B**
Bed width L (m)	0.03	0.138	0.138
Initial bed height H_{ini} (m)	0.10	0.20	0.20
Initial particle volume fraction $\alpha_{p,ini}$	0.55	0.58	0.58
Particle diameter d_p (μm)	75	125	350
Particle density ρ_p (kg/m^3)	1 500	2 500	2 500
Restitution coefficient e_c	0.95	0.80	0.80
Gas density ρ_g (kg/m^3)	1.186	1.4	1.4
Gas viscosity μ_g $(Pa.s)$	$1.8\ 10^{-5}$	$1.8\ 10^{-5}$	$1.8\ 10^{-5}$
Superficial gas velocity U_f (m/s)	0.2	0.26	0.54
Homogeneous bed height H_{eq} (m)	2.48	0.49	0.31

Table 3.1: Simulation parameters

3.2.2 Two-fluid model equations

Constitutive relations used were derived by Balzer et al. (1995) and are summarized in Appendix A. The model is based on separate transport equations of mass and momentum for the gas phase and mass, momentum and kinetic agitation for the particle phase. Equations are coupled through interphase momentum transfer terms. The particle kinetic stress is modelled using a viscosity assumption taking into account the friction of interstitial fluid.

The drag law is a key parameter in the simulation of a fluidized bed. Its contribution in the particle phase momentum equation can be written as:

$$I_{p,i} = \frac{\alpha_p \rho_p}{\tau_p} \left(U_{g,i} - U_{p,i}\right) \tag{3.1}$$

where τ_p is the mean particle relaxation time characterizing the particle inertia calculated with the Wen and Yu (1966) correlation:

$$\frac{1}{\tau_p} = \frac{1}{\tau_p^{St}} \left(1 + 0.15\, R_e^{0.687}\right) \alpha_g^{-2.7} \tag{3.2}$$

$R_e = \alpha_g \|\mathbf{U_g} - \mathbf{U_p}\| d_p/\nu_g$ is the particle Reynolds number and τ_p^{St} the Stokes drag time of an isolated particle, given by:

$$\tau_p^{St} = \frac{\rho_p}{\rho_g} \frac{d_p^2}{18\nu_g} \tag{3.3}$$

3.2.3 Mesh refinement results

The first step in performing a CFD simulation is to investigate the effect of mesh size on the simulation results. The mesh should be sufficiently fine so that further refinement will not change significantly the results. In such a case, model equations are correctly solved by the code and comparison with experimental data can be performed. Influence of mesh size on axial (vertical) and radial (horizontal) profiles of solids volume fraction and on averaged bed height is investigated. A square uniform grid is used with different mesh sizes. The cell width is noted Δ_G.

Figure 3.2 shows instantaneous particle volume fraction fields obtained by numerical simulations. The mesh size has a visible effect on the homogeneity and on the bed height. For all the groups of particles, refining the mesh leads to the formation of dense zones near maximum compacting fraction and dilute zones with a porosity close to one, as it can be seen on Figure 3.4 for the group A particles.

Time-averaged particle volume fraction profiles are shown in Figure 3.3. For group A/B and A particles, the bed height decreases as the mesh size reduces. In contrast, it remains unchanged for group B particles. The reduction is the most pronounced for group A particles and the bed height is reduced by more than a factor two between the coarsest mesh and the finest mesh. This reduction goes along with an increase of spatial inhomogeneity, as shown on Figure 3.4.

3.2.4 Experimental validation

Experimental validation is based on the time-averaged bed height and radial particle volume fraction profile for the simulations of Geldart A/B and Geldart B particles. Results are compared to experimental data given by Makkawi et al. (2006). Experiences of Makkawi et al. (2006) were conducted in a cylindrical bed. The authors report a bed height of $0.36 \pm 0.01\ m$ for both group B and A/B particles. These values are in good agreement with axial profiles shown in Figure 3.3 when the finest mesh is used.

3.3 Dimensionless approach

3.3.1 Introduction

The previous section has shown that a mesh sensitivity is found for the bed expansion when trying to simulate fluidized beds of Geldart A particles. Such mesh sensitivity is not found for Geldart B particles. This fact could be, in principle, expressed as a function of dimensionless numbers, but such numbers have not been identified yet. In this section, we

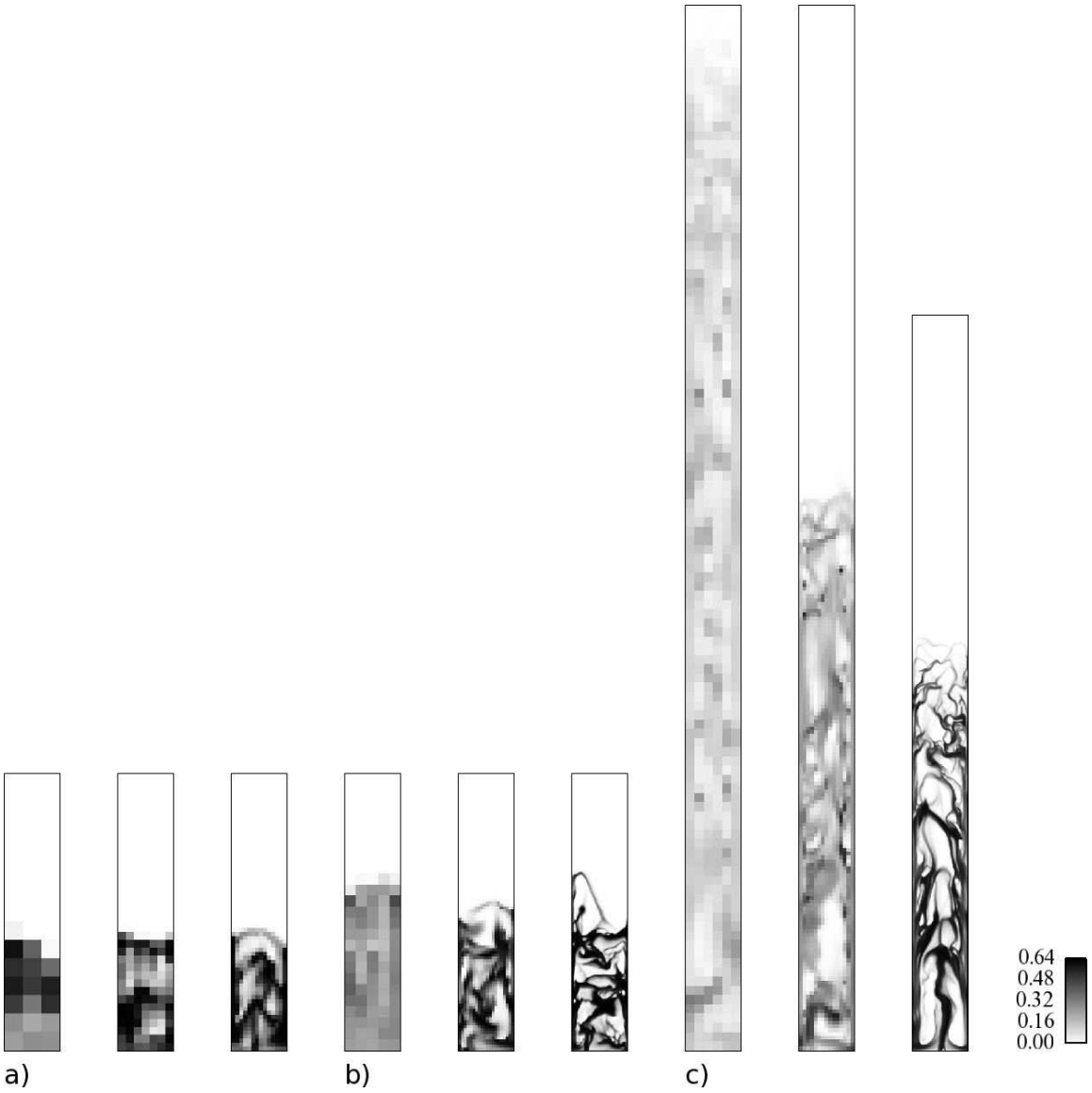

Figure 3.2: Snapshots of particle volume fraction. a) Geldart B particles. From left to right $\Delta_G = 4.60\ cm$, $1.97\ cm$ and $9.86\ mm$. b) Geldart A/B particles. From left to right $\Delta_G = 2.76\ cm$, $6.90\ mm$ and $1.73\ mm$. c) Geldart A particles. From left to right $\Delta_G = 5\ mm$, $2\ mm$ and $300\ \mu m$.

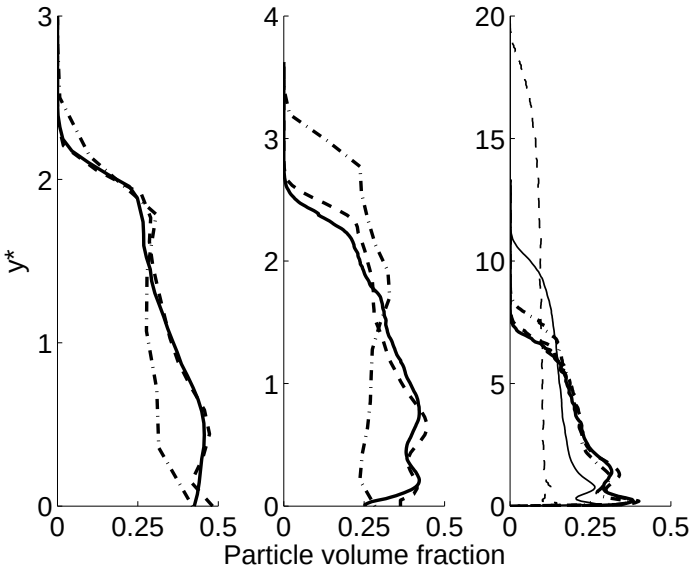

Figure 3.3: Vertical profiles of time-averaged particle volume fraction. From left to right: Geldart B particles (-·- : $\Delta_G = 4.60\ cm$, - - - : $\Delta_G = 1.97\ cm$, —— : $\Delta_G = 9.86\ mm$), Geldart A/B particles (-·- : $\Delta_G = 2.76\ cm$, - - - : $\Delta_G = 6.90\ mm$, —— : $\Delta_G = 1.73\ mm$) and Geldart A particles (- - - : $\Delta_G = 5\ mm$, —— : $\Delta_G = 2\ mm$, -·- : $\Delta_G = 1\ mm$, - - - : $\Delta_G = 500\ \mu m$, —— : $\Delta_G = 300\ \mu m$).

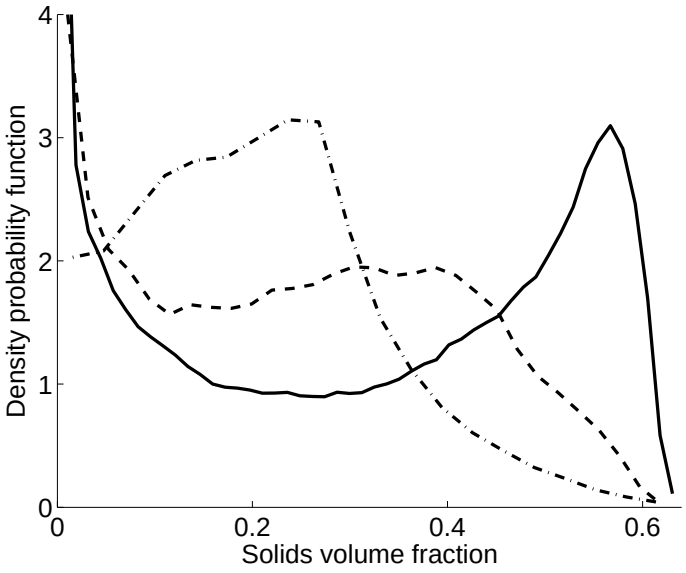

Figure 3.4: Probability density function of the particle volume fraction inside the fluidized bed of Geldart A particles. -·- : $\Delta_G = 2\ mm$, - - - : $\Delta_G = 1\ mm$, —— : $\Delta_G = 100\ \mu m$.

focus on the simple case of 2D fluidized beds, as described in the previous section. First, using a theoretical approach, all the dimensionless numbers describing this problem are found. Then some parameters are suppressed using physical considerations. Numerical simulations show the resulting simplified set to be relevant. Finally, an empirical law describing the mesh dependance is proposed.

3.3.2 Review of dimensionless numbers

Dimensionless numbers are used to find scaling relationships for fluidized beds from many years (Detamore et al., 2001; Glicksman, 1984; Glicksman et al., 1994; Horio et al., 2004). In particular, the three primary scaling sets that emerge from the literature include the full set (Chang and Louge, 1992; Glicksman et al., 1994), the simplified set (Glicksman et al., 1993; Horio et al., 1989) and the viscous-limit set (Glicksman, 1984; Horio et al., 2004):

Full set:

$$Fr = \frac{U_f}{gL} \quad , \quad Ar = \frac{(\rho_p - \rho_g)\,\rho_g\,d_p^3\,g}{\mu_g^2} \quad , \quad \frac{\rho_p}{\rho_g} \quad , \quad \frac{d_p}{L} \quad , \quad \frac{H_s}{L} \tag{3.4}$$

Simplified set:

$$Fr = \frac{U_f}{gL} \quad , \quad \frac{U_f}{U_{mf}} \quad , \quad \frac{\rho_p}{\rho_g} \quad , \quad \frac{H_s}{L} \tag{3.5}$$

Viscous-limit set:

$$Fr = \frac{U_f}{gL} \quad , \quad \frac{U_f}{U_{mf}} \quad , \quad \frac{H_s}{L} \tag{3.6}$$

The bed geometry is added to all sets. For circulating fluidized beds, the ratio $G_s/(\rho_p\,U_f)$ is substituted to the ratio H_s/L, where $H_s = \alpha_{p,ini}\,H_{ini}$ represents the total mass of particles inside the bed. As all sets are dedicated to experimental configurations, the particle sphericity and the particle size distribution is added. As in our numerical simulations particles are perfect spheres with only one diameter, these parameters are not significant. The terminal velocity is sometimes used instead of the minimum fluidization velocity U_{mf}. As noted by Detamore et al. (2001), collisional parameters should be added. In our cases, this leads to the addition of e_c to all sets.

All previous studies were devoted to find scaling relationship to build laboratory-scale experiments that reproduce the behaviour of large-scale process. Our interest is to find relevant dimensionless numbers that describe the influence of the mesh size on the bed expansion of a simulated fluidized bed.

3.3.3 Theoretical approach

The Vaschy-Buckingham theorem could be directly use to find a set of dimensionless numbers that characterize the problem. Here we chose to write the two-fluid model equations in a dimensionless form. This enable to highlight the physical meaning of the dimensionless numbers and to find the relevant combinations that are possibles.

Normalization parameters

L, U_f and ρ_p are chosen as characteristic length, velocity and density and used to make all variables dimensionless. The resulting characteristic time is L/U_f.

Geometrical description

The geometry used is shown in Figure 3.1. The dimensionless boundary conditions are expressed in Table 3.2 and lead to the first dimensionless number: H/L. This one is describing the geometrical aspect of the problem.

$x^* = 0$	wall
$x^* = 1$	wall
$y^* = 0$	$U^*_{g,x} = 0$, $U^*_{g,y} = 1$
$y^* = \frac{H}{L}$	free outlet

Table 3.2: Dimensionless boundary conditions

The initial condition is given by both $\alpha_{p,ini}$ and H_{ini}. As we are interested in the time-averaged quantities, only the total mass of particles inside the bed is significant. Hence the couple $(\alpha_{p,ini}, H_{ini})$ can be reduced to $H_s = \alpha_{p,ini} H_{ini}$. The corresponding dimensionless number is H_s/L.

Therefore, the initial and boundary conditions are described by to the two following dimensionless numbers:

$$\frac{H_s}{L} \quad , \quad \frac{H}{L} \tag{3.7}$$

The first one is for the initial condition, the second one for the bed geometry.

Dimensionless two-fluid model equations

The two-fluid model equations can be described in a dimensionless form. The mass transport equation for the k phase becomes:

$$\frac{\partial \alpha_k}{\partial t^*} + \frac{\partial}{\partial x_i^*}(\alpha_k \, U_{k,i}^*) = 0 \tag{3.8}$$

The mass transport equation do not lead to more dimensionless numbers. The momentum transport equation for the k phase is:

$$\alpha_k \, \rho_k^* \, \frac{DU_{k,i}^*}{Dt} = -\alpha_k \, \frac{\partial P_g^*}{\partial x_i^*} - \frac{gL}{U_f^2} \, \alpha_k \rho_k^* \, \delta_{i,3} + \frac{L}{\tau_p^0 \, U f} \, I_{k,i}^* + \frac{\partial}{\partial x_j^*} \Sigma_{p,ij}^* \tag{3.9}$$

where $\rho_p^* = 1$, $\rho_g^* = \rho_g/\rho_p$ and $I_{p,i}^*$ is the the drag contribution given by:

$$I_{p,i}^* = -I_{g,i}^* = \frac{\alpha_p \, V_{r,i}^*}{\tau_p^*} \tag{3.10}$$

$$\frac{1}{\tau_p^*} = \alpha_g^{-2.7} \; f(Re_f, \alpha_g \| V_{r,i}^* \|) \tag{3.11}$$

$$f(Re_f, \alpha_g \| V_{r,i}^* \|) = \frac{1 + 0.15 \, Re_f^{0.687} (\alpha_g \| V_{r,i}^* \|)^{0.687}}{1 + 0.15 \, Re_f^{0.687}} \tag{3.12}$$

$$Re_f = \frac{U_f d_p}{\nu_g} \tag{3.13}$$

Re_f is a particle Reynolds number constructed with the superficial gas velocity. The gravity contribution is expressed in function of the Froude number $U_f^2/(gL)$. The drag contribution is function of the particle Reynolds number Re_f and a Stokes number $\tau_p^0 U f/L$. The dimensionless stress tensor $\Sigma_{p,ij}^*$ is function of the ratio d_p/L and the restitution coefficient e_c. As the particle Reynolds number can be expressed in function of ρ_p/ρ_g, d_p/L et $\tau_p^0 U_f/L$, we get 5 independent dimensionless numbers:

$$\frac{\rho_p}{\rho_g} \quad , \quad \frac{d_p}{L} \quad , \quad \frac{U_f}{\tau_p^0 \, g} \quad , \quad \frac{\tau_p^0 \, U_f}{L} \quad , \quad e_c \tag{3.14}$$

The Froude number was divided by the Stokes number $\tau_p^0 U f/L$ in order to make the ratio between the superficial gas velocity and $\tau_p^0 \, g$ appear. When this ratio is greater than one, the bed becomes circulating. This ratio is the equivalent of the ratio U_f/U_{mf}.

Moreover, a transport equation for the kinetic particle agitation is solved. This equation

does not show new independent dimensionless parameters, as it can be proved by the Vaschy-Buckingham theorem.

Numerical resolution

A lot of parameters appears in the numerical resolutions of the two-fluid model equations. The two main parameters are the scheme order used and the mesh. Here we restrict our attention to uniform square mesh. The scheme used is of second order in space and first order in time and will not be changed. Hence Δ_G is chosen as the unique parameter describing all the numerical setup. The corresponding dimensionless number is:

$$\frac{\Delta_G}{L} \tag{3.15}$$

Simplified set

Boundary and initial conditions, two-fluid model equations and numerical set-up lead to a set of 8 dimensionless parameters (Eqs. 3.7, 3.14 and 3.15). This set could be reduced.

We assume that the ratio ρ_p/ρ_g and L/d_p have a negligible impact. The ratio L/d_p appears in collisional terms and such terms do not have a major impact on the bed expansion. In the same way, the restitution coefficient has not a significant influence on the bed expansion of bubbling fluidized beds when its value remains close to the unity ($1 - e_c \ll e_c < 1$). Therefore it is also removed from the set.

The height of the domain, H, has not a great influence in bubbling fluidized bed as their is no circulating solids. Its value is assumed to be greater than the bed expansion in order to keep all the particles inside the bed. Its contribution will also not appear in the simplified set.

Finally, a simplified set of four dimensionless numbers is found:

$$\frac{H_s}{L} \quad , \quad \frac{U_f}{\tau_p^0\, g} \quad , \quad \frac{\tau_p^0\, U_f}{L} \quad , \quad \frac{\Delta_G}{L} \tag{3.16}$$

A modified viscous-limit set Eq. 3.6 is found, where the ratio Δ_G/L is added, the Stokes number $\tau_p^0 L/U_f$ is substituted to the Froude number and the ratio $U_f/(\tau_p^0\, g)$ is substituted to the ratio U_f/U_{mf}.

3.3.4 Mesh dependence equivalence

The simplified set Eq. 3.16 is used to show that the mesh dependence on the bed expansion found for the fluidized bed with group A particles can also be found when using group

A/B and group B particles. Numerical simulations of new fluidized beds are performed. The particles are the same that were used in Section 3.2 and are fluidized by ambient air. The bed width, the superficial gas velocity, the initial bed height and the mesh size are calculated using the simplified set Eq. 3.16. The restitution coefficient is fixed to 0.95 for the three type of particles. The parameters are summarized in Table 3.3. Value of the dimensionless numbers are reported showing that only the simplified set and the elasticity coefficient are conserved between the three fluidized beds. The superficial gas velocity is 10 times greater for the group B particles than for the group A particles and the bed width is 100 times greater.

Particle type	**group A**	**group A/B**	**group B**
Bed width L (m)	0.03	0.3753	4.512
Initial bed height H_{ini} (m)	0.10	1.251	15.04
Initial particle volume fraction $\alpha_{p,ini}$	0.55	0.55	0.55
Particle diameter d_p (μm)	75	125	350
Particle density ρ_p (kg/m^3)	1 500	2 500	2 500
Restitution coefficient e_c	0.95	0.95	0.95
Gas density ρ_g (kg/m^3)	1.186	1.186	1.186
Gas viscosity μ_g $(Pa.s)$	1.8 10^{-5}	1.8 10^{-5}	1.8 10^{-5}
Superficial gas velocity U_f (m/s)	0.2	0.708	2.454
Mesh size Δ_G (mm)	$5, 2, 1, 0.5$	$62.6, 25, 12.5, 6.26$	$752, 302, 150, 75.2$
H_s/L	1.83	1.83	1.83
$U_f/(\tau_p^0\, g)$	0.90	0.90	0.90
$\tau_p^0\, U_f/L$	0.15	0.15	0.15
L/Δ_G	$6, 15, 30, 60$	$6, 15, 30, 60$	$6, 15, 30, 60$
ρ_p/ρ_g	1265	2108	2108
L/d_p	400	3000	12890
Re_f	0.98	5.83	57
Archimedes number	23	175	3850

Table 3.3: Simulation parameters and dimensionless numbers of the new fluidized beds

Time-averaged particle volume fraction profiles are shown in Figure 3.5. The same dependence of the bed height to the mesh size is found for the three beds. However the similitude between the profiles is not perfect. Nevertheless, it shows that the the mesh dependence of the bed expansion can be reasonably expressed as a function of the dimensionless numbers of the simplified set. Moreover, it shows that the mesh dependance of the bed expansion can also be found in large-scale bubbling fluidized bed with Geldart B particles, as observed by Wang et al. (2010). Converged results also show that the 4.5 m-width fluidized bed of Geldart B particles is nearly equivalent to the 3 cm-width fluidized bed of

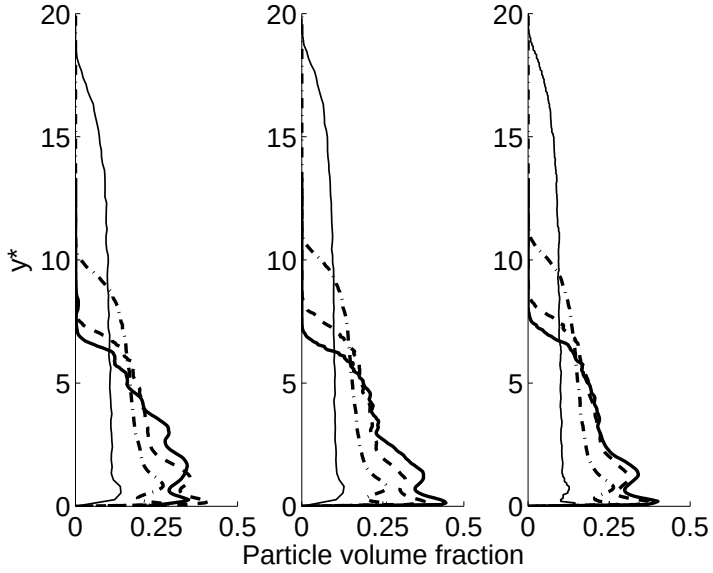

Figure 3.5: Vertical profiles of time-averaged particle volume fraction. From left to right: Geldart B particles, Geldart A/B particles and Geldart A particles. —— : $L/\Delta_G = 6$, -·-·- : $L/\Delta_G = 15$, - - - : $L/\Delta_G = 30$, —— : $L/\Delta_G = 60$.

Geldart A particles.

3.3.5 Mesh dependence law

The mesh dependence has been shown to be a function of the dimensionless numbers appearing in the simplified set Eq. 3.16. In the case of a very coarse grid, the field of particle volume fraction is nearly homogeneous and the corresponding bed height is of the order of H_{eq}, the height found by assuming an homogeneous equilibrium in the momentum transport equations of particle and gas phase, Eqs. 3.9 or A.3:

$$H_{eq} = \frac{H_s}{1 - \alpha_g^{eq}} \tag{3.17}$$

where α_g^{eq} is given by:

$$\alpha_g^{eq} = \left(\frac{U_f}{\tau_p^0 \, g} \, \frac{\rho_p}{\rho_p - \rho_g} \right)^{\frac{1}{4.7}} \tag{3.18}$$

As the mesh size increases, the particle volume fraction tends to $\alpha_p^{eq} = 1 - \alpha_g^{eq}$. Noting α_p^{cv} the mean particle volume fraction over the bed when convergence is achieved, the particle

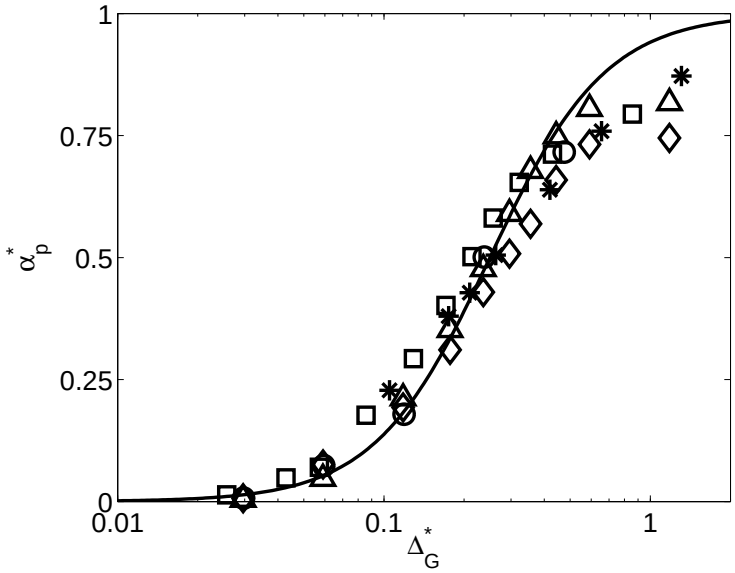

Figure 3.6: α_p^* in function of Δ_G^*. —— : Eq. 3.21. Symbols are simulation results described in Table 3.4.

volume fraction α_p given at a particular mesh size can be scaled in the following form:

$$\alpha_p^* = \frac{\alpha_p - \alpha_p^{cv}}{\alpha_p^{eq} - \alpha_p^{cv}} \tag{3.19}$$

Figure 3.6 shows the evolution of α_p^* in function of a dimensionless mesh size Δ_G^* given by:

$$\Delta_G^* = \frac{\Delta_G}{L} \left(\frac{L}{\tau_p^0 \, U_f} \right)^{\frac{1}{2}} \tag{3.20}$$

Various numerical simulations of the Geldart A fluidized bed were performed, with some parameters that have been changed (see Table 3.4). The results are put in Figure 3.6. It should be noted that the dimensionless parameter Δ_G^* depends both on the particle relaxation time τ_p^0 and on bed width L.

A fit on numerical results leads to the following law giving the evolution of α_p^* as a function of Δ_G^* :

$$\alpha_p^* = \frac{{\Delta_G^*}^2}{{\Delta_c^*}^2 + {\Delta_G^*}^2} \tag{3.21}$$

where $\Delta_c^* \simeq 0.25$. The law given by Eq. 3.21 allows to estimate the mesh size needed to obtain a relative error e between the height given by the numerical simulation with the

Case	*Symbol*
Ref.	$\square$
$U_f = 0.1\ m/s$	$\triangle$
$U_f = 0.1\ m/s$, $H_{ini} = 3\ cm$	$\Diamond$
$L = 0.5\ m$, $H_{ini} = 0.5\ cm$	$*$
A/B particles (see Table 3.1)	$\circ$

Table 3.4: Parameters and corresponding symbols of the simulations of Geldart A fluidized beds. Ref. is the case describe in Table 3.1. Other cases differ only for parameters that are indicated.

mesh size Δ_G and the converged result:

$$H = H_{cv}\,(1+e) \tag{3.22}$$

The scaled particle volume fraction α_p^* is given by:

$$\alpha_p^* = \frac{e}{1+e}\,\frac{1}{1-r} \simeq \frac{e}{1-r} \tag{3.23}$$

where $r = H_{cv}/H_{eq}$ is the ratio between the converged bed height and the homogeneous bed height. This ratio decreases as the superficial gas velocity approaches the terminal velocity. Then, using Eq. 3.21 and assuming that $e \ll 1$, the mesh size Δ_G^* needed to obtain the relative error e is given by:

$$\Delta_G^* = \Delta_c^* \left(\frac{e}{1-r}\right)^{\frac{1}{2}} \tag{3.24}$$

Finally, the number of cells in the width of the bed L/Δ_G is given by:

$$\frac{L}{\Delta_G} \;\simeq\; 4.0 \left(\frac{1-r}{e}\right)^{\frac{1}{2}} \left(\frac{L}{\tau_p^0\, U_f}\right)^{\frac{1}{2}} \tag{3.25}$$

When r goes to one. *i.e* that the converged bed height is the homogeneous bed height, the number of cells needed goes to zero because the a coarse-grid simulation will lead to a homogeneous expansion of the bed. The number of cells needed depends both on the particle relaxation time τ_p^0 and on bed width L. Smaller particles have a smaller relaxation time τ_p^0. Hence the number of cells needed is greater.

3.4 Filtered Two-Fluid Model Equations

The study carried out in Section 3.2 has shown that small structures are predicted by the two-fluid model equations and that these structures have a drastic influence on the bed expansion. Due to practical limitations, these structures cannot be resolved for simulations at the pilot or industrial scale. Hence, they need to be modelled. The filtering approach is a formalism that highlights terms that need to be closed when we do not wish to solve small structures. This idea has been applied in single-phase turbulent flow for many years (Smagorinsky, 1963) but the application to gas-particle flows is very recent (Agrawal et al., 2001; Andrews IV et al., 2005; Igci et al., 2008; Zhang and VanderHeyden, 2002).

The idea is to split all physical variables into a resolved part and an unresolved part. The resolved part of a variable is the spatially-filtered variable, which contains only large-scale structures that can be resolved on a coarse-grid. The unresolved part contains the small scales that cannot be solved on a coarse grid. The balance laws of the filtered variables are found by filtering the balance laws of the two-fluid model. While we have chosen a particular set of constitutive relations for the two-fluid model, the approach can be applied to other relations.

Let us define $\overline{f}(\mathbf{x},t)$ as the filtered part - or the resolved part - of a space-time variable $f(\mathbf{x},t)$ as:

$$\overline{f}(\mathbf{x},t) = \iiint G(\mathbf{x}-\mathbf{u})\ f(\mathbf{u},t)\ \mathbf{du} \tag{3.26}$$

where G is a weight function that satisfies $\iiint G(\mathbf{u})\ \mathbf{du} = 1$. Several choices can be made for the weight function. By choosing how rapidly $G(\mathbf{u})$ decays when u increases, one can change how much the small structures will be taken into account in the resolved part. Hence, the filtered particle volume fraction $\overline{\alpha}_p$ is defined according to Eq. 3.26:

$$\overline{\alpha}_p(\mathbf{x},t) = \iiint G(\mathbf{x}-\mathbf{u})\ \alpha_p(\mathbf{u},t)\ \mathbf{du} \tag{3.27}$$

The gas phase pressure $\overline{P}_g(\mathbf{x},t)$ is similarly defined. Filtered phase velocities are defined by:

$$\widetilde{U}_{p,i} = \overline{\alpha_p U_{p,i}}\ /\ \overline{\alpha}_p \tag{3.28}$$

$$\widetilde{U}_{g,i} = \overline{\alpha_g U_{g,i}}\ /\ \overline{\alpha}_g \tag{3.29}$$

The filtered particle agitation is defined by $\widetilde{q}_p^2 = \overline{\alpha_p\, q_p^2}\ /\ \overline{\alpha}_p$.

The balance laws for the filtered variables are obtained by filtering the balance laws of

the two-fluid model, leading, for the mass transport equations, to:

$$\frac{\partial}{\partial t}(\rho_k\,\overline{\alpha}_k) + \frac{\partial}{\partial x_j}(\rho_k\,\overline{\alpha}_k\widetilde{U}_{k,j}) = 0 \tag{3.30}$$

where the subscript $k = p$ for the particle phase and $k = g$ for the gas phase. A direct consequence of the definition of the filtered phase velocities Eqs. 3.28 and 3.29 is that Eqs. 3.30 are formally similar to those of the two-fluid model. Filtering the momentum transport equation of the particle phase leads to:

$$\begin{aligned}
\rho_p\,\overline{\alpha}_p\,\frac{D\widetilde{U}_{p,i}}{Dt} &= \rho_p\,\overline{\alpha}_p\,g_i \\
&- \overline{\alpha}_p\,\frac{\partial\overline{P}_g}{\partial x_i} - \Phi_{P,i} \\
&+ \rho_p\,\frac{\overline{\alpha}_p\widetilde{W}_{r,i}}{\widetilde{\tau}_p} + \Phi_{D,i} \\
&- \frac{\partial}{\partial x_j}\overline{\Sigma}_{p,ij} - \frac{\partial}{\partial x_j}(\rho_p\,\overline{\alpha}_p\sigma_{p,ij})
\end{aligned} \tag{3.31}$$

where $\widetilde{W}_{r,i} = \widetilde{U}_{g,i} - \widetilde{U}_{p,i}$ is the resolved relative velocity. The particle relaxation time τ_p is given by the Wen and Yu (1966) drag law (Eq. A.15) and $\widetilde{\tau}_p$ is defined similarly using the resolved part of the variables:

$$\frac{1}{\widetilde{\tau}_p} = \frac{1}{\tau_p^{St}}\left(1 + 0.15\,\widetilde{Re}^{0.687}\right)\overline{\alpha}_g{}^{-2.7} \tag{3.32}$$

$\widetilde{Re} = \overline{\alpha}_g\|\widetilde{\mathbf{U}}_\mathbf{g} - \widetilde{\mathbf{U}}_\mathbf{p}\|d_p/\nu_g$ and $\tau_p^{St} = \rho_p d_p^2/(18\mu_g)$ the Stokes drag time of an isolated particle. Four terms have to be closed: the filtered particle stress, $\overline{\Sigma}_{p,ij}$, a Reynolds stress-like contribution coming from the particle phase velocity fluctuations, $\sigma_{p,ij}$ defined by:

$$\overline{\alpha}_p\sigma_{p,ij} = \overline{\alpha_p U_{p,i}U_{p,j}} - \overline{\alpha}_p\widetilde{U}_{p,i}\widetilde{U}_{p,j} \tag{3.33}$$

and $\Phi_{P,i}$ and $\Phi_{D,i}$, defined by:

$$\Phi_{P,i} = \overline{\alpha_p\frac{\partial P_g}{\partial x_i}} - \overline{\alpha}_p\frac{\partial\overline{P}_g}{\partial x_i} \tag{3.34}$$

$$\Phi_{D,i} = \rho_p\,\overline{\left(\frac{\alpha_p V_{r,i}}{\tau_p}\right)} - \rho_p\,\frac{\overline{\alpha}_p\widetilde{W}_{r,i}}{\widetilde{\tau}_p} \tag{3.35}$$

where $V_{r,i} = U_{g,i} - U_{p,i}$ is the relative velocity. The balance law for the filtered gas velocity

can be obtained by filtering the gas phase momentum equation, leading to another unknown term, $\sigma_{g,ij}$, defined by:

$$\overline{\alpha}_g \sigma_{g,ij} = \overline{\alpha_g U_{g,i} U_{g,j}} - \overline{\alpha}_g \widetilde{U}_{g,i} \widetilde{U}_{g,j} \tag{3.36}$$

In the following, the balance law of the filtered particle agitation is assumed to be similar to Eq. A.11 when using the filtered variables. This amounts to say that unresolved terms appearing in this equation are assumed to have a negligible effect on the bed expansion.

3.5 A priori analysis description

As the mesh convergence is reached with the 100 μm-mesh size for simulation with the Geldart A particles (see Section 3.2.3), the simulation is said to be fully resolved. Results are assumed to be a good discretization of the continuous solution of the two-fluid model. The mesh size will be noted Δ_D in the following, in reference to single-phase flow simulations, where such grid-size independent results are called "Direct Numerical Simulation". Hence we get $\Delta_D = 100\ \mu m$. These results are used to provide closures for the unknown terms appearing in Eq. 3.31. For each snapshot of the flow field, the filtered quantities are calculated at each cell of the mesh, using for G a discrete version of the continuous box filter:

$$G(\mathbf{u}) = \begin{cases} 1/\Delta_B^2 & \text{if } \ max(u_x, u_z) < \Delta_B/2 \\ \\ 0 & \text{otherwise} \end{cases} \tag{3.37}$$

Hence the instantaneous field of the filtered particle volume fraction, the filtered velocities, and so forth, are known for any value of Δ_B. The operation is repeated for many snapshots, leading to a wide number of values for each filtered quantity. Typically, we use 10 snapshots. As the mesh is composed of 900 000 cells, we get 9 000 000 of values for each filtered quantity and each value of Δ_B. All these filtered values are considered as statistically equivalent and are used to perform various averaging operations.

3.6 Subgrid drift velocity

3.6.1 Budget analysis

The database described in Section 3.5 is used to quantify the contribution of each term appearing in the filtered momentum equation of the particle phase, Eq.3.31. Let us define $< \overline{f} >_{b,t}$ as the average of $\overline{f}$ over space and time. Applying the $< . >_{b,t}$ operation to Eq.3.31

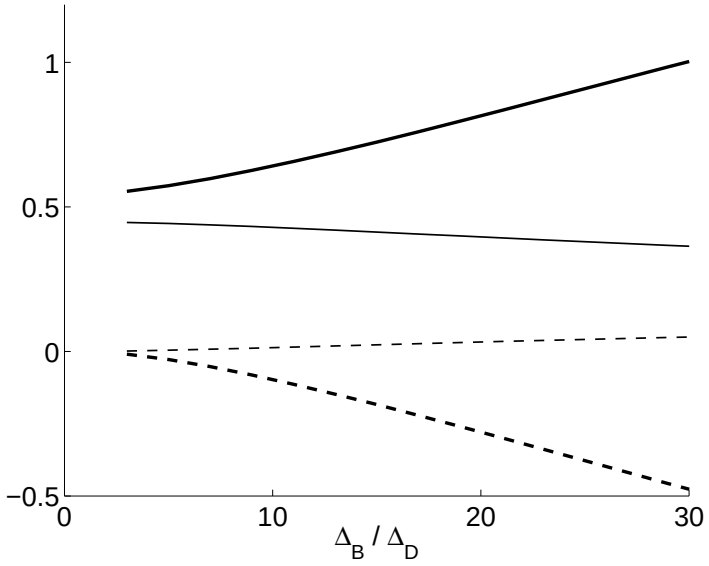

Figure 3.7: Budget analysis of Eq. 3.38 *vs.* the ratio Δ_B/Δ_D. ——— : resolved drag force, - - - : unresolved drag force, —— : resolved buoyancy, – – – : unresolved buoyancy. All values are divided by the absolute value of the gravity contribution.

leads to:

$$\begin{aligned} 0 &= < \rho_p \, \overline{\alpha}_p g_i >_{b,t} \\ &+ < \overline{\alpha}_p \frac{\partial \overline{P}_g}{\partial x_i} >_{b,t} - < \Phi_{P,i} >_{b,t} \\ &+ < \rho_p \frac{\overline{\alpha}_p \widetilde{W}_{r,i}}{\widetilde{\tau}_p} >_{b,t} + < \Phi_{D,i} >_{b,t} \end{aligned} \tag{3.38}$$

Eq. 3.38 simply states the global equilibrium between the filtered drag force, the filtered gravity and the filtered gas pressure gradient. The first term in the r.h.s. of Eq. 3.38 is the contribution of gravity. The second and the third are respectively the resolved and unresolved part of the buoyancy. The two last terms are the resolved and unresolved part of the drag force. The vertical components of these terms are plotted versus the Δ_B/Δ_D ratio in Figure 3.7. It is clear that, as the filter size increases, the resolved part of the drag force increases dramatically. In consequence, the unresolved part of the drag $\Phi_{D,i}$ decreases so that the average of the filtered drag remains constant. For this reason, when the filtered drag is estimated by its resolved part only - i.e. when $\Phi_{D,i}$ is neglected - the bed expansion is consequently overestimated. In contrast, the unresolved part of the buoyancy

$\Phi_{P,i}$ remains negligible.

This analysis shows that the first-order term that needs to be modelled to predict the correct bed expansion of a bubbling fluidized bed is the unresolved part of the drag. Hence we will focus on this term in the following. In circulating fluidized beds, some authors report that the contribution of the unresolved part of the buoyancy $\Phi_{P,i}$ is not negligible (De Wilde, 2005, 2007; Zhang and VanderHeyden, 2002). Effect of the Reynolds stress-like contribution $\sigma_{p,ij}$ and the filtered particle-stress $\overline{\Sigma}_{p,ij}$ were studied by Agrawal et al. (2001) and Igci et al. (2008) but are not the topic of this study.

3.6.2 Drift velocity

In order to predict the correct fluidized bed expansion, we need to model the filtered drag force. Various authors have proposed a closure law in the form of an effective drag coefficient (Andrews IV et al., 2005; Heynderickx et al., 2004; Igci et al., 2008; Wang and Li, 2007) defined by:

$$\overline{\left(\frac{\alpha_p \rho_p}{\tau_p} V_{r,i}\right)} = \beta_e \widetilde{W}_{r,i} \tag{3.39}$$

This effective drag coefficient depends either on the filtered particle volume fraction (Heynderickx et al., 2004; Andrews IV et al., 2005) or on the filter size (Igci et al., 2008). Here, we propose to model the filtered drag force using an effective relative velocity instead of an effective drag coefficient. This effective relative velocity is the sum of the resolved relative velocity $\widetilde{W}_{r,i}$ and a subgrid drift velocity $\widetilde{V}_{d,i}$ defined by:

$$\overline{\left(\frac{\alpha_p \rho_p}{\tau_p} V_{r,i}\right)} = \frac{\overline{\alpha}_p \rho_p}{\widetilde{\tau}_p} \left(\widetilde{W}_{r,i} + \widetilde{V}_{d,i}\right) \tag{3.40}$$

A correlative analysis using our database has shown that the filtered drag force can be approximated by:

$$\overline{\frac{\alpha_p \rho_p}{\tau_p} V_{r,i}} \simeq \frac{\rho_p}{\widetilde{\tau}_p} \overline{\alpha_p V_{r,i}} \tag{3.41}$$

The r.h.s of Eq. 3.41 is correlated with the l.h.s to more than 99 %, even for high values of Δ_B. It should be noted that the particle relaxation time depends both on the gas volume fraction and on the Reynolds number, which also depends on the relative velocity and on the gas volume fraction (Eq. 3.32). Eq. 3.41 is an approximation and shows that the major challenge in predicting the filtered drag force is to produce a good model for the filtered relative velocity weighted by the particle volume fraction, $\overline{\alpha_p V_{r,i}}$. This last one can be decomposed as follow:

$$\overline{\alpha_p V_{r,i}} = \overline{\alpha}_p \widetilde{W}_{r,i} + \overline{\alpha}_p \left(\widetilde{U}_{g@p,i} - \widetilde{U}_{g,i}\right) \tag{3.42}$$

where:

$$\widetilde{U}_{g@p,i} \;=\; \overline{\alpha_p U_{g,i}} \;/\; \overline{\alpha}_p \tag{3.43}$$

is the filtered gas velocity seen by the particle phase. Putting Eq. 3.42 in Eq. 3.41 leads, for the subgrid drift velocity, to:

$$\widetilde{V}_{d,i} \;\simeq\; \widetilde{U}_{g@p,i} - \widetilde{U}_{g,i} \tag{3.44}$$

Figure 3.8 compares an instantaneous horizontal profile of the vertical drift velocity as defined by Eq. 7.5 and by using the relation Eq. 7.6. A very good agreement between the exact value and its approximated form is found. Hence, the drift velocity $\widetilde{V}_{d,i}$ can be interpreted as the difference between the filtered gas velocity seen by the particle phase and the filtered gas velocity seen by the gas phase (defined Eq. 3.29).

$\widetilde{V}_{d,i}$ is a subgrid drift velocity coming from the correlation between the particle volume fraction and the gas velocity as well as from spatial inhomogeneities inside the volume of filtering. The joint probability density function of the particle volume fraction and the gas velocity is shown in Figure 3.9. There is a strong dependence of the gas velocity on the particle volume fraction. As seen on Figure 3.10, the gas velocity is, on average, greater in dilute regions than in dense regions. Consequently the gas velocity seen by the gas phase will be greater, on average, than the gas velocity seen by the particle phase. Hence, the average drift velocity will be negative, reflecting the fact that the resolved part of the relative velocity overestimates the efficient relative velocity.

A Taylor development shows that, for small filter size, the drift velocity can be written as (see Apendix D):

$$\overline{\alpha}_p \; \overline{\alpha}_g \; \widetilde{V}_{d,i} = \; \frac{\overline{\Delta}^2}{12} \; \frac{\partial \alpha_p}{\partial x_j} \; \frac{\partial U_{g,i}}{\partial x_j} \; + \; O(\overline{\Delta}^4) \tag{3.45}$$

with $\overline{\Delta}$ a characteristic length scale of the filter (for instance, when G is the continuous box filter, $\overline{\Delta} = \Delta_B$). Eq. 3.45 shows that the drift velocity is proportional to the square of the filter size when the latter is small. Therefore, a model for the filtered drag should respect this square dependence for small filter size in order to be mathematically consistent.

3.7 Conclusion

The mesh-influence study has shown that coarse-grid simulations of bubbling fluidized beds with Geldart A particles severely overestimate the bed expansion. This mesh sensitivity has been shown to be dependant of dimensionless numbers, such as the ratio between the superficial gas velocity and the terminal velocity, and a Stokes number build with the bed

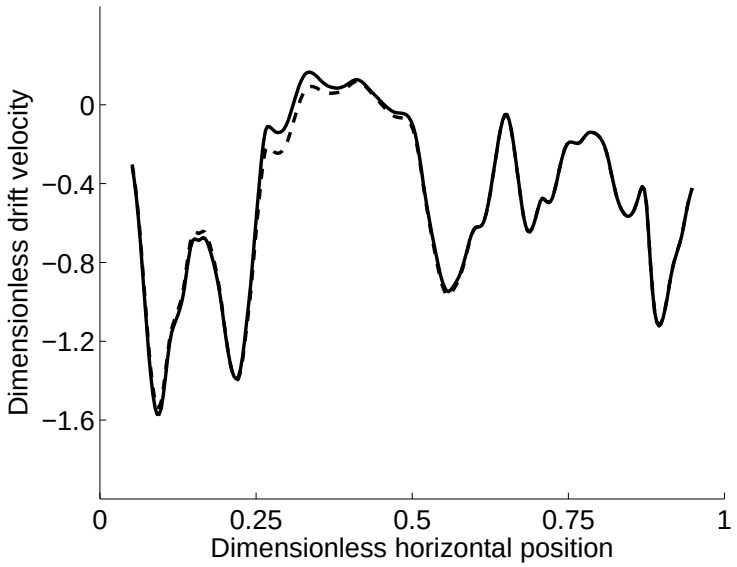

Figure 3.8: Profile of instantaneous dimensionless drift velocity versus of dimensionless horizontal position in the bed. Box filter was used with $\Delta_B = 31\ \Delta_D$. Vertical position in the bed is 0.15 m. Horizontal position is adimensionalized using bed width. Drift velocities were made dimensionless using the superficial gas velocity. ——— : exact drift velocity, Eq. 7.5, - - - approximate drift velocity, Eq.7.6.

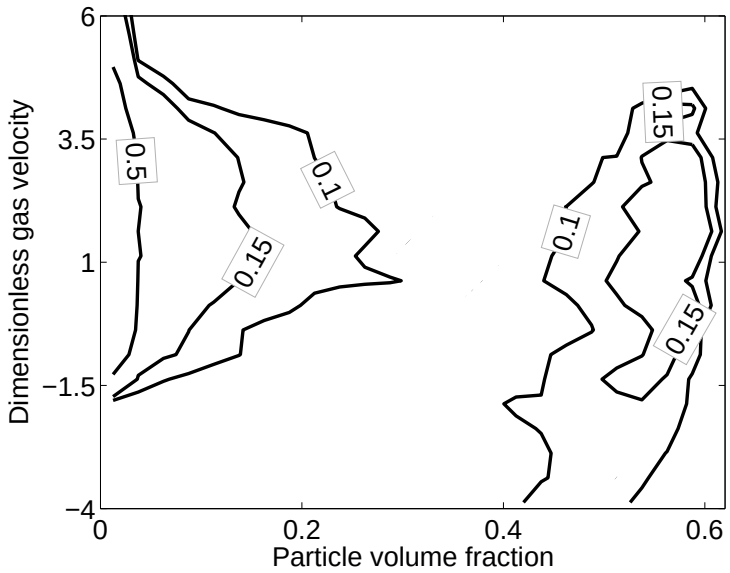

Figure 3.9: Iso values of the joint probability density function between the particle volume fraction and the gas velocity. The gas velocity is made dimensionless using the superficial gas velocity.

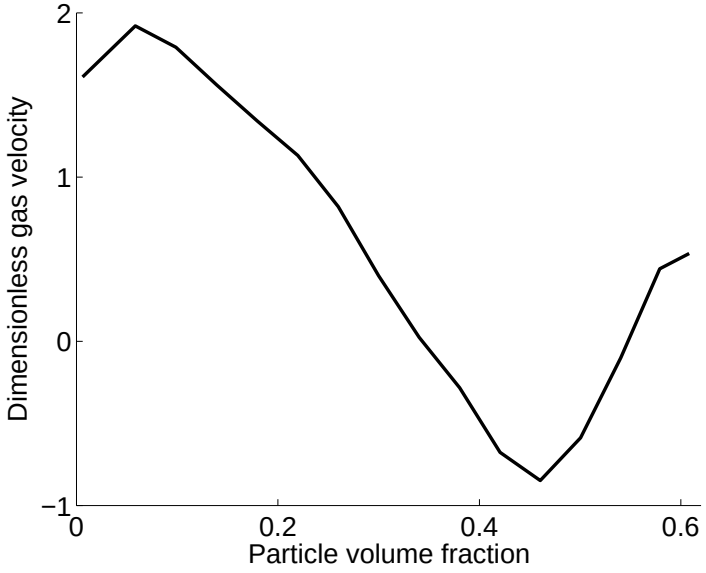

Figure 3.10: Average of gas velocity conditioned by the particle volume fraction. The gas velocity is made dimensionless using the superficial gas velocity.

width and the particle relaxation time. A dimensionless mesh size, depending both on the mesh size, the bed width and the particle relaxation time, was used to express a general law of mesh dependance of the bed expansion.

The filtered approach was used to enable coarse-grid simulations but some unknown terms have to be modelled. Using a highly resolved simulation, we have first shown that the first order term that needs to be modelled is the unresolved part of the filtered drag. Then, using a correlative analysis, the problem was reduced to the prediction of a subgrid drift velocity coming from spatial inhomogeneities inside the filtered volume and correlation between gas velocity and particle volume fraction. A mathematical analysis for small filter sizes has shown a square dependence of the subgrid drift velocity.

Chapter 4

Functional modelling of the subgrid drift velocity

4.1 Introduction

Various methods are proposed in the literature to modify the drag term in order to obtain the correct bed expansion (for a state-of-the art review, we refer to Wang (2009)). McKeen and Pugsley (2003) suggested to use a scale factor between 0.2 and 0.3 for the commonly-used gas-solid drag laws. With this factor, their numerical simulations fit their experimental results well. Following the same analysis, Hosseini et al. (2009) used a scale factor of 0.1 to fit their own experiments. Gao et al. (2009) used an effective mean diameter of 300 μm for the dense phase of their turbulent fluidized bed, corresponding to a scale factor of 0.04. None of the authors propose a generic law to estimate this scale factor.

Andrews IV et al. (2005) suggest using an ad-hoc effective drag coefficient to perform simulation of a large-scale circulating fluidized bed on a coarse grid. Their effective drag coefficient is measured using the highly resolved simulations of periodic flows obtained by Agrawal et al. (2001) and depends on the particle volume fraction. Following the same approach, Igci et al. (2008) propose an effective drag coefficient that depends on the size of the filter used, i.e. the size of the grid used in numerical simulations.

Recently, the EMMS method has been applied to the prediction of the hydrodynamics inside a bubbling fluidized bed (Wang and Liu, 2010). The EMMS method, originally developed by Li and Kwauk (1994) to predict steady flows inside circulating fluidized beds, assumes that particles move in the form of clusters through a dilute phase composed by the surrounding gas and a few randomly distributed particles. The EMMS method was integrated into the Eulerian formalism in the form of a subgrid drag correction (Wang and

Li, 2007). The last revised EMMS model can be found in Wang et al. (2008). Clusters are described by 10 parameters that are calculated by balance laws and an energy minimization condition. While a good agreement is found between simulation results of Wang and Liu (2010) and experimental results, the description of the flow in the form of clusters is very questionable in a dense bubbling fluidized bed where bubbles move inside a dense phase composed of little gas and highly concentrated particles.

Finally, Wang et al. (2010) show that a correction of the drag law is also needed when performing coarse grid simulations of industrial-scale bubbling fluidized beds with Geldart B particles. By assuming that the flow inside each computational cell is divided into a dense zone, where the relative velocity is given by a homogeneous expansion law (Richardson and Zaki, 1954), and a dilute zone where no particles are present, the authors propose a simple modification of the drag law. Such a relationship between the gas velocity and the particle volume fraction is a very limitating parameter.

In this part, a first model will be proposed to close the subgrid drift velocity that was highlighted in the previous chapter. This model is called the "Functional model" because it assumes that the function of the drift velocity is to reduce the effective relative velocity. Hence it is expressed as a correction to the resolved drag depending on the filtered particle volume fraction and the filter size. This model will be constructed using results of the highly resolved simulation. Moreover, a dynamic procedure will be used to adjust a tuning parameter. Finally this model will be first tested *a priori* using the highly resolved simulation and then tested *a posteriori* on coarse-grid simulations.

4.2 Drag model description

4.2.1 General form

In previous sections we have shown that the subgrid drift velocity defined by Eq. 7.6 needs to be modelled in order to predict the filtered drag force. The generic form to model it is given by:

$$\begin{aligned} \widetilde{V}_{d,i} \;=\; & \mathcal{F}(\overline{\Delta}^{*},\, \overline{\alpha}_p,\, \frac{\widetilde{W}_{r,j}}{\tau_p^{St} g}, \\ & \overline{\Delta}\,\frac{\partial \overline{\alpha}_p}{\partial x_j},\, \overline{\Delta}\,\frac{\partial \widetilde{U}_{g,j}}{\partial x_k},\, \overline{\Delta}\,\frac{\partial \widetilde{U}_{p,j}}{\partial x_k},\, \ldots, \\ & D_1,\, D_2,\, \ldots,\, D_n) \end{aligned} \tag{4.1}$$

where $D_1, D_2, \ldots, D_n$ are dimensionless numbers that characterize the problem. The first dots refer to the combination of derivatives of variables. $\overline{\Delta}^*$ is a dimensionless parameter constructed with the filter size and the macroscopic fluidization parameters (bed width, ...). As the first effect of the subgrid drift velocity is to reduce the apparent relative velocity, we assume that it can be modelled by a simpler form:

$$\widetilde{V}_{d,i} = g(\overline{\Delta}^*, \overline{\alpha}_p)\ K_{ij}\, \widetilde{W}_{r,j} \tag{4.2}$$

where K_{ij} are constants and g is a function of the filtered particle volume fraction and a dimensionless filter size. Due to geometrical properties, it is assumed that $K_{xy} = K_{yx} = 0$. Only K_{xx} and K_{yy} have to be estimated and Eq. 4.2 can be written:

$$\widetilde{V}_{d,\alpha} = g(\overline{\Delta}^*, \overline{\alpha}_p)\ K_{\alpha\alpha}\, \widetilde{W}_{r,\alpha} \tag{4.3}$$

where the Greek subscript α is used to indicate that there is no implicit summation. The g function will be determined in Section 4.2.2 using the database provided by the fully resolved simulation and K_{ij} constants will be dynamically adjusted following a methodology adapted from Germano et al. (1991) and Lilly (1992) described in Section 4.2.3.

4.2.2 Volume fraction and filter size dependence

In this section, K_{yy} is assumed to be equal to one. The g function is determined using the database described in Section 3.5 by:

$$g(\overline{\Delta}^*, \overline{\alpha}_p) = < \widetilde{V}_{d,y} \,|\, \overline{\alpha}_p >_{b,t} \ / \ < \widetilde{W}_{r,y} \,|\, \overline{\alpha}_p >_{b,t} \tag{4.4}$$

where $< A \,|\, B >_{b,t}$ denotes the conditional average of A by B. g is plotted as a function of $\overline{\alpha}_p$ in Figure 4.1 for different values of $R = \Delta_B/\Delta_D$. As the shape of the function is nearly independent of R, g can be written as:

$$g(\overline{\Delta}^*, \overline{\alpha}_p) \simeq f(\overline{\Delta}^*)\ h(\overline{\alpha}_p) \tag{4.5}$$

where $f(\overline{\Delta}^*)$ and $h(\overline{\alpha}_p)$ are two independent functions. Measured values of h are represented in Figure 4.2 for different R. The following suggested form for h is obtained by fitting the measurements:

$$h(\overline{\alpha}_p) = -\sqrt{u}\ (1-u)^2\ (1 - 1.88\ u + 5.16\ u^2) \tag{4.6}$$

with $u = \overline{\alpha}_p \ / \ \alpha_m$ and $\alpha_m = 0.64$ representing the maximum loading. The suggested form for h was imposed to vanish when the filtered particle volume fraction was equal

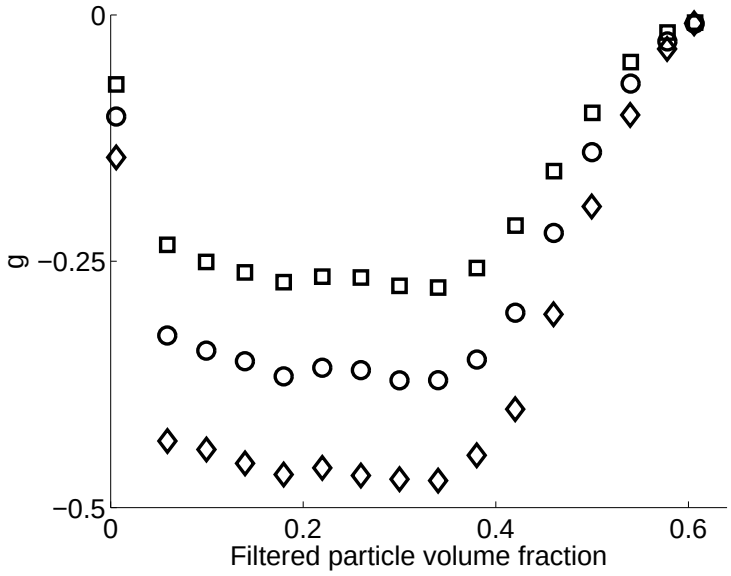

Figure 4.1: Measured values of g versus the filtered particle volume fraction $\overline{\alpha}_p$. □: $R = 11$, ○: $R = 15$, ◇: $R = 21$.

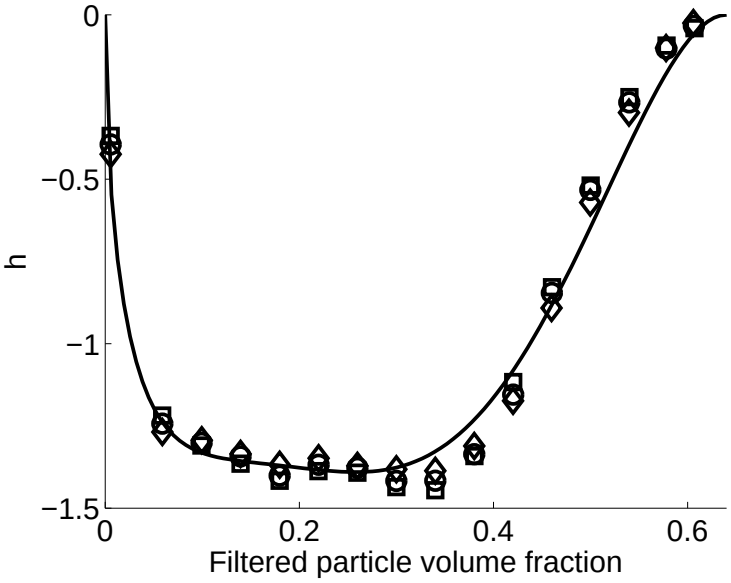

Figure 4.2: h versus the filtered particle volume fraction $\overline{\alpha}_p$. Symbols are obtained from the database. □: $R = 11$, ○: $R = 21$, ◇: $R = 31$, —— : Eq. 4.6.

Case	a
Ref.	$6.13 \cdot 10^{-2}$
$U_f = 0.1\ m/s$	$6.58 \cdot 10^{-2}$
$L \ = 0.06\ m$	$5.72 \cdot 10^{-2}$

Table 4.1: Measured values of a for different cases. Ref. is the case describe in Section 3.5. Other cases differ only as noted.

to either zero or the maximum loading. In these two cases, the particle volume fraction inside the filtering box is homogeneous. Hence, no correction to the filtered drag is needed. The maximum of the correction occurs for intermediate filtered particle volume fractions, reflecting the trend of the flow to lead to preferential particle volume fractions close to zero or to the maximum packing fraction, as shown in Figure 3.4.

The subgrid drift velocity dependence on the filter size is measured by:

$$f(\overline{\Delta}^*) = \frac{< \overline{\alpha}_p \widetilde{V}_{d,y} >_{b,t}}{< \overline{\alpha}_p \, h(\overline{\alpha}_p) \widetilde{W}_{r,y} >_{b,t}} \tag{4.7}$$

f is plotted in Figure 4.3 and the following form is proposed:

$$f(\overline{\Delta}^*) = \frac{\overline{\Delta}^{*2}}{a^2 + \overline{\Delta}^{*2}} \tag{4.8}$$

with $a \approx 6.13 \cdot 10^{-2}$ and $\overline{\Delta}^*$ given by:

$$\overline{\Delta}^* = \frac{\overline{\Delta}/\tau_p^{St}}{\sqrt{g \ D_H}} \tag{4.9}$$

where $g = \| \mathbf{g} \|$ is the norm of the gravity acceleration and $D_H = 2\,L$ the bed hydraulic diameter. Table 4.1 reports values of a obtained for a halved superficial gas velocity or a doubled bed width. The value is nearly case-independent. For small filter size, Eq. 4.8 leads to a parabola, which is consistent with the Taylor development given by Eq 3.45. For wide filter size, the filtered flow is homogeneous and the resolved part of the filtered drag reaches its maximal value. Consequently f reaches a constant value, as shown in Figure 4.3.

4.2.3 Dynamic adjustment

Values of K_{xx} and K_{yy} depend on the simulated case. We propose to calculate them using a dynamic adjustment (Germano et al., 1991). The main idea is that the model described

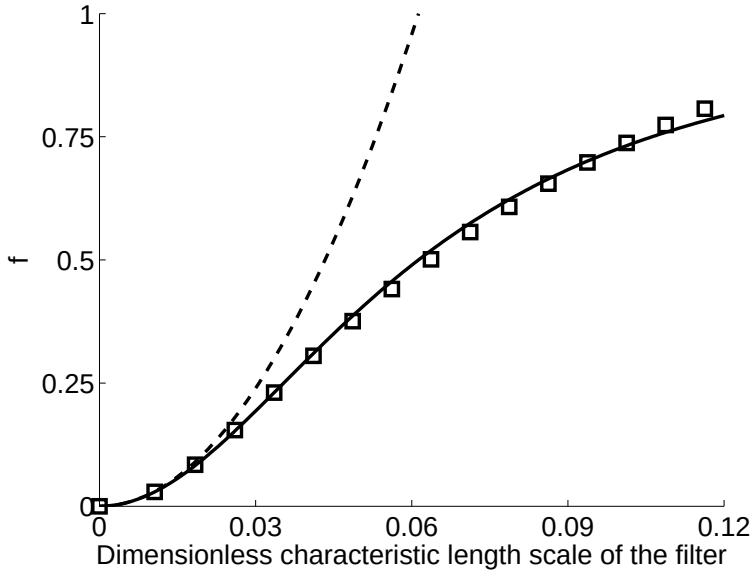

Figure 4.3: Evolution of f with respect to the dimensionless characteristic length scale of the filter, $\overline{\Delta}^*$. □: measured values, —— : Eq. 4.8, - - - : parabola.

in Eq. 4.3 is independent of the choice of the weight function G used to calculate filtered values. Therefore K_{ij} could be calculated by performing a second filter operation on the filtered quantities. This second filter, called the test filter, is applied during coarse grid simulations on resolved quantities.

Let us define $\widehat{\overline{f}}$ by:

$$\begin{aligned}\widehat{\overline{f}}(\mathbf{x},t) = \frac{1}{5} \quad (\quad & \overline{f}(\mathbf{x},t) \\ + \quad & \overline{f}(\mathbf{x}+\Delta_G\,\mathbf{e_x},t) + \overline{f}(\mathbf{x}-\Delta_G\,\mathbf{e_x},t) \\ + \quad & \overline{f}(\mathbf{x}+\Delta_G\,\mathbf{e_z},t) + \overline{f}(\mathbf{x}-\Delta_G\,\mathbf{e_z},t)\ )\end{aligned} \tag{4.10}$$

where $\Delta_G \geq \Delta_B$. Eq. 4.10 can be written in the form of a filtering operation on f. Its associated weight function has a characteristic length scale $\widehat{\overline{\Delta}}$ linked to $\overline{\Delta}$ by:

$$\widehat{\overline{\Delta}}^2 = \overline{\Delta}^2 + \frac{24}{5}\,\Delta_G^2 \tag{4.11}$$

The filter associated with Eq. 4.10 is called the test filter.

Figures 4.4 and 4.5 show that calculating filtered quantities by Eq. 3.26 with the discrete box filter or the test filter leads to the same values for f and h. In consequence, one can

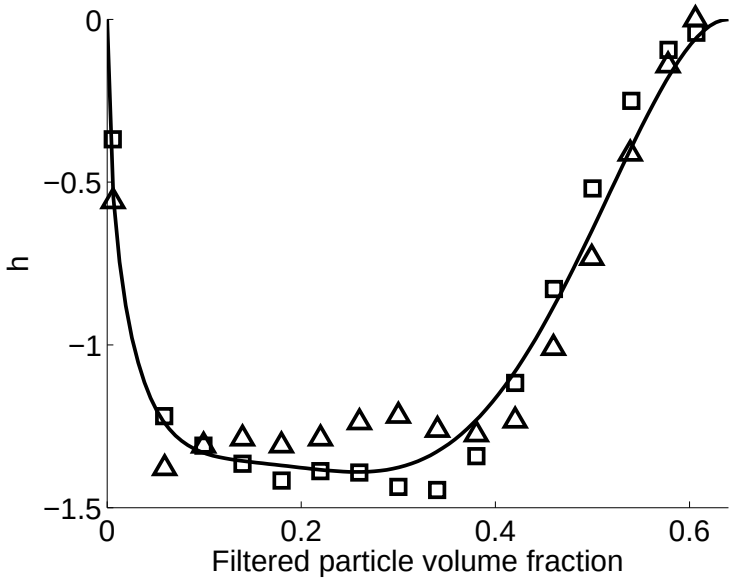

Figure 4.4: h as a function of the filtered particle volume fraction, $\overline{\alpha}_p$ or $\widehat{\overline{\alpha}}_p$. Symbols are obtained from the database. □: $R = 11$, discrete box filter, △: $R = 11$, test filter with $\Delta_G = \Delta_B$, —— : Eq. 4.6.

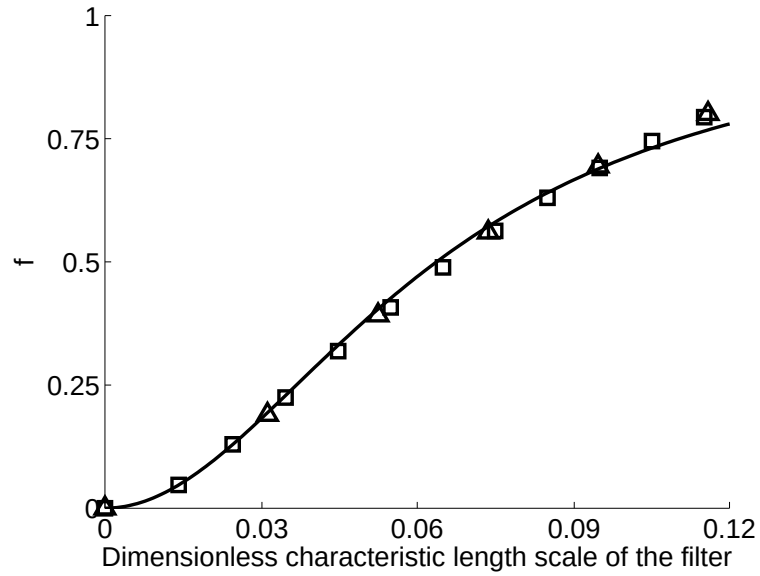

Figure 4.5: Evolution of f with respect to the dimensionless characteristic length scale of the filter, $\overline{\Delta}^*$ or $\widehat{\overline{\Delta}}^*$. □: measured values with the box filter, △: measured values with the test filter, —— : Eq. 4.8.

write both:

$$\overline{\alpha_p V_{r,\alpha}} = \overline{\alpha}_p \widetilde{W}_{r,\alpha} \left(1 + K_{\alpha\alpha}\, f(\overline{\Delta}^*)\; h(\overline{\alpha}_p)\right) \tag{4.12}$$

and

$$\widehat{\overline{\alpha_p V_{r,\alpha}}} = \widehat{\overline{\alpha}}_p \widehat{\widetilde{W}}_{r,\alpha} \left(1 + K_{\alpha\alpha}\, f(\widehat{\overline{\Delta}}^*)\; h(\widehat{\overline{\alpha}}_p)\right) \tag{4.13}$$

where $\widehat{\widetilde{W}}_{r,i}$ is defined by:

$$\widehat{\widetilde{W}}_{r,i} = \widehat{\widetilde{U}}_{g,i} - \widehat{\widetilde{U}}_{p,i} \tag{4.14}$$

with $\widehat{\widetilde{U}}_{p,i} = \widehat{\overline{\alpha_p U_{p,i}}} \;/\; \widehat{\overline{\alpha}}_p$ and $\widehat{\widetilde{U}}_{g,i} = \widehat{\overline{\alpha_g U_{g,i}}} \;/\; \widehat{\overline{\alpha}}_g$. By applying $(\,\hat{.}\,)$ operation on Eq. 4.12 then putting the result into Eq. 4.13, and assuming moreover that the scale of variation of $K_{\alpha\alpha}$ is much larger than the grid size:

$$\left(K_{\alpha\alpha}\widehat{\overline{\alpha}_p h(\overline{\alpha}_p)\widetilde{W}_{r,\alpha}}\right) \simeq K_{\alpha\alpha} \left(\widehat{\overline{\alpha}_p h(\overline{\alpha}_p)\widetilde{W}_{r,\alpha}}\right) \tag{4.15}$$

$K_{\alpha\alpha}$ can be evaluated:

$$K_{\alpha\alpha} \simeq -\frac{L_\alpha}{M_\alpha} \tag{4.16}$$

with L_α and M_α defined by:

$$L_\alpha = \widehat{\overline{\alpha}_p \widetilde{W}_{r,\alpha}} - \widehat{\overline{\alpha}}_p \widehat{\widetilde{W}}_{r,\alpha} \tag{4.17}$$

$$M_\alpha = f(\overline{\Delta}^*)\; (\widehat{\overline{\alpha}_p h(\overline{\alpha}_p)\widetilde{W}_{r,\alpha}}) - f(\widehat{\overline{\Delta}}^*)\; \widehat{\overline{\alpha}}_p h(\widehat{\overline{\alpha}}_p)\widehat{\widetilde{W}}_{r,\alpha} \tag{4.18}$$

4.2.4 Recapitulation

To summarize, we model the filtered drag force by:

$$\overline{\left(\frac{\alpha_p \rho_p}{\tau_p}\, V_{r,\alpha}\right)} = \frac{\overline{\alpha}_p \rho_p}{\widetilde{\tau}_p} \left(1 + f(\overline{\Delta}^*)\; h(\overline{\alpha}_p)\; K_{\alpha\alpha}\right) \widetilde{W}_{r,\alpha} \tag{4.19}$$

where $f(\overline{\Delta}^*)$, $h(\overline{\alpha}_p)$ and $K_{\alpha\alpha}$ are evaluated using Eqs. 4.8, 4.6 and 4.16.

4.3 A priori validation

The highly resolved simulation results can be also used as a validation tool, to assess the validity of the model developed. All filtered quantities are known, making comparison possible between the real filtered drag and the modelled one. The correction of the drag

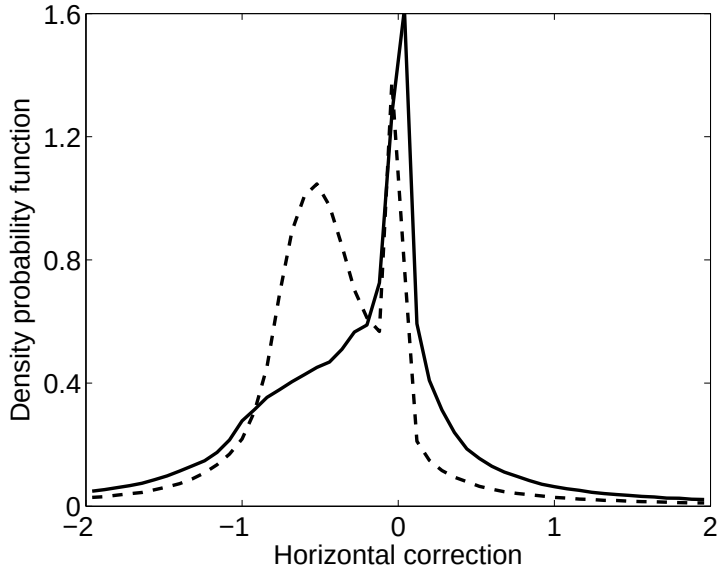

Figure 4.6: Probability density function of the horizontal correction of the drag, C_x, for $\Delta_B = 21\ \Delta_D$ and $\Delta_G = \Delta_B$, corresponding to $\overline{\Delta}^* \simeq 0.10$. —— : measured value, - - - : model prediction.

C_α in the α direction is defined by:

$$\overline{\frac{\alpha_p \rho_p}{\tau_p} V_{r,\alpha}} = \frac{\overline{\alpha}_p \rho_p}{\widetilde{\tau}_p} \widetilde{W}_{r,\alpha}\ (1 + C_\alpha) \tag{4.20}$$

Putting Eq. 4.20 in Eq. 7.7 leads to the following model for C_α:

$$C_\alpha = f(\overline{\Delta}^*)\ h(\overline{\alpha}_p)\ K_{\alpha\alpha} \tag{4.21}$$

Figures 4.6 and 4.7 compare the probability density function of C_x and C_y measured in the bed with the prediction of Eq. 4.21, for $\Delta_B = 21\ \Delta_D$, corresponding to $\overline{\Delta}^* \simeq 0.10$, and $\Delta_G = \Delta_B$. Reasonable agreement is found. As seen in Figures 4.6 and 4.7, C_α could take values lower than -1. Such values result in a filtered drag force in the direction opposite to its resolved part (see Eq. 4.20).

Figures 4.8 and 4.9 compare the probability density function of $\overline{\alpha}_p \widetilde{V}_{d,x}$ and $\overline{\alpha}_p \widetilde{V}_{d,y}$ measured in the bed with the model prediction for $\overline{\Delta}^* \simeq 0.10$ and $\Delta_G = \Delta_B$. Both the probability density function of the horizontal and vertical components of the subgrid drift velocity are fairly well predicted. The probability density functions of the filtered drag, the resolved drag and the filtered drag predicted by the model are shown in Figure 4.10. Fairly

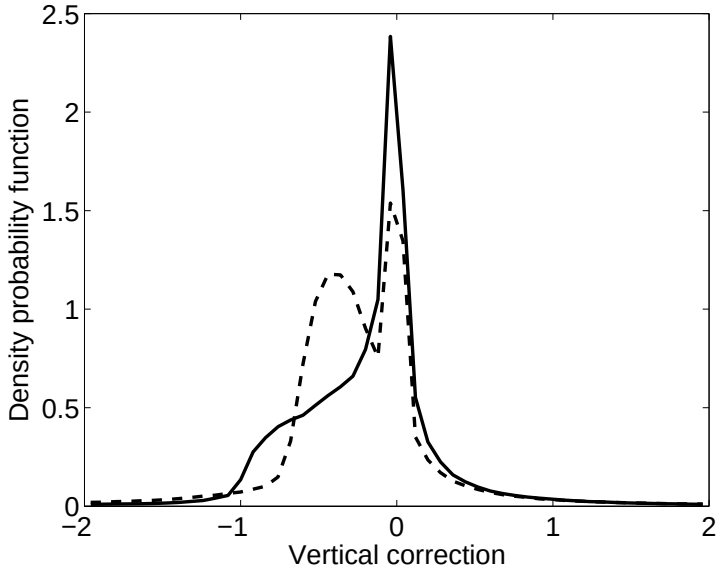

Figure 4.7: Probability density function of the vertical correction of the drag, C_y, for $\Delta_B = 21\,\Delta_D$ and $\Delta_G = \Delta_B$, corresponding to $\overline{\Delta}^* \simeq 0.10$. ——: measured value, - - - : model prediction.

good agreement is again found.

4.4 Coarse-grid simulations

Two-dimensional coarse-grid simulations were performed using the theoretical model developed previously and the results are compared to those obtained in highly resolved simulations. The theoretical developments rely on an abstract filter. A coarse-grid simulation is assumed to apply an implicit filter on calculated quantities, the length scale of which is proportional to the computational grid. As this implicit filter is unknown, the characteristic length scale $\overline{\Delta}$ is unknown. It is assumed that this length scale is related to the mesh size, Δ_G, by:

$$\overline{\Delta}^2 = 2\,\Delta_G^2 \tag{4.22}$$

The scale factor of 2 was determined empirically.

For each time step and for each cell, K_{xx} and K_{yy} were calculated by applying the $\hat{(\,.\,)}$ operation on the quantities given by the code. As shown in the *a priori* analysis, the corrections C_x and C_y could be less than -1. For numerical stability reasons, these values were set to -0.99. In the same way, predicted values of C_x and C_y greater than 0.99 were

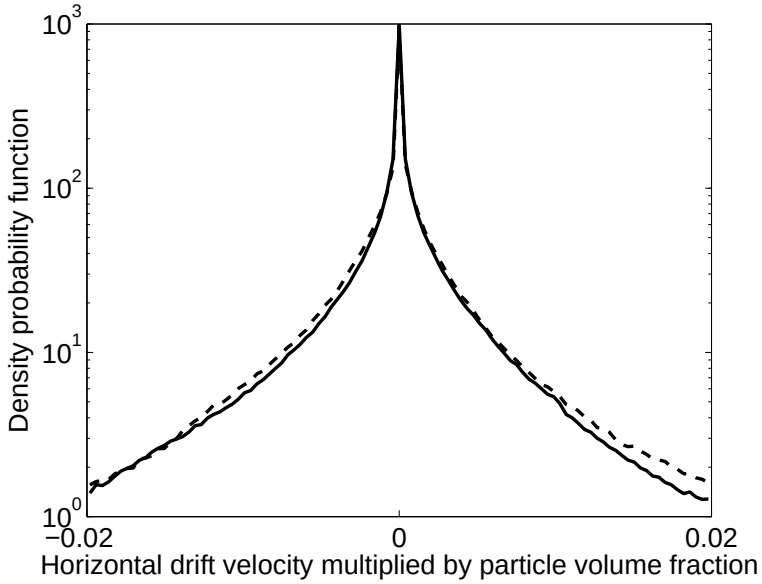

Figure 4.8: Probability density function of the horizontal component of the drift velocity weighted by the filtered particle volume fraction, $\overline{\alpha}_p \widetilde{V}_{d,x}$, for $\Delta_B = 21\ \Delta_D$ ($\overline{\Delta}^* \simeq 0.10$), and $\Delta_G = \Delta_B$. ——— : measured value, - - - : model prediction.

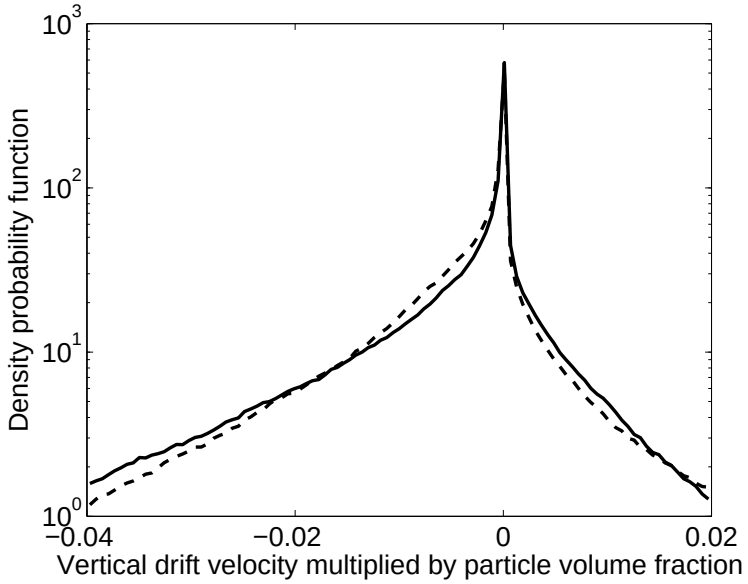

Figure 4.9: Probability density function of the vertical component of the drift velocity weighted by the filtered particle volume fraction, $\overline{\alpha}_p \widetilde{V}_{d,y}$, for $\Delta_B = 21\ \Delta_D$ ($\overline{\Delta}^* \simeq 0.10$), and $\Delta_G = \Delta_B$. ——— : measured value, - - - : model prediction.

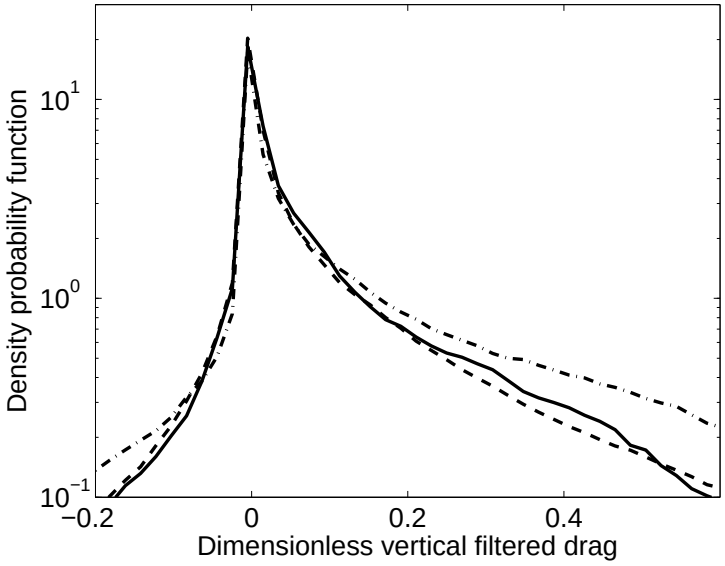

Figure 4.10: Probability density function of the dimensionless vertical component of the filtered drag for $\Delta_B = 21\ \Delta_D$ ($\overline{\Delta}^* \simeq 0.10$), and $\Delta_G = \Delta_B$. ——— : measured value, - - - : model prediction, -·-·- : resolved drag.

set to 0.99. As seen in Figures 4.6 and 4.7 these events are very infrequent so they are expected to have a negligible effect.

4.4.1 Coarse-grid simulation of the reference case

The reference case defined in Section 3.5 is used to validate the model. Simulations were performed on meshes of sizes 2 mm and 1 mm. A snapshot of the particle volume fraction obtained on the 2 mm-size mesh is shown in Figure 4.11. As shown in Figure 4.12, the correct bed expansion is well predicted with the two coarse meshes.

We define K_{yy}^{moy} the time average of K_{yy} by:

$$K_{yy}^{moy} = \frac{\int \frac{\overline{\alpha}_p \rho_p}{\widetilde{\tau}_p}\ \widetilde{W}_{r,y}\ f(\overline{\Delta}^*)\ h(\overline{\alpha}_p)\ K_{yy}\ dt}{\int \frac{\overline{\alpha}_p \rho_p}{\widetilde{\tau}_p}\ \widetilde{W}_{r,y}\ f(\overline{\Delta}^*)\ h(\overline{\alpha}_p)\ dt} \tag{4.23}$$

Vertical profiles of K_{yy}^{moy} for different the meshes are shown in Figure 4.13. Oscillations on profiles of K_{yy}^{moy} are due to the non-convergence of the time average operation since the particle volume fraction is very low. The theory developed assumes that K_{xx} is independent of the size of the mesh cells. However, its value changes slightly between the two coarse-grid simulations and this is probably due to errors in modelling f. Moreover the value of K_{yy}^{moy}

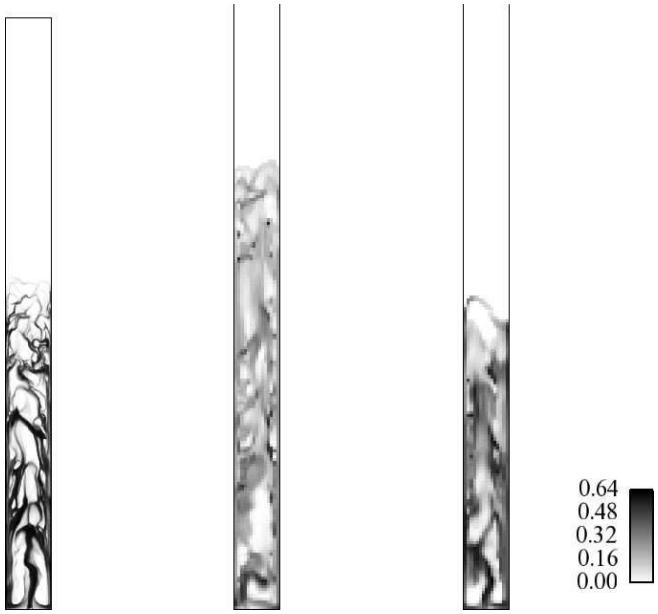

Figure 4.11: Instantaneous particle volume fraction field. Fully resolved simulation (without any subgrid drag model) is at the left. Simulation on a 2 mm grid mesh size without and with the model are at the center and at the right respectively.

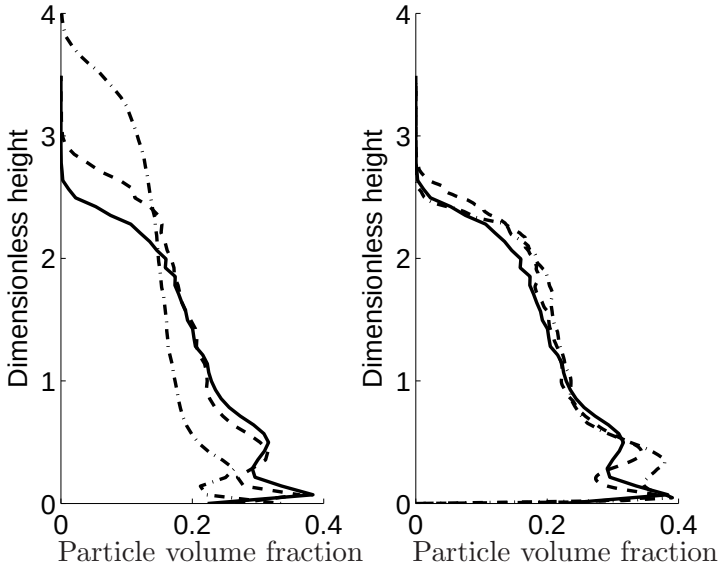

Figure 4.12: Vertical profiles of particle volume fraction. Simulations results without and with the drag model are at the left and the right respectively. —— : $\Delta_G = 100\ \mu m$ (fully resolved simulation), - - - : $\Delta_G = 1\ mm$, -·-· :$\Delta_G = 2\ mm$.

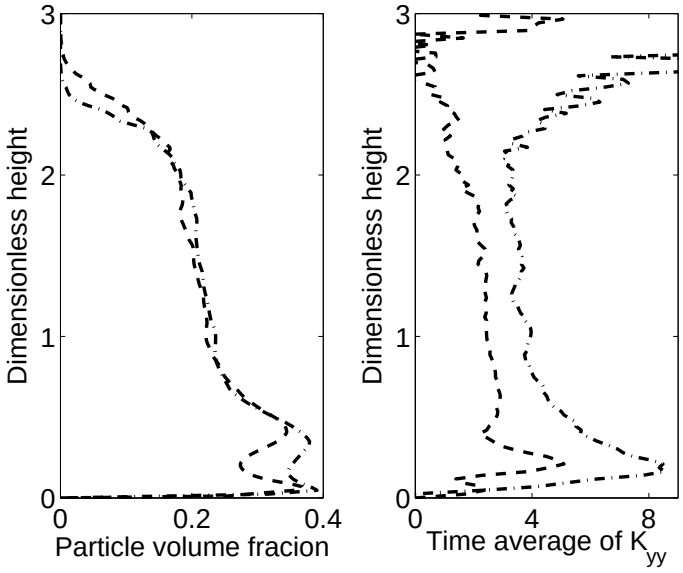

Figure 4.13: Vertical profiles of particle volume fraction and time average of K_{yy}, K_{yy}^{moy}. ---- : $\Delta_G = 1\ mm$, -·-·- :$\Delta_G = 2\ mm$.

depends on the position within the bed.

4.4.2 Coarse-grid simulation of Geldart B bubbling fluidized bed

While it has been shown that the model gives satisfactory results in the reference case, it should be also verified that the model vanishes when simulations without any model give satisfactory results. This fact is clearly not the case for scaling factor models.

A Geldart B fluidized bed with parameters extracted from Makkawi et al. (2006) experiments is simulated (*cf.* Table 4.2). Coarse-grid simulations without any drag modification lead to good agreement with experimental measurements of the bed expansion (Makkawi et al. (2006) or see Section 3.2.4). Therefore we expect that no significant changes will appear when using the developed model. This is shown in Figure 4.14 where the results obtained on a mesh size of 9.86 mm are putted. Consequently, it can be concluded that the model can be applied even if it is not needed.

4.5 Extension to three-dimensional cases

The results obtained previously were gathered in a two-dimensional case. Igci et al. (2008) report that, although there are quantitative differences between the 2D and 3D results, they

Bed width L	0.138 cm
Particle diameter d_p	350 μm
Particle density ρ_p	2 500 kg/m^3
Restitution coefficient e_c	0.80
Gas density ρ_g	1.4 kg/m^3
Gas viscosity μ_g	1.8 10^{-5} $Pa.s$
Superficial gas velocity U_f	0.54 m/s

Table 4.2: Physical parameters of the Geldart B fluidized bed

are qualitatively similar. We performed simulations of a bubbling fluidized bed in a 3D bed with a square section of 0.03 m width. Gas and particle characteristics were identical to the test case. The superficial gas velocity was 0.1 m/s. The initial bed height was 0.03 m with a particle volume fraction of 0.55. The domain height was 0.09 m. The cells of the mesh were cubes of 250 μm width, corresponding to $120 \times 120 \times 360 = 5\ 184\ 000$ cells. A snapshot of the particle volume fraction field is shown in Figure 4.15.

Correlative analysis indicates that the subgrid drift velocity can still be identified as Eq. 7.6. As seen in Figure 4.16, h is more independent of the filtered particle volume fraction than it is in the 2D case. However the mesh is still too coarse to measure the function f correctly.

The test filter defined by Eq. 4.10 becomes, for three-dimensional cases:

$$\begin{aligned}\widehat{\overline{f}}(\mathbf{x},t) = \frac{1}{7} \quad (\quad & \overline{f}(\mathbf{x},t) \\ + \quad & \overline{f}(\mathbf{x}+\Delta_G\mathbf{e_x},t) + \overline{f}(\mathbf{x}-\Delta_G\mathbf{e_x},t) \\ + \quad & \overline{f}(\mathbf{x}+\Delta_G\mathbf{e_y},t) + \overline{f}(\mathbf{x}-\Delta_G\mathbf{e_y},t) \\ + \quad & \overline{f}(\mathbf{x}+\Delta_G\mathbf{e_z},t) + \overline{f}(\mathbf{x}-\Delta_G\mathbf{e_z},t) \ )\end{aligned} \tag{4.24}$$

Then, $\widehat{\overline{\Delta}}$ is linked to $\overline{\Delta}$ by:

$$\widehat{\overline{\Delta}}^2 = \overline{\Delta}^2 + \frac{24}{7}\ \Delta_G^2 \tag{4.25}$$

For two-dimensional simulations in the (x,z) plane, K_{xx} and K_{yy} are calculated using Eq. 4.16. In three-dimensional simulations, where the gravity is in the z-direction, it is assumed that $K_{xx} = K_{yy}$. Then, following Lilly (1992), K_{xx} and K_{yy} are calculated by:

$$K_{xx} = K_{yy} = -\frac{L_x M_x + L_y M_y}{M_x^2 + M_y^2} \tag{4.26}$$

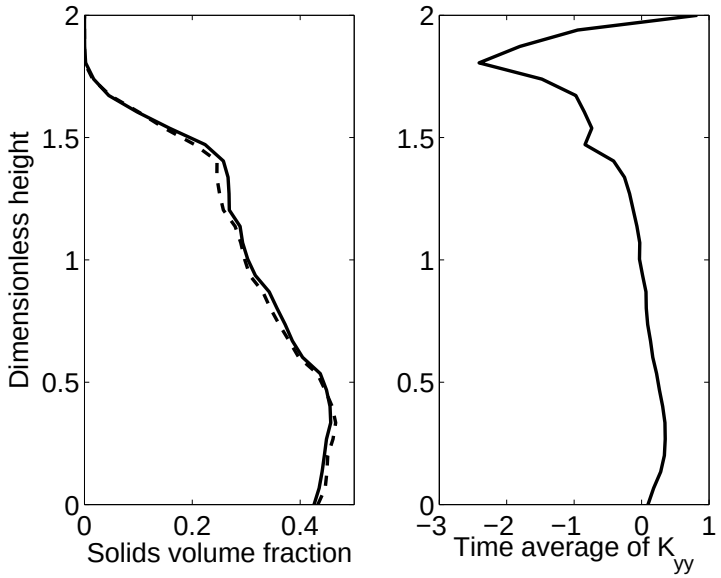

Figure 4.14: Vertical profiles of particle volume fraction and K_{yy}^{moy} for the Geldart B bubbling fluidized bed. At left, —— : without subgrid drag model, - - - : with the subgrid drag model. At right, —— : K_{yy}^{moy}.

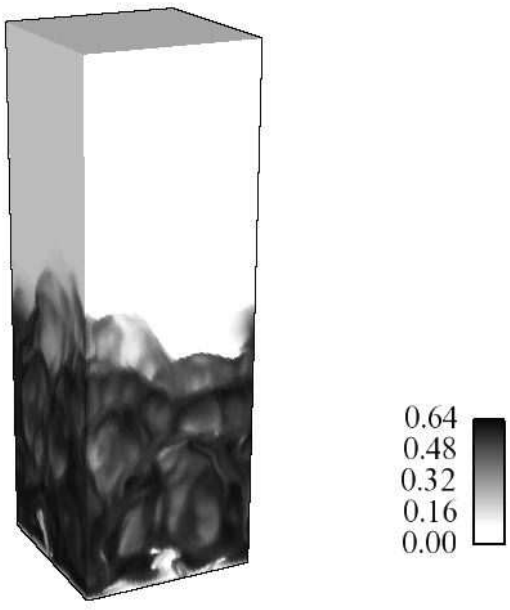

Figure 4.15: Snapshot of a the particle volume fraction field in the three-dimensional fluidized bed.

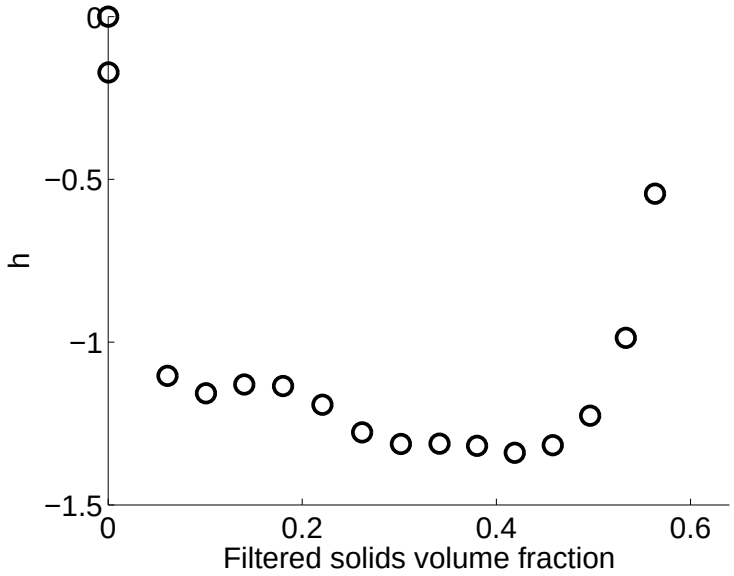

Figure 4.16: Measured values of as a function of the filtered particle volume fraction $\overline{\alpha}_p$ for the three-dimensional fluidized bed. Filtering was performed using the box filter with $R = 15$.

4.6 Conclusion

The subgrid drift velocity was modelled as a function of the filtered particle volume fraction, the resolved relative velocity and the filter size. The model is adjusted using a dynamic procedure adapted from single-phase turbulence modelling. Tests on coarse-grid simulations have shown a good prediction of the bed expansion for any mesh size. Finally, an extension to three-dimensional cases has been suggested.

Chapter 5

Structural modelling of the subgrid drift velocity

5.1 Introduction

5.1.1 The drift tensor

Structural modelling in LES is based on mathematical properties of the filtering operation. Hence it can be used in a straightforward way, since it does not rely on any assumption dealing with the nature of subgrid transfers (Sagaut, 2001). The drift velocity can be expressed as a subgrid scalar flux in the LES approach by noting that:

$$\overline{\alpha}_g \, \overline{\alpha}_p \, \widetilde{V}_{d,i} = \overline{\alpha_p \, U_{g,i}} - \overline{\alpha}_p \, \overline{U}_{g,i} = \tau_i \tag{5.1}$$

with τ_i the analogue of the subgrid scalar flux defined in the case of the transport of a scalar. Structural models can be directly applied to model this vector, which will be called the subgrid drift vector below.

Two different structural models will be tested: the gradient model and the scale similarity model. This will lead us to a two-parameter model in order to obtain better correlation and average for large filter sizes. All these models will be compared a priori and tested on a posteriori simulations.

5.1.2 Consistent a priori analysis

A priori analysis will be performed using the database of the reference case with the 100 μm mesh size. Variables will be filtered using a discrete version of the box filter (see Section

3.5). The resulting characteristic length scale $\overline{\Delta}$ is linked to the box filter width Δ_B by:

$$\overline{\Delta}^2 = \Delta_B^2 \ \left(1 - (\Delta_D/\Delta_B)^2\right) \tag{5.2}$$

where $\Delta_D = 100\ \mu m$ is the mesh size used to provide the database.

In a posteriori simulations, derivatives of filtering of variables appearing in structural models will be calculated on the mesh used to perform simulations. A priori analysis taking into account the discrete nature of the a posteriori simulation is called the consistent a priori test (Liu et al., 2006). It is assumed that the implicit filter of a posteriori simulations is a box filter of characteristic length scale $\overline{\Delta} = 2\,\Delta_G$, where Δ_G is the grid size. As the discrete version of the box filter is performed for width $\Delta_B = (2\,k+1)\,\Delta_D$, with $k \in \mathbb{N}$, we have $\overline{\Delta} \simeq 2\,k\Delta_D$. Hence, derivatives will be calculated by assuming that $\Delta_G = k\Delta_D$. As k increases, $\Delta_G \to \overline{\Delta}/2$.

5.2 Germano's Consistent Decomposition

The subgrid drift vector can be decomposed following Germano's consistent decomposition (Germano, 1986):

$$\tau_i = \mathcal{L}_i + \mathcal{C}_i + \mathcal{R}_i \tag{5.3}$$

in which the vectors $\mathcal{L}$, $\mathcal{C}$ and $\mathcal{R}$ are defined as:

$$\mathcal{L}_i = \overline{\overline{\alpha}_p\,\widetilde{U}_{g,i}} - \overline{\overline{\alpha}}_p\,\overline{\widetilde{U}}_{g,i} \tag{5.4}$$

$$\mathcal{C}_i = \overline{\overline{\alpha}_p\,U''_{g,i}} - \overline{\overline{\alpha}}_p\,\overline{U''_{g,i}} + \overline{\alpha'_p\,\widetilde{U}_{g,i}} - \overline{\alpha'_p}\,\overline{\widetilde{U}}_{g,i} \tag{5.5}$$

$$\mathcal{R}_i = \overline{\alpha'_p\,U''_{g,i}} - \overline{\alpha'_p}\,\overline{U''_{g,i}} \tag{5.6}$$

with $\alpha'_p = \alpha_p - \overline{\alpha}_p$ and $U''_{g,i} = U_{g,i} - \widetilde{U}_{g,i}$ the fluctuating particle volume fraction and gas velocity. Figure 5.1 represents the average over the whole domain and time of the three terms appearing in this decomposition. After a square dependence in $\overline{\Delta}$, $< \tau_y >_{b,t}$ increases in a linear way.

As expected, the Leonard part $\mathcal{L}_y$ is a good approximation of the subgrid drift vector for small filter sizes ($\overline{\Delta} < 5\,\Delta_D$). For $\overline{\Delta} = 10\,\Delta_D$, we have $< \mathcal{C}_y + \mathcal{R}_y >_{b,t} \sim \ \frac{1}{2} < \mathcal{L}_y >_{b,t}$. Hence $< \tau_y >_{b,t} \sim \ \frac{3}{2} < \mathcal{L}_y >$. For $\overline{\Delta} = 20\,\Delta_D$, we have $< \mathcal{C}_y >_{b,t} \sim < \mathcal{R}_y >_{b,t} \sim \ \frac{1}{2} < \mathcal{L}_y >_{b,t}$. Then we have $< \tau_y >_{b,t} \sim \ 2 < \mathcal{L}_y >$. For $\overline{\Delta} = 40\,\Delta_D$, we have $< \mathcal{R}_y >_{b,t} \sim < \mathcal{L}_y >_{b,t} \sim 2 < \mathcal{C}_y >_{b,t}$. Hence $< \tau_y >_{b,t} \sim \ \frac{5}{2} < \mathcal{L}_y >$.

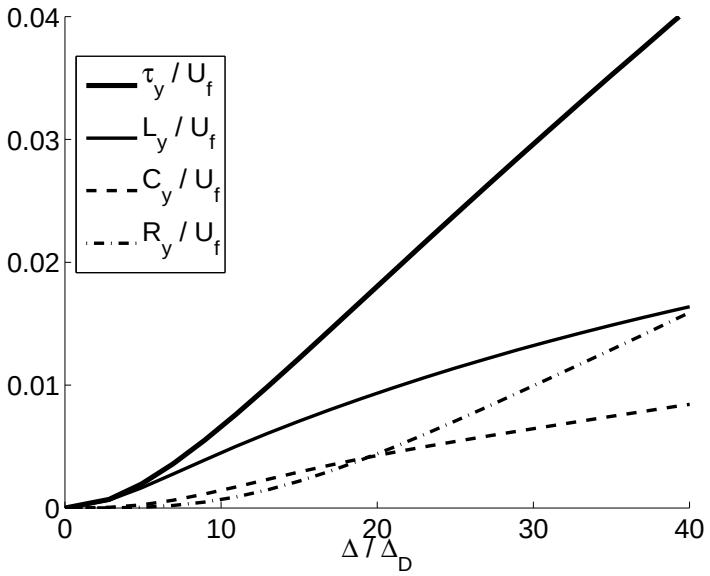

Figure 5.1: Absolute value of the average over the bed of the vertical component of the drift vector and its terms in the Germano's decomposition, as a function of the $\overline{\Delta}/\Delta_D$ ratio.

5.3 Gradient model

5.3.1 Theoretical expression

By expanding α_p and $U_{g,i}$ in Taylor series and performing the filter operation, τ_i can be expressed as:

$$\tau_i = \frac{\overline{\Delta}^2}{12} \frac{\partial \overline{\alpha}_p}{\partial x_j} \frac{\partial \widetilde{U}_{g,i}}{\partial x_j} + O(\overline{\Delta}^4) \tag{5.7}$$

Details of this Taylor analysis can be found in Appendix D. By limiting the Taylor development to the second-order, one can find the analogue of the gradient model or Clark's model used in LES (Clark et al., 1979):

$$\tau_i = C\, \Delta_G^2 \frac{\partial \overline{\alpha}_p}{\partial x_j} \frac{\partial \widetilde{U}_{g,i}}{\partial x_j} \tag{5.8}$$

where C is a constant depending on the ratio between $\overline{\Delta}$, the characteristic length scale of the implicit filter, and Δ_G, the grid size used in a posteriori simulation. By assuming that the implicit filter size is the twice of the grid size, we get $C = 1/3$.

5.3.2 Practical expressions

In a posteriori simulations, exact derivatives $\partial/\partial x_j$ appearing in Eq. 5.8 are approximated using numerical derivatives $\delta/\delta x_j$ on the grid. Due to practical limitations of the code used for a posteriori simulations, only second-order derivatives can be calculated. Using the central second-order scheme for the evaluation of the first derivatives:

$$\frac{\delta\phi}{\delta x_j} = \frac{\phi(\mathbf{x} + \Delta_G\,\mathbf{e_j}) - \phi(\mathbf{x} - \Delta_G\,\mathbf{e_j})}{2\,\Delta_G} \tag{5.9}$$

for $\phi = \overline{\alpha}_p$ and $\phi = \widetilde{U}_{g,i}$, we get a first version of the gradient model:

$$\tau_i = \; C_1\;\Delta_G^2\;\frac{\delta\overline{\alpha}_p}{\delta x_j}\;\frac{\delta\widetilde{U}_{g,i}}{\delta x_j} \tag{5.10}$$

Eqs. 5.8 and 5.10 differ in the fourth-order terms.

A second version of this model can be found by noting that:

$$\frac{\partial\overline{\alpha}_p}{\partial x_j}\;\frac{\partial\widetilde{U}_{g,i}}{\partial x_j} \;=\; \frac{1}{2}\;\left(\Delta(\overline{\alpha}_p\widetilde{U}_{g,i}) - \overline{\alpha}_p\,\Delta(\widetilde{U}_{g,i}) - \widetilde{U}_{g,i}\,\Delta(\overline{\alpha}_p)\right) \tag{5.11}$$

with $\Delta(\phi)$ the Laplacian of ϕ. Using a second-order scheme to evaluate the Laplacian operator:

$$\begin{aligned}\delta^2\phi \;&=\; \left(\phi(\mathbf{x} + \Delta_G\,\mathbf{e_x}) - 2\;\phi(\mathbf{x}) + \phi(\mathbf{x} - \Delta_G\,\mathbf{e_x})\right)/\Delta_G^2 \\ &+\; \left(\phi(\mathbf{x} + \Delta_G\,\mathbf{e_y}) - 2\;\phi(\mathbf{x}) + \phi(\mathbf{x} - \Delta_G\,\mathbf{e_y})\right)/\Delta_G^2\end{aligned} \tag{5.12}$$

we obtain a second version of the gradient model:

$$\tau_i = \; C_2\;\frac{\Delta_G^2}{2}\;\left(\delta^2(\overline{\alpha}_p\widetilde{U}_{g,i}) - \overline{\alpha}_p\;\delta^2\widetilde{U}_{g,i} - \widetilde{U}_{g,i}\;\delta^2\overline{\alpha}_p\right) \tag{5.13}$$

The two versions of the model, Eqs. 5.10 and 5.13, differ in the fourth-order terms. The following sections will show that these terms have an impact on the values of C_1 and C_2 and the correlations obtained.

5.3.3 A priori analysis

The two versions of the gradient model are compared using two criteria. First, the correlation coefficient should be the greatest. Second, as the bed height is given by the average of the subgrid drift velocity over the bed, this one should be correctly predicted, even for high

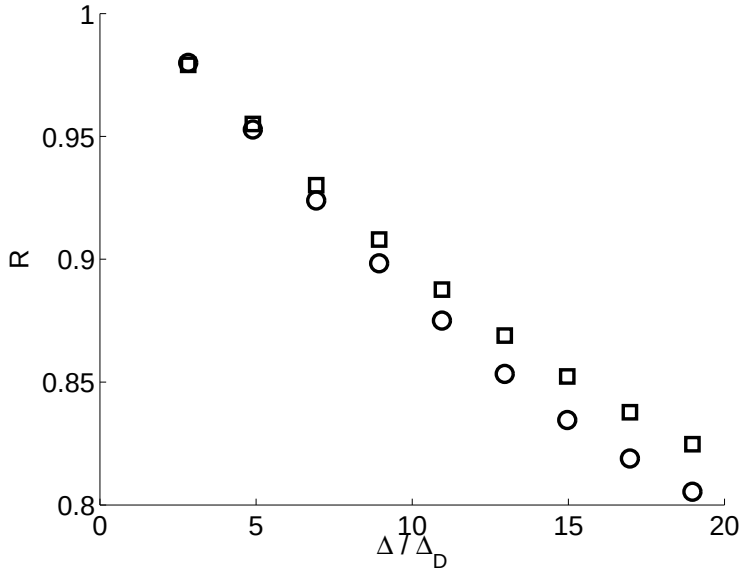

Figure 5.2: Correlation coefficient versus the $\overline{\Delta}/\Delta_D$ ratio. ◯: first version of the gradient model, Eq. 5.10, □: second version of the gradient model, Eq. 5.13

values of $\overline{\Delta}$ once the constant C is fixed. This means that the variation of the constant determined to ensure the same mean of the model and the real subgrid drift tensor should remain constant when $\overline{\Delta}$ increases. As the average of the horizontal component of the subgrid drift tensor over the bed is null - due to the geometrical symmetry - correlation analysis and measurements of C_1 and C_2 will be performed using the vertical component of the subgrid drift vector.

Figure 5.2 compares the correlation of the two models for different $\overline{\Delta}/\Delta_D$ ratios. Even for high values, the correlation is greater than 80 % for the two proposed versions. However, the second version, Eq. 5.13, gives slightly greater values.

C_1 is measured by:

$$C_1 =< \tau_i >_{b,t} \; / < \Delta_G^2 \; \frac{\delta \overline{\alpha}_p}{\delta x_j} \; \frac{\delta \widetilde{U}_{g,y}}{\delta x_j} >_{b,t} \tag{5.14}$$

C_2 is similarly measured using Eq. 5.13. The measured values of C_1 and C_2 are plotted in Figure 5.3. First the values of C_1 and C_2 decrease with $\overline{\Delta}/\Delta_D$. They reach their minimal values, $C_{1,min} = 0.60$ and $C_{2,min} = 0.55$ for a ratio $\overline{\Delta}/\Delta_D \simeq 7$. Then they increase with $\overline{\Delta}/\Delta_D$. What should be considered is the variation of the measured values of C_1 and C_2, as these two values will be set constant in the a posteriori test. It can be seen that C_1

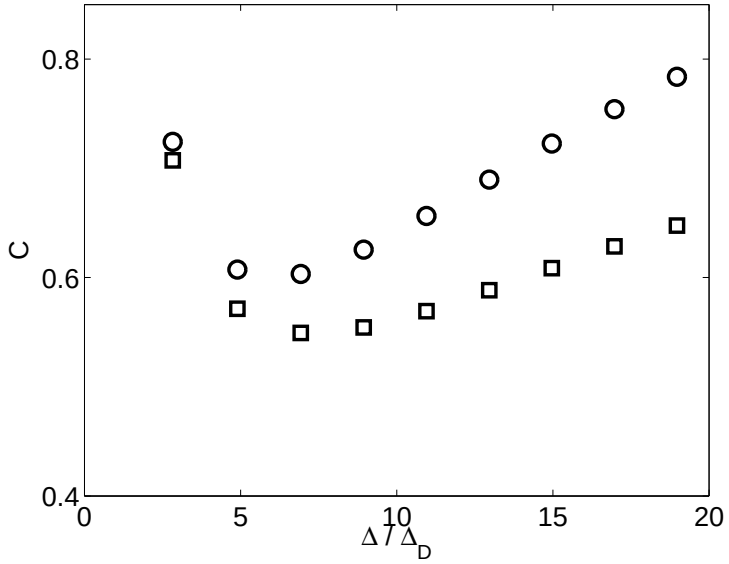

Figure 5.3: Measured values C for the gradient models versus the $\overline{\Delta}/\Delta_D$ ratio. ◯: C_1, □: C_2.

increases by 30 % while C_2 only increases of 20 %.

C_1 and C_2 are set to their respective minimal values so that the model never overestimates the real subgrid drift vector.

$$C_1 = 0.60 \tag{5.15}$$

$$C_2 = 0.55 \tag{5.16}$$

The fact that the measured values of C_1 and C_2 are always greater than the values imposed implies that the model will always underestimate the real subgrid drift vector. This is not important for small $\overline{\Delta}/\Delta_D$ ratios because the correction is small and has a negligible effect on the bed expansion. But it is more crucial for large values of $\overline{\Delta}/\Delta_D$ where the correction should be sufficient to predict the bed height correctly. Figure 5.4 compares the average of the real subgrid drift tensor and the prediction of the two versions of the gradient model using the values C_1 and C_2 given by Eqs. 5.15 and 5.16. It can be seen that, for large $\overline{\Delta}/\Delta_D$ ratios the average of the second version of the gradient model remains closer to the average of the real subgrid drift vector than the first version.

The density probability function of the vertical correction $C_y = \widetilde{V}_{d,y}/\widetilde{W}_{r,y}$ is shown in Figure 5.5 for the second version of the gradient model, with $C_2 = 0.60$. Their is a very well agreement for small values of Δ_B/Δ_D, but for high ratios the model leads to two many

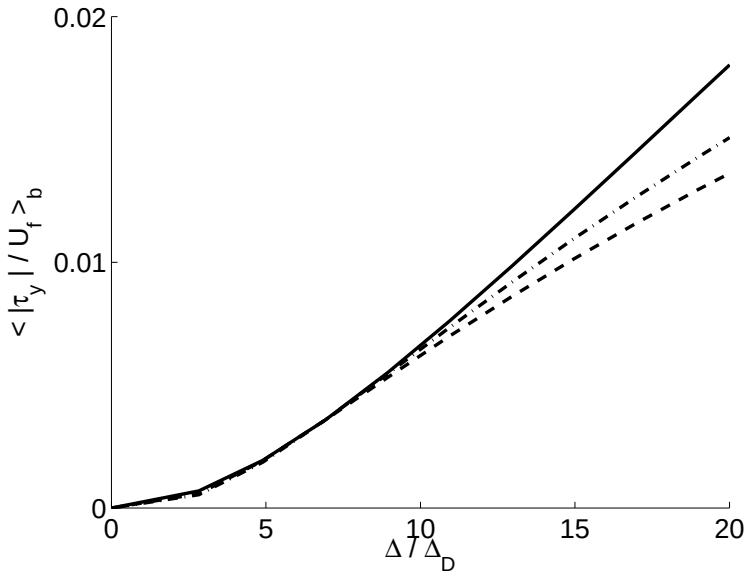

Figure 5.4: Absolute value of the average over the bed of the vertical component of the subgrid drift tensor versus the $\overline{\Delta}/\Delta_D$ ratio. ——— : measured value, - - - : gradient model Eq. 5.10, -·-·- : gradient model Eq. 5.13.

values lower than -1 and not enough between -1 and 0.

5.3.4 A posteriori analysis

The two versions of the model, Eqs. 5.10 and 5.13, are compared on coarse-grid simulations of the test case. Constants C_1 and C_2 are fixed to their minimal values measured during the a priori analysis, Eqs. 5.15 and 5.16. Thus it is assumed that the implicit filter of the simulation is a box filter of width $\overline{\Delta} = \Delta_B = 2\,\Delta_G$, where Δ_G is the mesh size. Figure 5.6 shows the vertical profile of the particle volume fraction in the bed on different meshes. The two versions of the model lead to the right bed height with the 1 mm-mesh size. On the coarser mesh, the second version of the gradient model gives a better result than the first version. This result is consistent with the a priori analysis which has shown that the average of the second version is closer to the real subgrid drift vector than the first version.

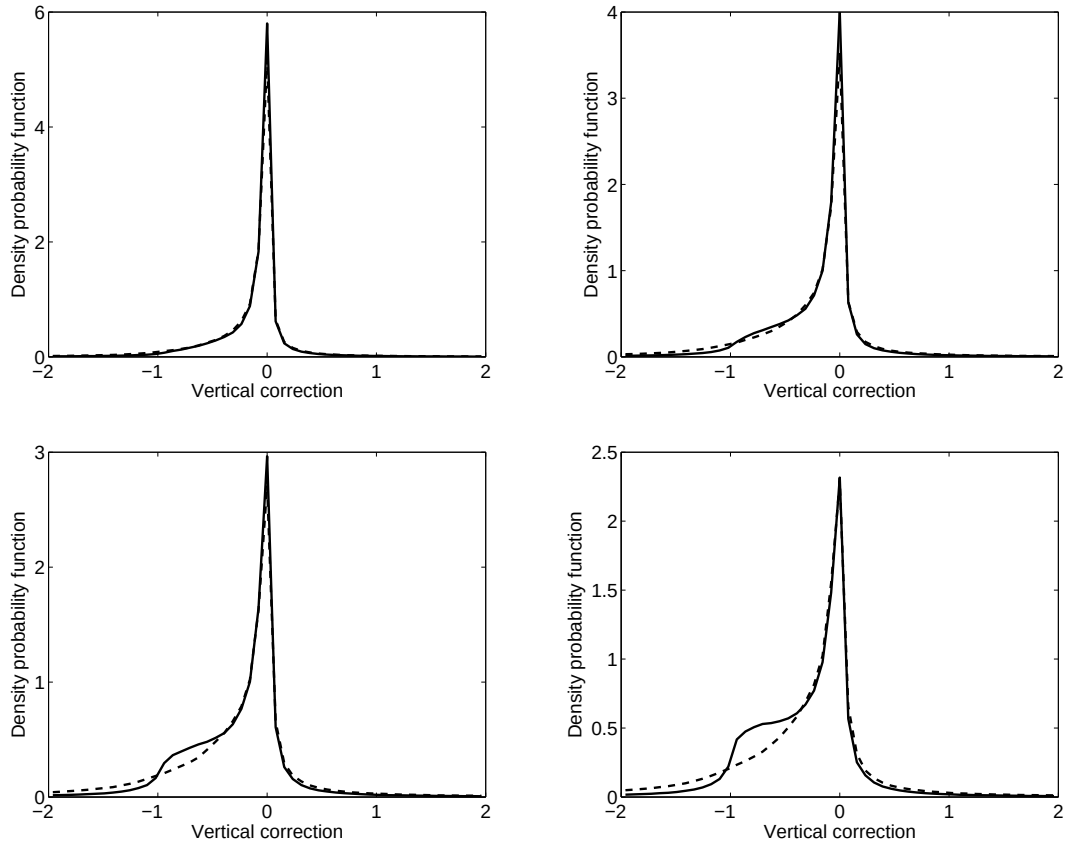

Figure 5.5: Density probability function of the vertical correction of the drag, C_y, for Δ_B/Δ_D equal to 7, 11, 15 and 19. —— : measured values, - - - : second gradient model Eq. 5.13.

5.4 Scale similarity models

5.4.1 Bardina model

The Bardina et al. (1983) model assumes that the subgrid tensor $\tau_{i,j}$ in LES can be approximated by the tensor $\mathcal{L}_{ij}$ in the Germano's decomposition. The application of this hypothesis to the subgrid drift tensor leads to:

$$\tau_i \simeq \mathcal{L}_i \tag{5.17}$$

or, using the expressions of τ_i and $\mathcal{L}_i$:

$$\overline{\alpha_p U_{g,i}} - \overline{\alpha}_p \overline{U}_{g,i} \simeq \overline{\overline{\alpha}_p \widetilde{U}_{g,i}} - \overline{\overline{\alpha}}_p \overline{\widetilde{U}}_{g,i} \tag{5.18}$$

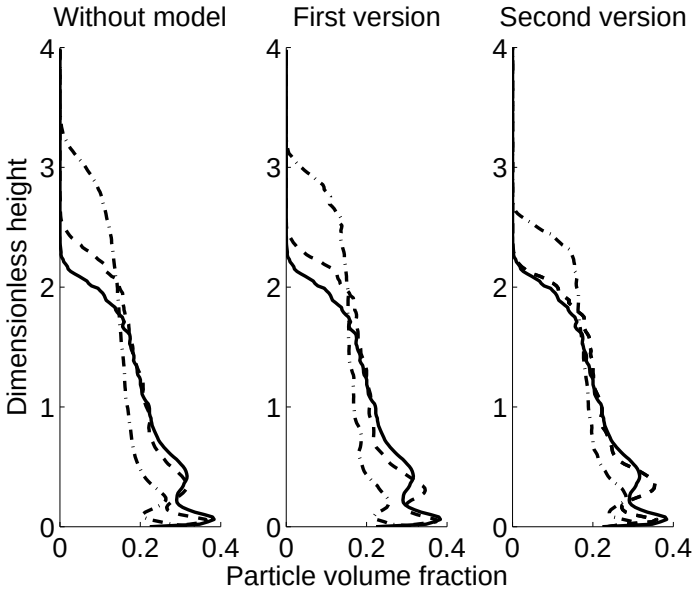

Figure 5.6: Vertical profiles of time averaged particle volume fraction. —— : converged result, - - - : $\Delta_G = 1\ mm$, -·-· : $\Delta_G = 2\ mm$.

A Taylor development shows that this model is equivalent to the Gradient model Eq. 5.8 when the size of the filter tends to zero. This model gives good correlations but, as can be seen in Figure 5.1, it underestimates the average of the subgrid drift tensor. Moreover, it uses a second application of the implicit filter. As it is unknown during a posteriori simulations, this model is useless for us in practice. Nevertheless, Liu et al. (2006) have extended this model to the use of a second filter different from the implicit filter.

5.4.2 Liu-Meneveau-Katz model

The Bardina model uses the same filter a second time. This model is generalized to the application of another filter:

$$\tau_i = C_s \ (\widehat{\overline{\alpha}_p \widetilde{U}_{g,i}} - \widehat{\overline{\alpha}}_p \widehat{\widetilde{U}}_{g,i}) \tag{5.19}$$

where $\widehat{(.)}$ is called the test filter and has a characteristic length scale $\widehat{\Delta} > \overline{\Delta}$, and $C_s > 0$ is the constant of similitude depending on the choice of the second filter and on the implicit filter.

This model will be tested a priori and a posteriori. Due to practical limitations during

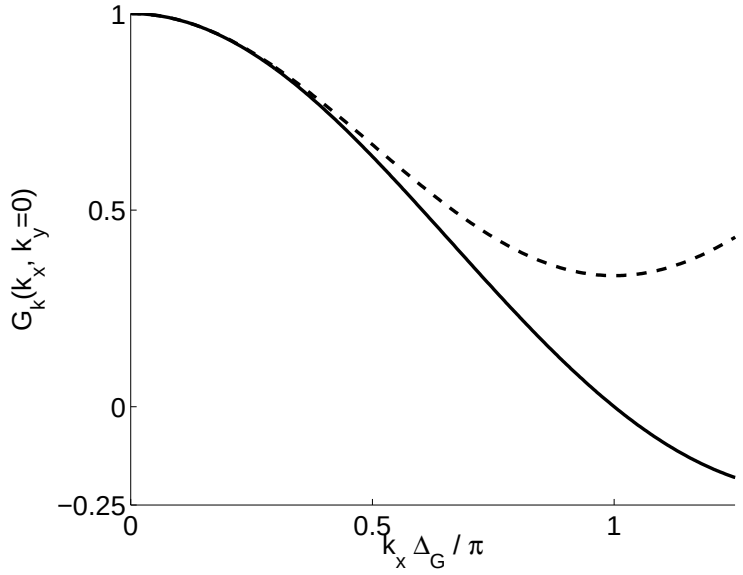

Figure 5.7: Transfer functions. —— : implicit filter, - - - : $\widehat{G}_k$ with $C_f = 1/6$.

the a posteriori simulations, we will focus on test filters defined by:

$$\begin{aligned} \widehat{\phi}(\mathbf{x}) &= (1 - 4\,C_f)\ \phi(\mathbf{x}) \\ &+ C_f\ (\phi(\mathbf{x} + \Delta_G\,\mathbf{e_x}) + \phi(\mathbf{x} - \Delta_G\,\mathbf{e_x})) \\ &+ C_f\ (\phi(\mathbf{x} + \Delta_G\,\mathbf{e_y}) + \phi(\mathbf{x} - \Delta_G\,\mathbf{e_y})) \end{aligned} \tag{5.20}$$

with $C_F > 0$ constants defining the filter. The transfer function associated with the test filter is (Lele, 1992):

$$\widehat{G}_k(k_x, k_y) = (1 - 4\,C_f) + 2\,C_f\,cos(k_x\,\Delta_G) + 2\,C_f\,cos(k_y\,\Delta_G) \tag{5.21}$$

The particular value of $C_f = 1/6$ is choosen so that the test filter is equivalent to the implicit filter when $\mathbf{k}$ tends to zero, *i.e.* a box filter of width $\overline{\Delta} = 2\,\Delta_G$. Figure 5.7 shows $\widehat{G}_k$ for $C_f = 1/6$ and the convolution kernel of the implicit filter. $\widehat{G}_k$ is periodic because the convolution kernel is discrete in physical space. As noted in Section 5.2, the correct average of the subgrid drift vector for $\overline{\Delta} \sim 10\,\Delta_D$ is obtained when $C_s \sim 3/2$.

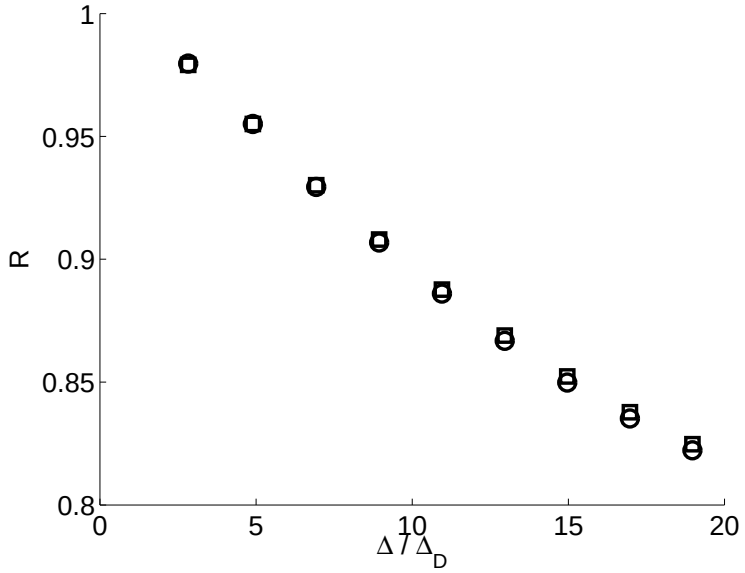

Figure 5.8: Correlation coefficient in function of the $\overline{\Delta}/\Delta_D$ ratio. ◯: LMK model with $C_f = 1/6$. □: second version of the gradient model.

5.4.3 A priori analysis

The LMK model with $C_f = 1/6$ and the second version of the gradient model are compared. Figure 5.8 shows the correlation of the two models for different $\overline{\Delta}/\Delta_D$ ratios. Even for high values, the correlation is greater than 80 % for the two proposed versions while the second version of the gradient model gives slightly greater values.

Figure 5.9 shows the measured values of C_s and C_2 divided by their respective minimal values ($C_{s,min} = 1.71$). It can be seen that C_s increases by more than 22 % while C_2 only increases by 18 %.

Figure 5.10 compares the average of the real subgrid drift tensor and the prediction of the LMK model using the value $C_s = 1.71$. It is shown that, for wide $\overline{\Delta}/\Delta_D$ ratios, the average of the second version of the gradient model remains closer to the average of the real subgrid drift vector than the LMK model.

5.4.4 A posteriori analysis

The LMK model Eq. 5.19 is compared to the second version of the gradient model Eq. 5.13. C_s is fixed to its minimal measured value during the a priori analysis, $C_{s,min} = 1.71$. Figure 5.11 shows the vertical profile of the particle volume fraction in the bed on different meshes. The two models lead to the right bed height with the 1 mm mesh size. On the

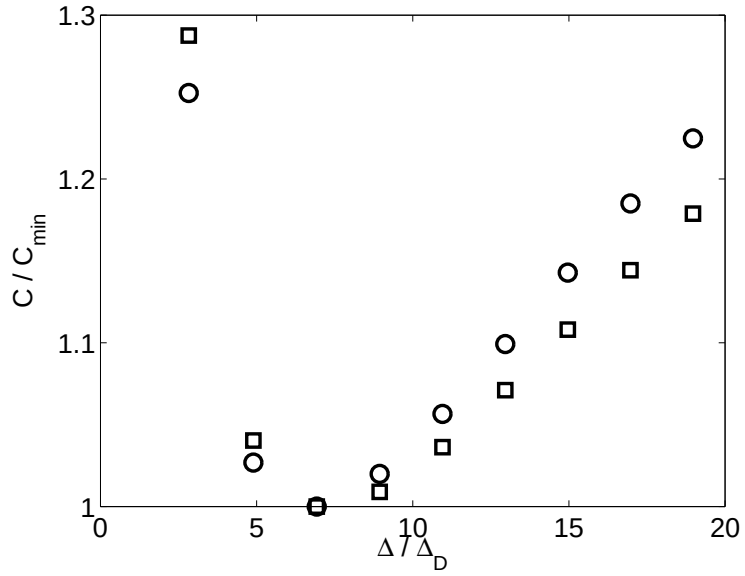

Figure 5.9: C/C_{min} for the LMK model and the second gradient model, as a function of the $\overline{\Delta}/\Delta_D$ ratio. ◯: $C_s/C_{s,min}$, □: $C_2/C_{2,min}$.

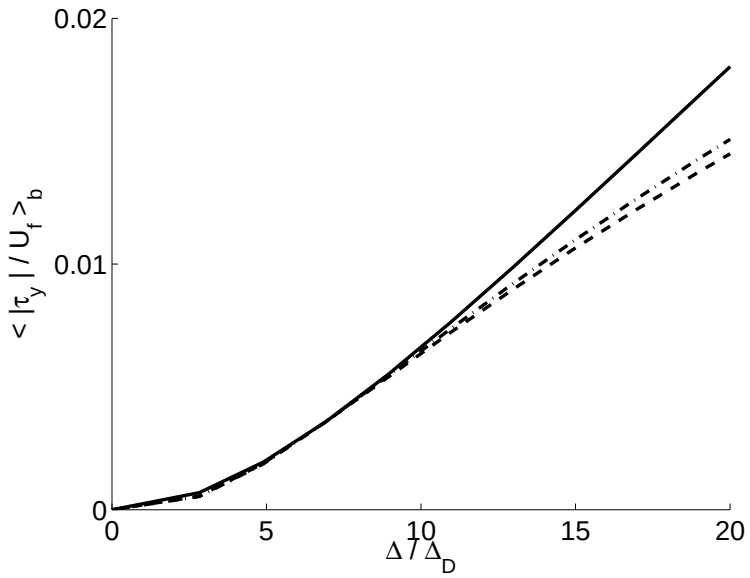

Figure 5.10: Absolute value of the average over the bed of the vertical component of the subgrid drift tensor as a function of the $\overline{\Delta}/\Delta_D$ ratio. ——— : measured value. - - - : LMK model, -·-·- : second version of the gradient model.

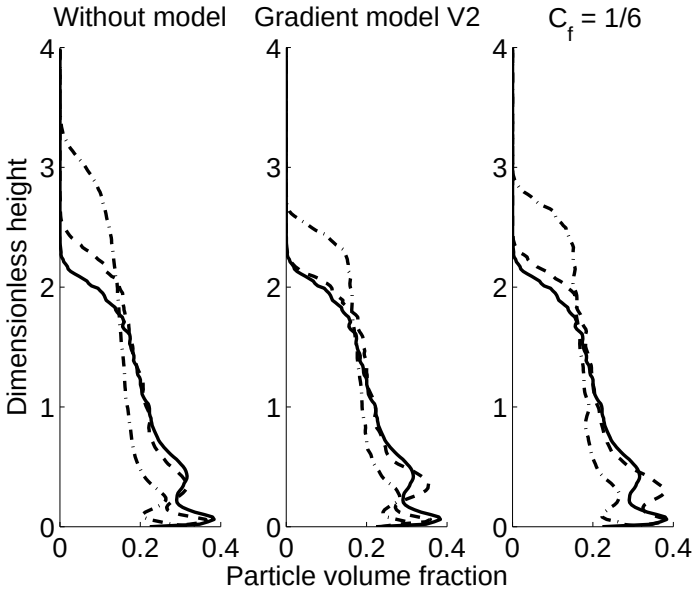

Figure 5.11: Vertical profiles of time averaged particle volume fraction. —— : converged result, - - - : $\Delta_G = 1\ mm$, -·-· : $\Delta_G = 2\ mm$.

coarser mesh, the second version of the gradient model gives a better result than the LMK model. This result is consistent with the a priori that has shown that the average of the second version is closer to the real subgrid drift vector than the LMK model.

5.5 Two-parameter model

5.5.1 Expression

The test filter can be expressed as a function of the second-order Laplacian operator by reorganizing Eq. 5.20:

$$\widehat{\phi} = \phi + C_f\ \Delta_G^2\ \delta^2\phi \tag{5.22}$$

Putting Eq. 5.22 in Eq. 5.19, we obtain the following expression for the LMK model:

$$\begin{aligned} \tau_i &= C_s\, C_f\, \Delta_G^2\ \left(\delta^2(\overline{\alpha}_p \widetilde{U}_{g,i}) - \overline{\alpha}_p\ \delta^2 \widetilde{U}_{g,i} - \widetilde{U}_{g,i}\ \delta^2 \overline{\alpha}_p\right) \\ &- C_s\, C_f^2\, \Delta_G^4\ \delta^2\overline{\alpha}_p\ \delta^2 \widetilde{U}_{g,i} \end{aligned} \tag{5.23}$$

This leads us to propose a two-parameter model:

$$\tau_i = a\ \tau_i^a + b\ \tau_i^b \tag{5.24}$$

with:

$$\tau_i^a = \Delta_G^2 \left(\delta^2(\overline{\alpha}_p \widetilde{U}_{g,i}) - \overline{\alpha}_p \ \delta^2 \widetilde{U}_{g,i} - \widetilde{U}_{g,i} \ \delta^2 \overline{\alpha}_p \right) \tag{5.25}$$

$$\tau_i^b = -\Delta_G^4 \ \delta^2 \overline{\alpha}_p \ \delta^2 \widetilde{U}_{g,i} \tag{5.26}$$

where a and b are the two parameters. When $b = 0$, the second version of the Gradient model Eq. 5.13 is obtained and we have $C_2 = 2\,a$. This two-parameter model differs from the gradient model by the terms of order greater than two.

5.5.2 A priori analysis

The two parameters a and b can be fixed in numerous ways. Let us define ϵ the error by:

$$\epsilon(\overline{\Delta}) = < \left(\tau_i - (a \ \tau_i^a + b \ \tau_i^b) \right)^2 >_{b,t} \tag{5.27}$$

By performing a least square fit on both a and b, ϵ can be minimized. Nevertheless, the average of the measured values and the model prediction are not the same ($< \tau_i >_{b,t} \neq < \ a \ \tau_i^a + b \ \tau_i^b \ >_{b,t}$). As the bed expansion is a direct consequence of this average, this methodology will not be used.

Another value of a and b can be found by first imposing that the model gives the same average as the real subgrid drift vector, which for b leads to:

$$b = \left(< \tau_y > - a \ < \tau_y^a > \right) / < \tau_y^b > \tag{5.28}$$

Then putting Eq. 5.28 in Eq. 5.27, the error is minimized by performing a least square fit on a. Table 5.1 reports the values of a and b found by this method. The associated correlation is also given. Table 5.1 shows that b is positive for small values of $\overline{\Delta}/\Delta_D$ but decreases and becomes negative for $\overline{\Delta}/\Delta_D > 11$, while a remains nearly constant during this time.

The previous methodology provides values of a and b depending on the $\overline{\Delta}/\Delta_D$ ratios. One way to provide a single values of a and b is to perform a least square fit directly on the average of the model, Eq. 5.24. This leads to $a = 0.19$ and $b = -0.31$. As shown in Figure 5.12, the average obtained is very close to the measured one. Nevertheless, these values lead to a poor correlation coefficient, as shown in Figure 5.13.

Intermediate values, $a = 0.27$ and $b = -0.044$, where chosen to provide greater correlation coefficients. This set of parameters is compared to the second gradient model. Figure 5.14 plots the correlation obtained for different $\overline{\Delta}/\Delta_D$ ratios. Even for high values, the correlation is greater than 80 % for the two proposed versions. The second gradient

$\overline{\Delta}/\Delta_D$	a	b	R
6.9	0.28	0.026	0.93
8.9	0.28	0.015	0.91
11	0.29	0.007	0.89
13	0.29	−0.0003	0.87
15	0.30	−0.006	0.85
17	0.31	−0.010	0.84
19	0.32	−0.013	0.82

Table 5.1: Measured values of a and b and the corresponding correlation coefficient R for various values of $\overline{\Delta}/\Delta_D$.

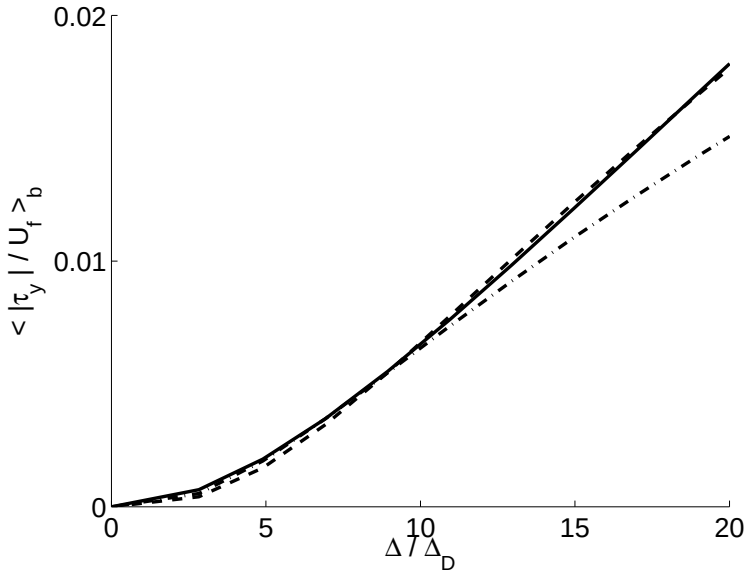

Figure 5.12: Absolute value of the average over the bed of the vertical component of the subgrid drift tensor versus the $\overline{\Delta}/\Delta_D$ ratio. ——— : measured value, - - - : two-parameter model $a = 0.19$, $b = -0.31$, -·-·- : second gradient model.

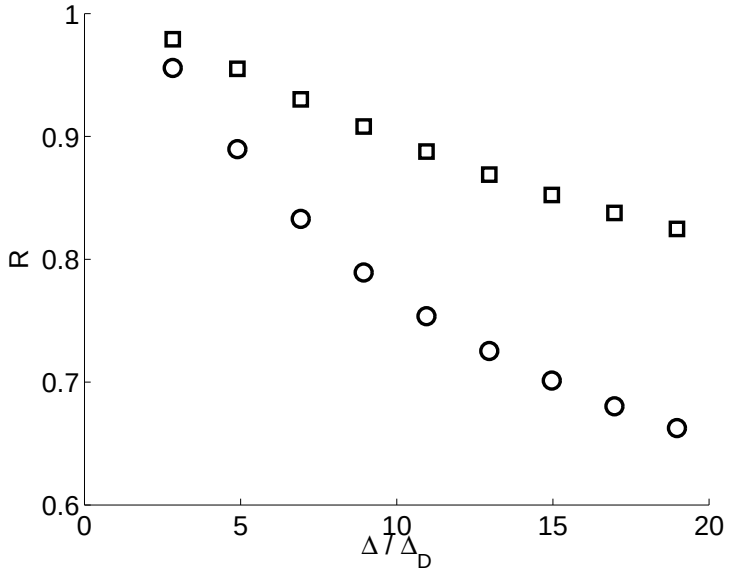

Figure 5.13: Correlation coefficient, as a function of the $\overline{\Delta}/\Delta_D$ ratio. ◯: two-parameter model $a = 0.19$, $b = -0.31$, □: second gradient model.

model gives slightly greater values of the correlation coefficient.

Let us define K as the ratio between the average of the subgrid drift tensor and the average given by the two-parameter model:

$$K = < \tau_y >_{b,t} / < a\ \tau_y^a + b\ \tau_y^b >_{b,t} \tag{5.29}$$

Figure 5.15 plots the measured values of K and C_2 divided by their respective minimal values. It can be seen that K increases by 14 % while C_2 increases by 18 %. a and b were chosen so that the minimal value for K was equal to one.

Figure 5.16 compares the average of the real subgrid drift tensor and the prediction of the two-parameter model with $a = 0.27$ and $b = -0.044$. It shows that for large $\overline{\Delta}/\Delta_D$ ratios the average of the two-parameter model remains closer to the average of the real subgrid drift vector than second gradient model does.

Negatives values of b could be interpreted as LMK models where a deconvolution is substituted to the second filter (see Appendix E). In particular, $a = 0.27$ and $b = -0.044$ leads to $C_f = -1/6$.

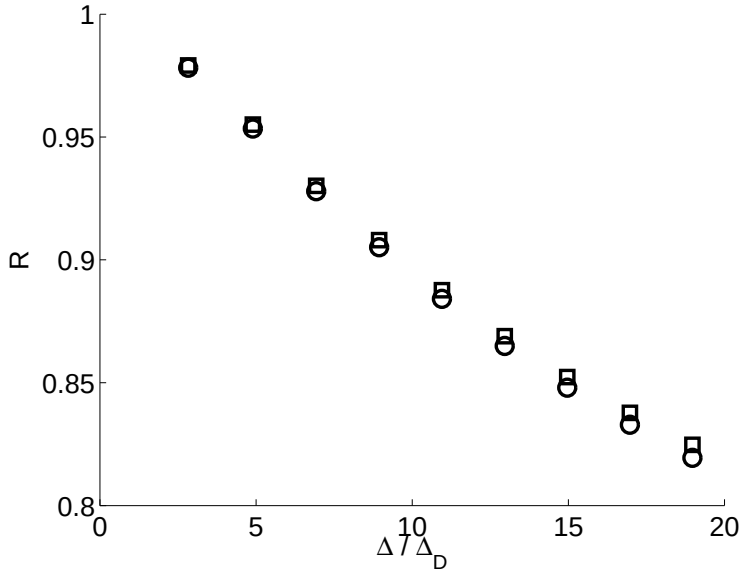

Figure 5.14: Correlation coefficient, as a function of the $\overline{\Delta}/\Delta_D$ ratio. ◯: two-parameter model $a = 0.27$, $b = -0.044$. □: second gradient model.

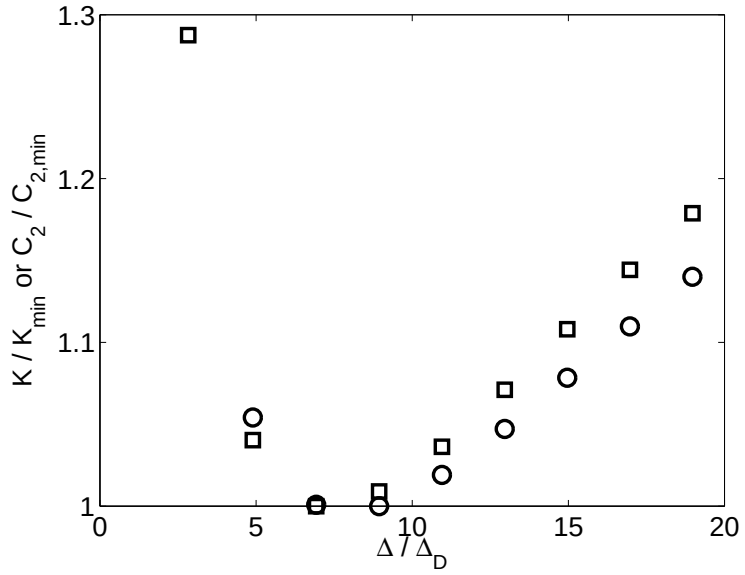

Figure 5.15: Measured values of K/K_{min} and $C_2/C_{2,min}$ as a function of the $\overline{\Delta}/\Delta_D$ ratio. ◯: two-parameter model $a = 0.27$, $b = -0.044$, □: second gradient model.

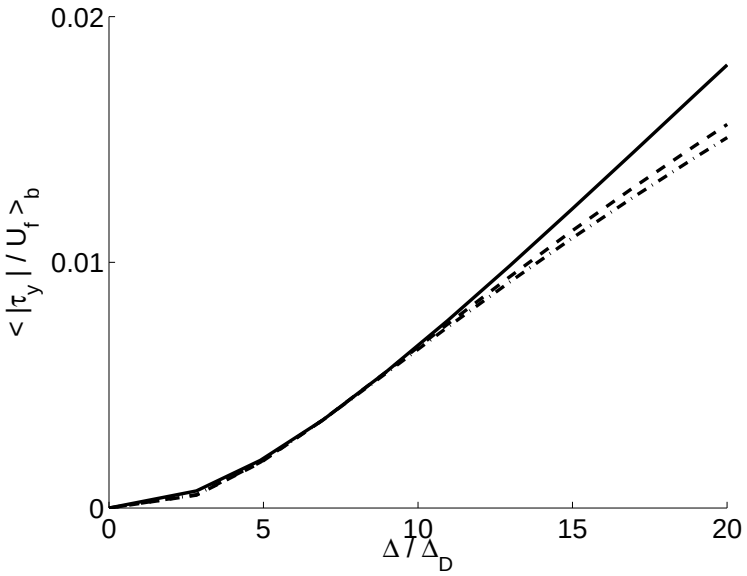

Figure 5.16: Absolute value of the average over the bed of the vertical component of the subgrid drift tensor versus the $\overline{\Delta}/\Delta_D$ ratio. —— : measured value, - - - : two-parameter model $a = 0.27$, $b = -0.044$, -·-·- : second gradient model.

5.5.3 A posteriori analysis

The two-parameter model Eq. 5.24 with $a = 0.27$ and $b = -0.044$ is compared to the second version of the gradient model Eq. 5.13. Figure 5.17 shows the vertical profile of the particle volume fraction in the bed on different meshes. The two models lead to the good bed expansion with the 1 mm-mesh size. On the coarser mesh, the two-parameter model gives a better result than the LMK model. This is coherent with the a priori analysis.

5.6 Conclusion

The application of structural models have been tested with a priori and a posteriori simulations. This kind of models leads to a great correlation coefficient but their application is limited to sufficiently refined meshes. For coarsest meshes, the bed expansion is reduced but remains higher than the converged results. The great advantage is that they are, by construction, applicable in any flow configurations. For instance they could be applicable bubbling beds as well as circulating beds.

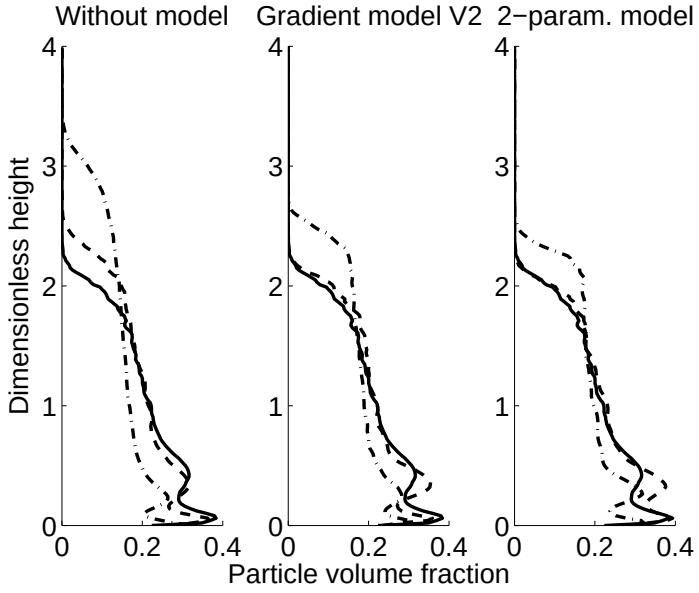

Figure 5.17: Vertical profiles of time averaged particle volume fraction. —— : converged result, - - - : $\Delta_G = 1\ mm$, -·-· : $\Delta_G = 2\ mm$..

Chapter 6

Testing models on a pilot scale

6.1 Introduction

Two models have been proposed in the preceding chapters. In this chapter, we will present the application of the models to the simulation of a laboratory apparatus consisting of a turbulent fluidized bed. This bed covers both the bubbling regime and the circulating regime. Moreover, a drag law specifically developed by TOTAL for their turbulent fluidized bed of Geldart A particles will also be tested. The following sections describe the experimental apparatus, the equations solved, the numerical setup and the results obtained.

6.2 Experimental setup

Experiments were conducted in a 350 mm internal diameter fluidized bed, built with polymethyl methacrylate (PMMA). The bed height is 4.5 mm, as shown in Figure 6.1. Air was injected at the bottom through a perforated plate, with velocities ranging from 0.1 m/s to 0.95 m/s. A cyclone linked to the exit enabled particle reinjection at the bottom of the bed. A second air injection of 100 l/h was added to incoming particles. Ambient air was used, with a pressure and temperature of 1 bar and 20$^{\circ}C$.

Particles were FCC catalyst, with a density of 1400 kg/m^3. Average bulk density was around 850 kg/m^3. Particle size distribution is shown in Figure 6.2 and summed in Table 6.1. The bed was initially filled with 70 kg of particles. Without any gas inlet, about 20% of the particles fall below the gas injection level, leading to a bed height of 70 cm. In the steady state, a fraction of the mass of particles remained in the cyclone and in the dipleg.

The pressure was measured along the wall where particles were injected, at 20 cm,

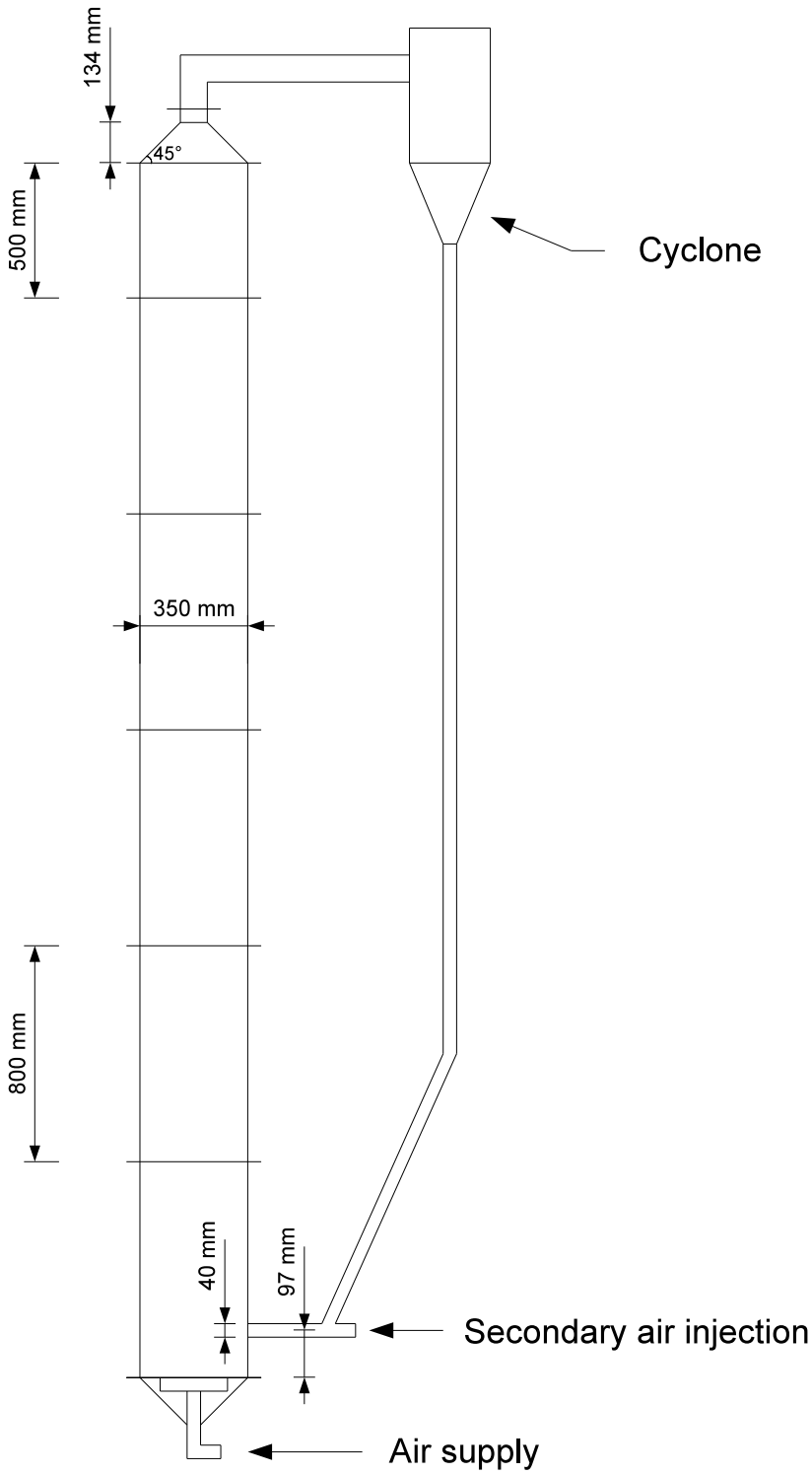

Figure 6.1: Experimental apparatus.

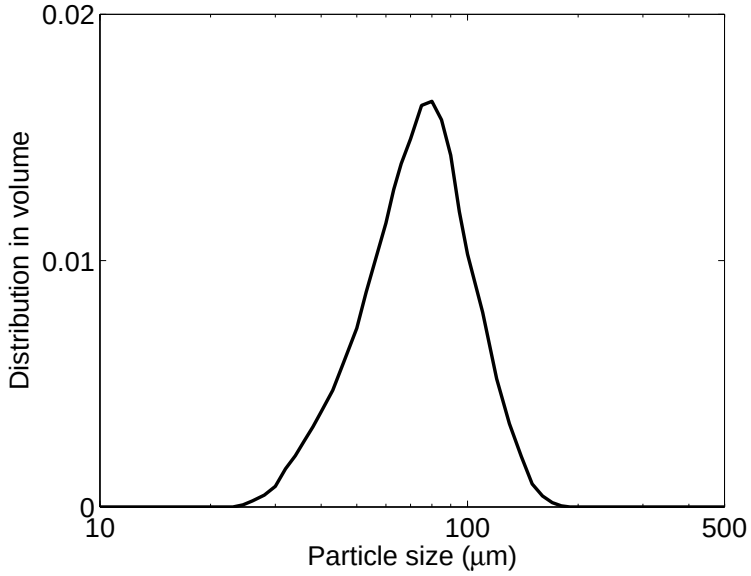

Figure 6.2: Volumetric particle size distribution.

d_{32}	58.78	μm
$d_{50\%}$	71.35	μm
$d_{10\%}$	43.48	μm
$d_{90\%}$	105.6	μm
span	0.871	

Table 6.1: Characteristic of particle size distribution.

60 cm, 100 cm, 140 cm and 4 m from the gas injection point. Solid mass fluxes were measured calculated by temporarily isolating the dipleg of the cyclone and measuring the masse of particles collected over a short period of time.

6.3 Constitutive equations

6.3.1 Two-fluid model

Gas-particle flow is modeled using the two-fluid model, with one particle phase. The constitutive equations used were derived by Balzer et al. (1995) and are given in Appendix A. They consist of the mass and momentum conservation law for each phase and a kinetic particle agitation balance law for the particle phase. The equations are coupled through solid and gas volume fraction and the interfacial momentum transfer. The latter is divided into a buoyancy term and a drag term.

6.3.2 Drag laws

Four drag closure laws will be tested. The first one is the Wen and Yu (1966) closure. Two closures come from the analysis performed in preceding chapters: the functional modelling and the structural modelling. They are corrections to the Wen and Yu (1966) closure that take the inhomogeneity inside a mesh into account. In fact, it is assumed that the equations solved are the filtered two-fluid model equations. The reader is referred to Chapter 3 for more details. Finally, the drag closure developed by TOTAL is also tested.

Wen et Yu law

The drag part of the interfacial momentum transfer is written as:

$$I_{p,i} = \frac{\alpha_p \rho_p}{\tau_p} \left(U_{g,i} - U_{p,i}\right) \tag{6.1}$$

where τ_p is the particle relaxation time given by Wen and Yu (1966):

$$\frac{1}{\tau_p} = \frac{1}{\tau_p^{St}} \left(1 + 0.15 R_e^{0.687}\right) \alpha_g^{-2.7} \tag{6.2}$$

with $R_e = \alpha_g \|\mathbf{U_g} - \mathbf{U_p}\| d_p / \nu_g$ and $\tau_p^{St} = \frac{d_p^2}{18\nu_g} \rho_p / \rho_g$ the Stokes relation time.

TOTAL CReG law

TOTAL CReG has developed a drag law correction especially to predict FCC particles fluidization in their applications. This is a correction of the Gidaspow et al. (1992) closure:

$$I_{p,i}^{CReG} = C(R_e, d_p, \alpha_p)\ I_{p,i}^{Gidaspow} \tag{6.3}$$

where C is an empirical correction.

Functional model

The functional correction to the Wen and Yu law developed in Chapter 4 is tested. It depends both on the size of the mesh and on the particle volume fraction and is written as:

$$I_{p,\alpha} = \frac{\alpha_p \rho_p}{\tau_p}\ (U_{g,\alpha} - U_{p,\alpha})\ \ (1 + f(\Delta_G^*)\ h(\alpha_p)\ K_{\alpha\alpha}) \tag{6.4}$$

where Δ_G^* is the dimensionless mesh size defined by:

$$\Delta_G^* = \sqrt{2}\ \Delta_G\ /\ \Delta_c \tag{6.5}$$

Δ_G is calculated as the cube root of the cell volume and Δ_c is given by:

$$\Delta_c = \sqrt{gD_H}\ \tau_p^{St} \tag{6.6}$$

D_H is the hydraulic diameter. The f and h functions are given by:

$$f(\Delta_G^*) = \frac{{\Delta_G^*}^2}{a^2 + {\Delta_G^*}^2} \tag{6.7}$$

$$h(\alpha_p) = -\sqrt{u}\ (1-u)^2\ (1 - 1.88\ u + 5.16\ u^2) \tag{6.8}$$

where $a = 0.12$ and $u = \alpha_p/\alpha_m$. K_{ij} is a diagonal matrix, the coefficients of which are dynamically calculated as explained in Section 4.2.3.

Structural model

The structural model comes from the mathematical properties of the filtering operation implicitly realized during numerical simulations. It is expressed as:

$$I_{p,i} = \frac{\alpha_p \rho_p}{\tau_p}\ (U_{g,i} - U_{p,i} + V_{d,i}) \tag{6.9}$$

where $\mathbf{V_d}$ is the subgrid drift velocity, calculated by:

$$V_{d,i} = \frac{C_2}{2}\,\Delta_G^2\,\frac{1}{\alpha_p\,\alpha_g}\,\left(\delta^2(\alpha_p U_{g,i}) - \alpha_p\,\delta^2 U_{g,i} - U_{g,i}\,\delta^2\alpha_p\right) \tag{6.10}$$

where $\delta^2\phi$ is a second-order scheme of the Laplacian operator of ϕ, Δ_G is the cube root of the cell volume and $C_2 = 0.55$ is a constant fixed in Chapter 4.

6.4 Simulation setup

6.4.1 Numerical parameters

Numerical simulations were performed with NEPTUNE_CFD V1.07, an unstructured code based on the finite volume method. The quick-upwind method was used for the transport equations. The time step was initially fixed at 10^{-5} s but was adapted during simulation with a maximum Current number of 1, a maximum Fourier of 100 and a maximum CFL of 10. Default options were used. For instance, the precision on the sum of volume fraction was fixed at 10^{-6}.

6.4.2 Physical parameters

The physical properties of the two phases are given in Table 6.2. Only one class of particle was used, with a diameter fixed at the $d_{50\%}$ of the particle size distribution.

Gas phase	density	1.19 $kg \cdot m^{-3}$
	dynamic viscosity	$1.8 \cdot 10^{-5}$ $Pa \cdot s$
Solid phase	diameter	71 μm
	density	1400 $kg \cdot m^{-3}$
	particle-particle restitution coefficient	0.9
	particle-wall restitution coefficient	1.0
	particle-wall friction coefficient	0

Table 6.2: Physical properties of the two phases used in the simulation.

Because of the relative uncertainty of the total mass in the fluidized bed, two initial conditions were used: 70 kg and 57 kg of total mass of particles, as shown in Figure 6.3).

6.4.3 Geometry and boundary conditions

Figure 6.4 shows the geometry of the mesh used to perform simulation. The gas injection was set to be uniform on the surface named "Inlet 1". As the cyclone was not modelled,

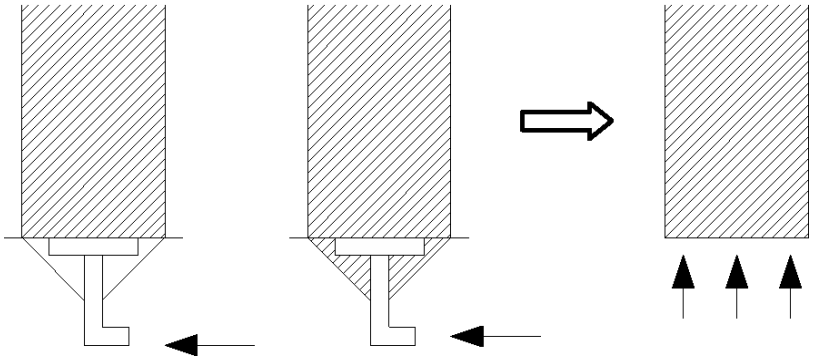

Figure 6.3: Initial conditions. Some particles go below the gas injection and may not be fluidized.

the particles that went through the fluidized bed outlet at each iteration were injected via "Inlet 2" in the next iteration. Particles were assumed to carry an equivalent volume of gas during their injection. Moreover a gas flux of 100 l/h was added. Particle and gas velocity were assumed to be equal and uniform over the injection surface. The boundary conditions are detailed in Table 6.3.

	Inlet 1	**Inlet 2**	**Outlet**	**Wall**
Pressure	extr.P	extr.P	ddP = 0	extr. P
Gas phase	Inlet $\alpha_g = 1$ $U_{g,\perp} = U_f$	Inlet α_g^{E2} $U_{g,\perp}^{E2}$	Outlet $\alpha_g^{in} = 1$	Wall No-slip
Solid phase	Wall Free slip	Input α_p^{E2} $U_{p,\perp}^{E2}$	Oultet $\alpha_p^{in} = 0$	Wall Free slip

Table 6.3: Boundary conditions used during numerical simulations.

Normal velocities $U_{k,\perp}$ at the "Inlet 2" were calculated as a function of U_f, the superficial gas velocity, by:

$$\alpha_p^{E2} = \frac{U_p^{deb}/U_g^{deb}}{1 + U_p^{deb}/U_g^{deb}} \tag{6.11}$$

$$\alpha_g^{E2} = 1 - \alpha_p^{E2} \tag{6.12}$$

$$U_{p,\perp}^{E2} = U_p^{deb} + U_g^{deb} \tag{6.13}$$

$$U_{g,\perp}^{E2} = U_{p,\perp}^{E2} \tag{6.14}$$

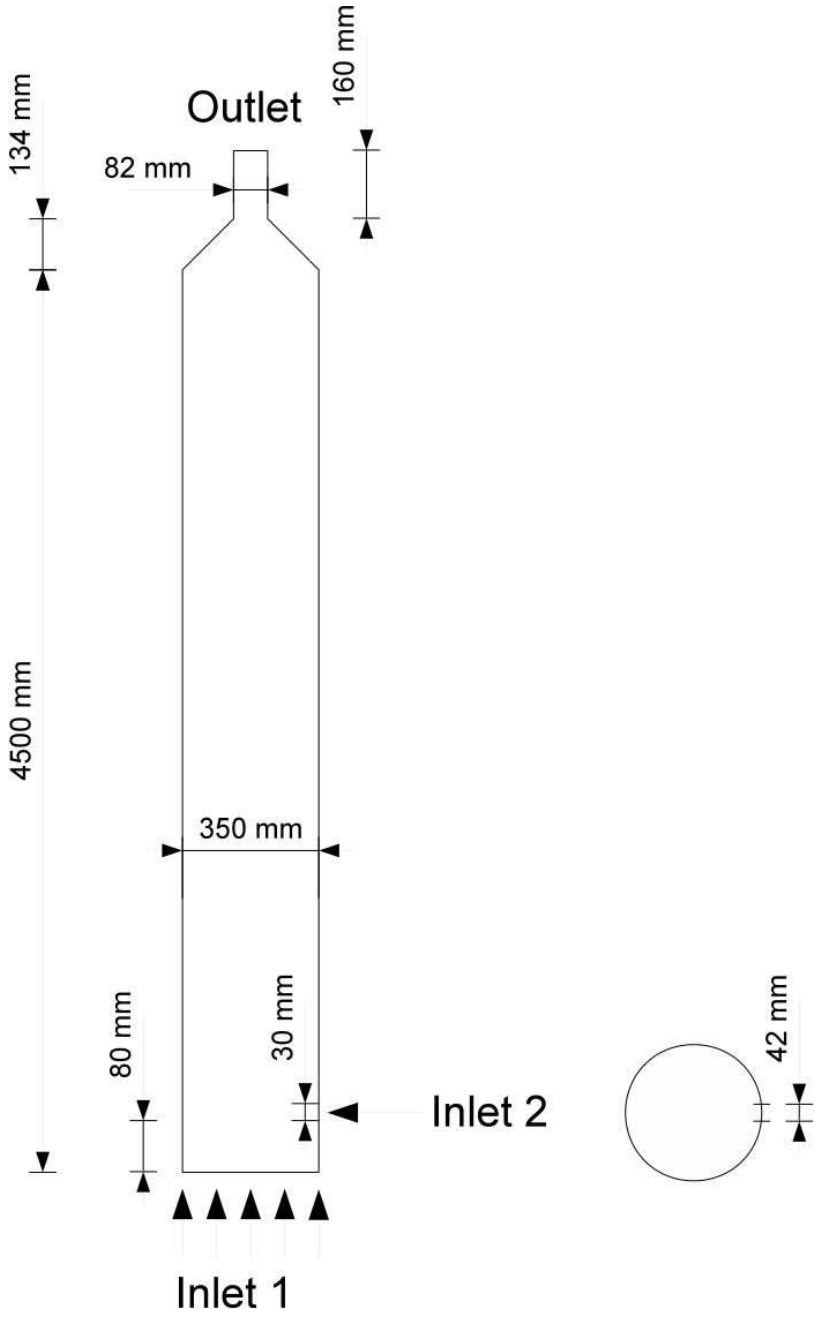

Figure 6.4: Geometry used during numerical simulations.

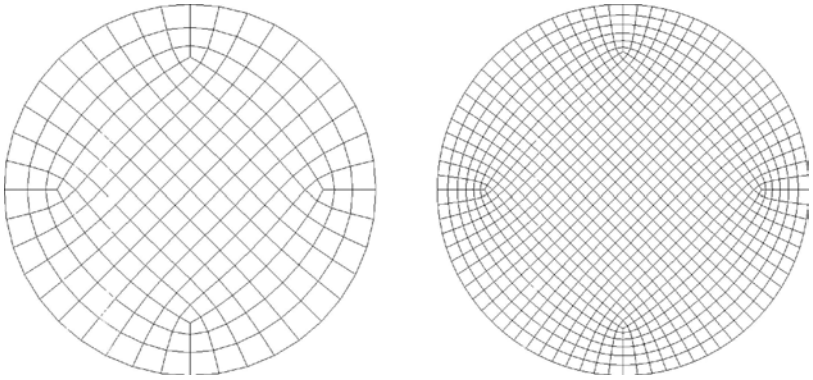

Figure 6.5: O-Grid meshes. From left to right: M0 and M1.

where $U_p^{deb} = Q_p/S_2$, Q_p is the volume flow of particles that goes out of the fluidized bed at the preceding iteration, S_2 the injection surface and $U_g^{deb} = Q_g/S_2$ with $Q_g = Q_p + 100\ l/h$.

6.4.4 Meshes

Two O-Grid meshes were used. Figure 6.5 and Table 6.4 show the mesh characteristics. Cell height was fixed as the average of the square root of the cells' area in the (x, y) plane, leading to nearly cubic cells. An additional finer mesh was used for some of the simulations.

Name	**Mesh number**	**Average Δ_G**
M0	53 020	2 cm
M1	421 520	1 cm

Table 6.4: Meshes characteristics

6.4.5 Simulation runs

Simulations were performed on 4, 48 and 336 cores for the M0, and M1 meshes respectively. Typical simulation time was a few hours for the M0 mesh, and few days for the M1 mesh.

6.5 Results

Three gas velocities were simulated: 0.1 m/s, 0.6 m/s and 0.95 m/s. The first one led to a bubbling fluidized bed while others led to circulating fluidized beds. For each velocity, the

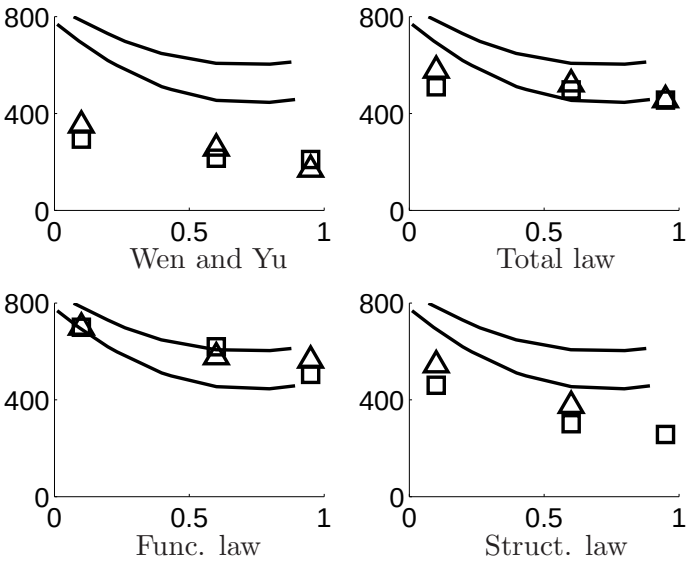

Figure 6.6: Bed density ρ_b in kg/m^3 *vs.* superficial gas velocity in m/s for 70 kg of particles. ——: experimental measurements, □: M0, △: M1.

density inside the bed and the solid mass flux were calculated and compared to experimental results.

6.5.1 Bed density

The bed density was evaluated using pressure sensors along the wall giving the values P_p at $z = 20\ cm$ and $z = 60\ cm$. Bed density ρ_b inside the bed was defined by:

$$\rho_b = -\frac{1}{g}\,\frac{\Delta P}{\Delta z} \tag{6.15}$$

where $\Delta P = P_p(z = 60\ cm) - P_p(z = 20\ cm)$ and $\Delta z = 40\ cm$. Figure 6.6 shows experimental and numerical results obtained with the M0 and M1 meshes and the total solid mass in the bed fixed at 70 kg. The two lines represent different technique of measurements.

The density obtained when using Wen and Yu's drag law without any correction is sensitive to the mesh refinement. Moreover, even with the finest mesh, it is still half the experimental value. Consequently, the bed expansion is considerably overestimated.

At low superficial gas velocity, $U_f = 0.1\ m/s$, Total's drag law leads to an underestimation of the bed density. This depends slightly on mesh refinement. For higher fluidization velocities, their is good agreement with experimental results. Mesh sensitivity decreases

when the fluid velocity increases. For $U_f = 0.95\ m/s$, the measured bed density is independent of the mesh used.

For each superficial gas velocity, the functional model leads to a density in agreement with experimental values. It is independent of the mesh for the lowest superficial gas velocity, i.e. for a bubbling fluidized bed, which the model was developed for. When the fluid velocity increases, the mesh sensitivity increases.

The structural model underestimates the bed density but leads to better results than the Wen and Yu drag law when no correction is added.

6.5.2 Solid mass flux

The solid mass fluxes measured during numerical simulations are given in Tables 6.5 and 6.6. Results vary by a factor of 1 to 1000 among the different drag law closures. The greatest values are obtained when the Wen and Yu drag law without correction was used.

For $U_f = 0.6\ m/s$, the solid mass flux vary by a factor two or more between the M0 and M1 meshes when using the Wen and Yu drag law without correction, the TOTAL drag law or the structural model. It remains constant with the functional model. Experimental mass flux is around 500 kg/h and is obtained only with the structural model on the M1 mesh. The functional drag law underestimates it by a factor 40, the TOTAL drag law overestimates by a factor 2 and Wen and Yu without any correction overestimate by a factor 15.

For $U_f = 0.95\ m/s$, the solid mass flux vary by at least by 40 % between the M0 and M1 meshes for each drag law, except the functional model, where it remains nearly constant. The experimental mass flux is around 3 500 kg/h and is obtained with the TOTAL drag law on the M1 mesh.

	Wen and Yu		**Total**		**Func. model**		**Struct. model**		**Exp.**
U_f (m/s)	**M0**	**M1**	**M0**	**M1**	**M0**	**M1**	**M0**	**M1**	
0.60	18 400	9 000	2 100	1 300	13	13	2 040	640	500
0.95	34 700	21 300	5 400	3 900	190	180	13 000	8 100	3 500

Table 6.5: Solid mass flux in kg/h for 70 kg of particle inside the bed. Experimental measurements are around 500 kg/h for $U_f = 0.6m/s$ and 3 500 kg/h for $U_f = 0.95\ m/s$.

6.5.3 Gas and particle velocity

Figures 6.7 and 6.8 show horizontal profiles of the vertical gas and particle velocities, $U_{g,z}$ and $U_{p,z}$, for $U_f = 0.1\ m/s$ and $U_f = 0.6\ m/s$. In all configurations, vertical gas and

	Wen and Yu		Total		Func. model		Struct. model		Exp.
U_f (m/s)	M0	M1	M0	M1	M0	M1	M0	M1	
0.60	13 900	6 800	2 000	1 100	13	11	1 300	460	500
0.95	25 300		5 500	3 500	160	150	8 100	6 000	3 500

Table 6.6: Solid mass flux in kg/h for 57 kg of particle inside the bed. Experimental measurements are around 500 kg/h for $U_f = 0.6m/s$ and 3500 kg/h for $U_f = 0.95$ m/s.

particle phase velocities are negatives near the walls.

6.5.4 Particle volume fraction

Figures 6.10 and 6.12 show the field of the time averaged particle volume fraction obtained on the M1 mesh with the four drag laws for $U_f = 0.1$ $/s$ and $U_f = 0.6$ m/s. For $U_f = 0.1$ m/s, the Wen and Yu drag law leads to a bed expansion nearly twice that of the other drag laws. For $U_f = 0.6m/s$ a clear separation is found between the dense zone at the bottom and the zone at the top of the bed for the TOTAL drag law and the functional model. For Wen and Yu and the structural model, such a clear separation is not found. Whereas there is a clear separation for the TOTAL drag law, the solids mass flux is greater than with the structural model. The dynamics predicted by the different drag laws are very different, as it can be seen in Figures 6.9 and 6.11, where snapshots of particle volume fraction are shown.

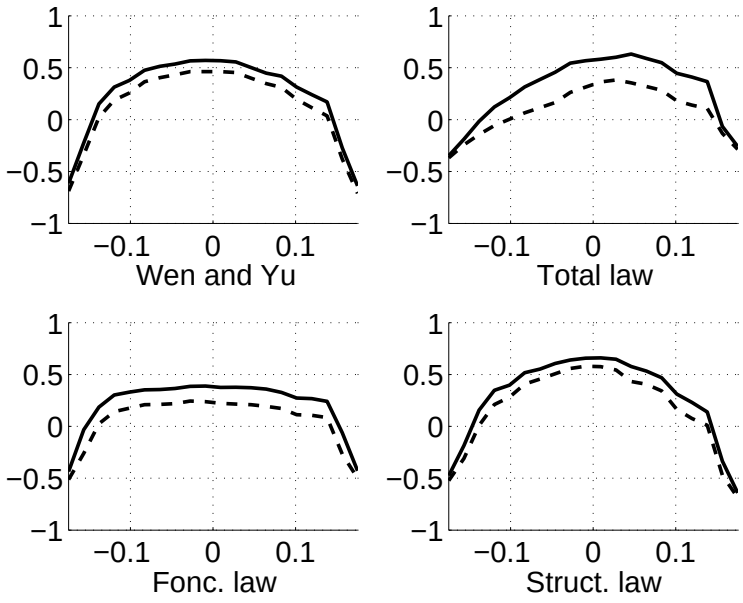

Figure 6.7: Profiles of vertical velocities, at $z = 0.8\ m$ and $y = 0$ for $U_f = 0.1\ m/s$ and 70 kg of particles. —— : $U_{g,z}$, - - - : $U_{p,z}$. Velocities are in m/s and horizontal axe is in m. M1 mesh.

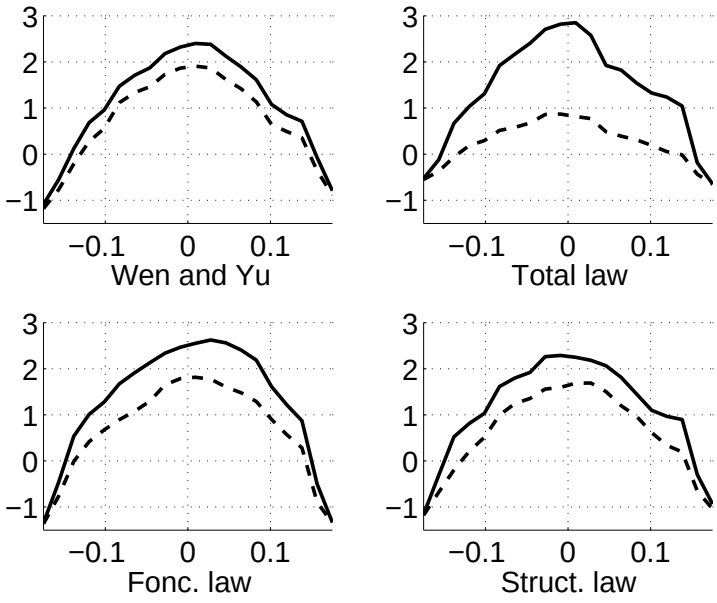

Figure 6.8: Profiles of vertical velocities, at $z = 0.8\ m$ and $y = 0$ for $U_f = 0.6\ m/s$ and 70 kg of particles. —— : $U_{g,z}$, - - - : $U_{p,z}$. Velocities are in m/s and horizontal axe is in m. M1 mesh.

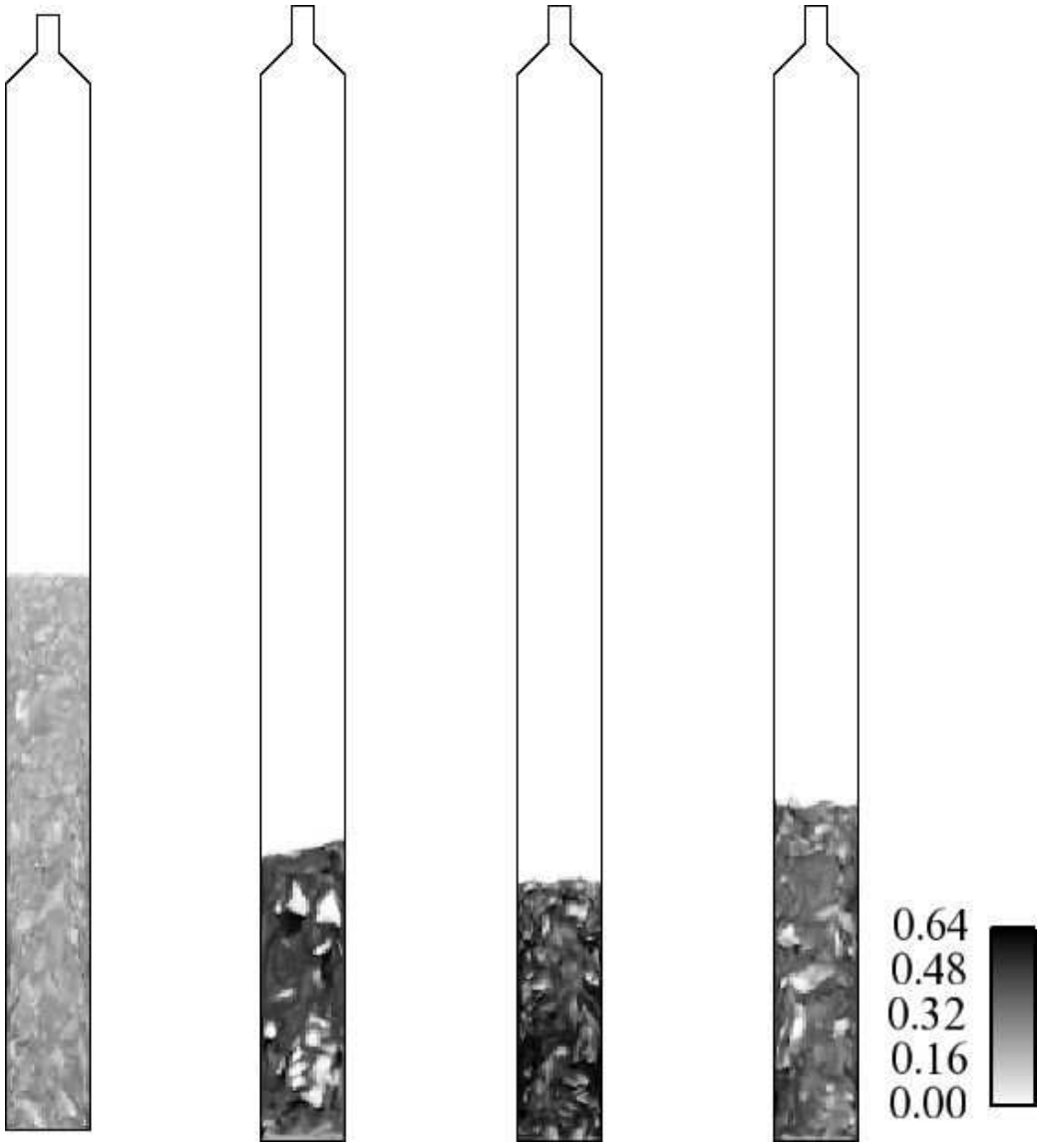

Figure 6.9: Instantaneous particle volume fraction for $U_f = 0.1\ m/s$ on the M1 mesh, with 70 kg of particles. From left to right: Wen and Yu without correction, TOTAL drag law, functional model and structural model.

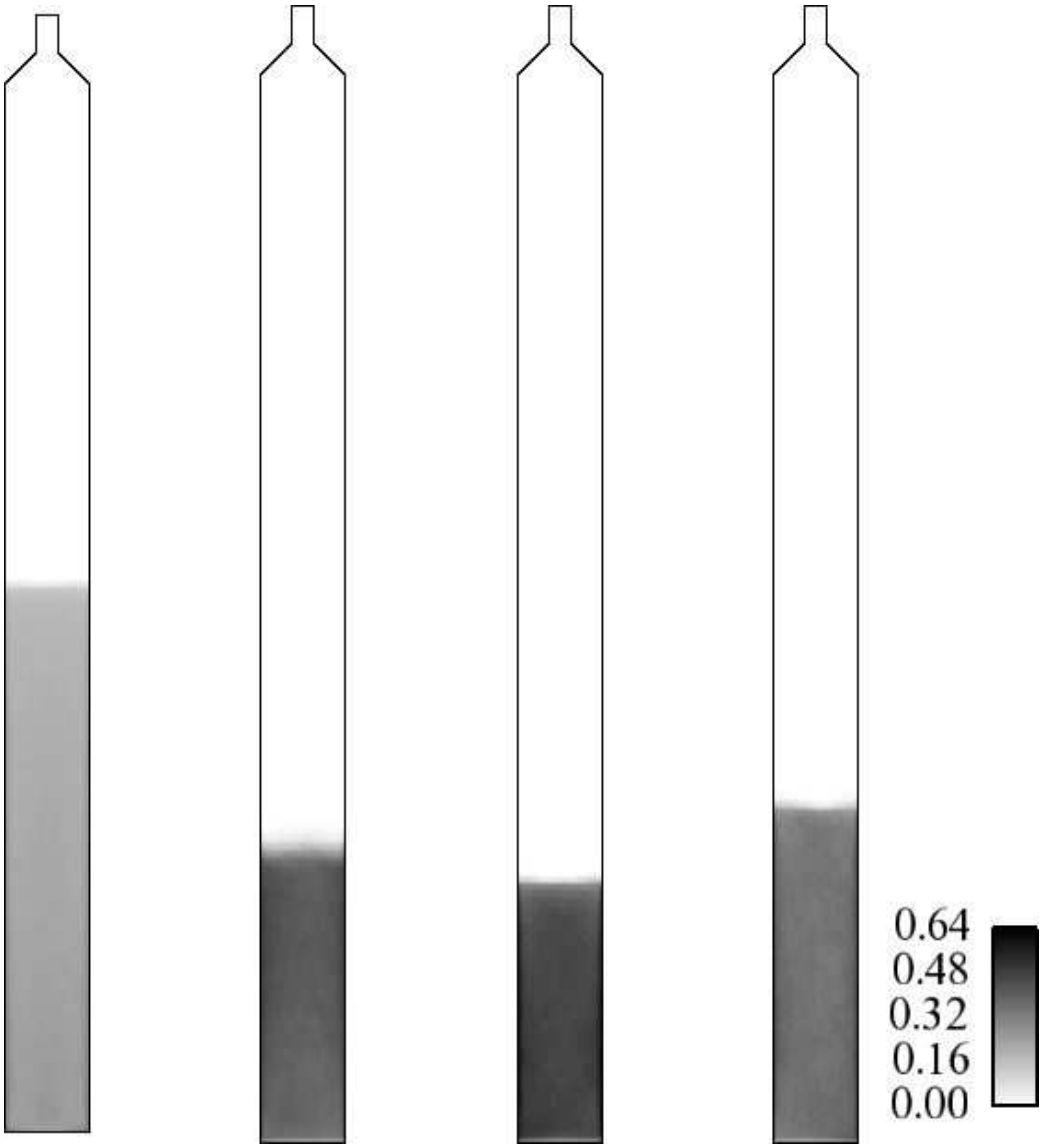

Figure 6.10: Time averaged particle volume fraction for $U_f = 0.1\ m/s$ on the M1 mesh, with 70 kg of particles. From left to right: Wen and Yu without correction, TOTAL drag law, functional model and structural model.

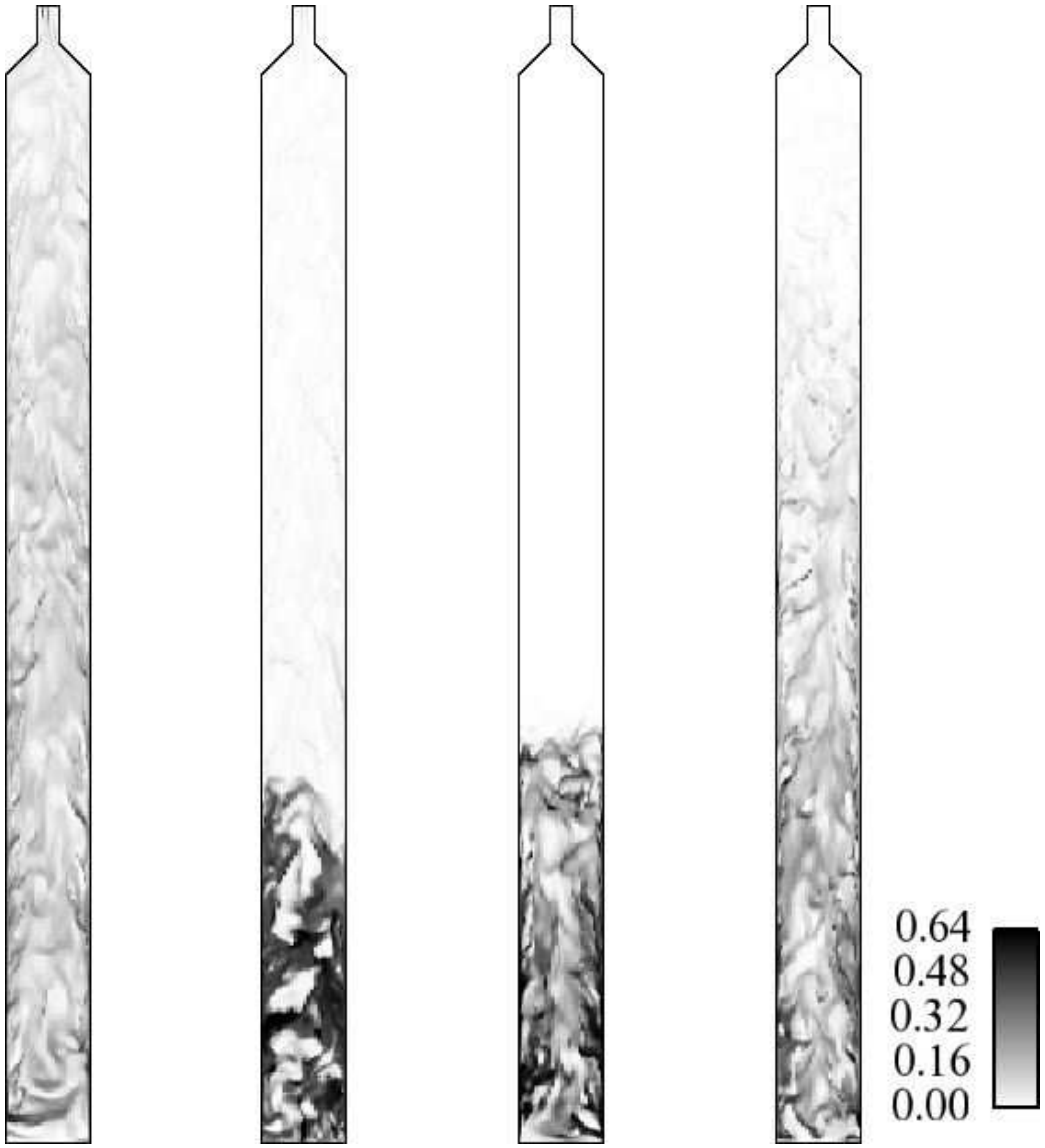

Figure 6.11: Instantaneous particle volume fraction for $U_f = 0.6\ m/s$ on the M1 mesh, with 70 kg of particles. From left to right: Wen and Yu without correction, TOTAL drag law, functional model and structural model.

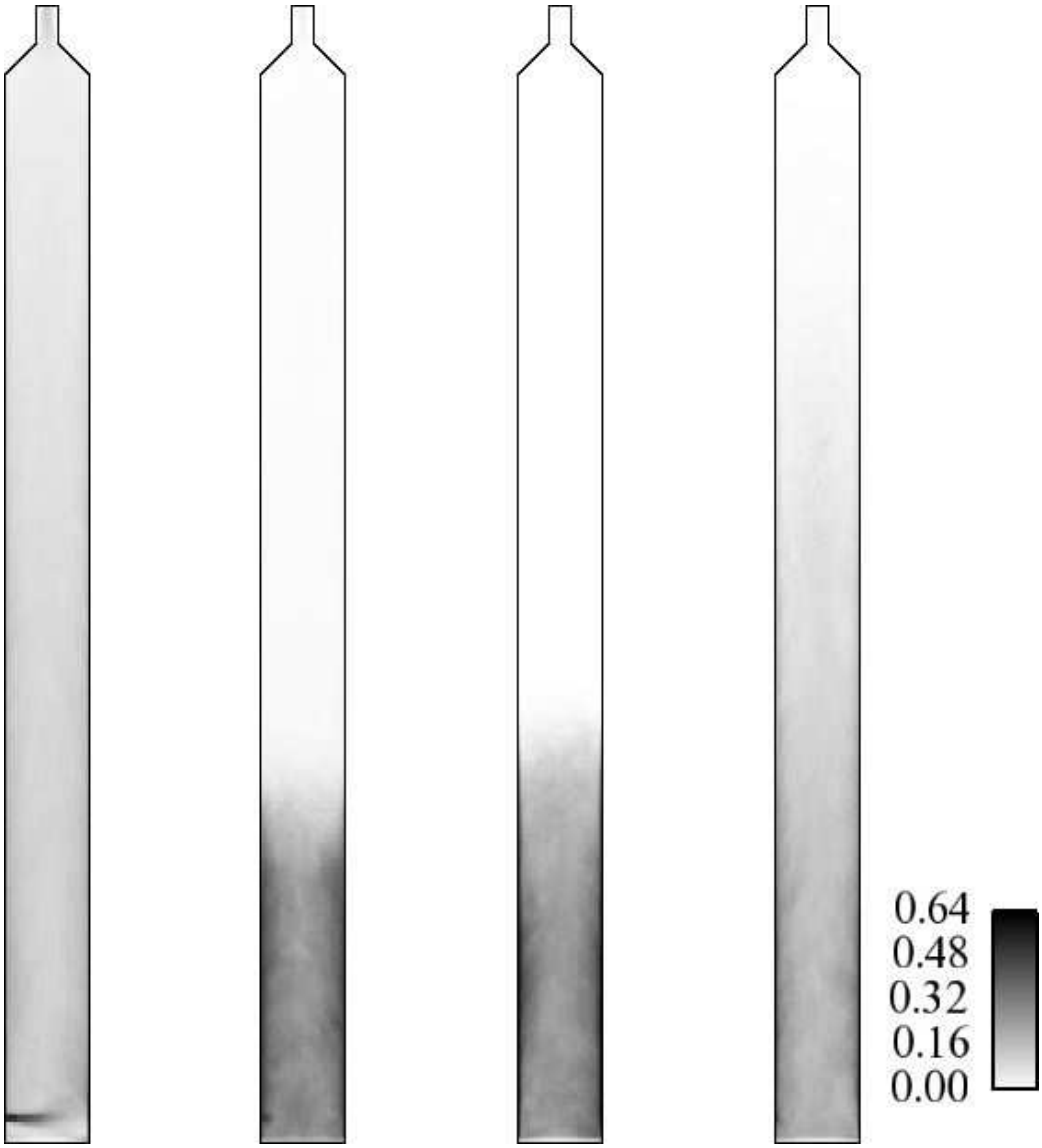

Figure 6.12: Time averaged particle volume fraction for $U_f = 0.6\ m/s$ on the M1 mesh, with 70 kg of particles. From left to right: Wen and Yu without correction, TOTAL drag law, functional model and structural model.

6.6 Conclusion

What should be carefully noted is the mesh sensitivity of the results obtained. As shown in Chapter 3, it is not because good results are obtained with cells of 1 cm width on the pilot scale that such cells will lead to good results at the industrial scale. Only dimensionless numbers ensure that the same results are obtained and, to our knowledge, there is no rule to estimate the mesh needed for a circulating fluidized bed.

Concerning the density within the bed, the functional model leads to mesh-independent results for $U_f = 0.1\ m/s$ and slightly mesh-dependent results for $U_f = 0.6\ m/s$ and $0.95\ m/s$. Moreover, predictions are in agreement with experimental measurements. The TOTAL drag law leads to mesh-independent results for $U_f = 0.95\ m/s$ and slightly dependent ones for $U_f = 0.6\ m/s$ and $0.1\ m/s$. Results are in agreement with experimental data for $U_f \geq 0.6\ m/s$.

Concerning the solid mass flux, results cannot be said to be good. All drag laws give mesh-dependent results. The functional drag law gives a solid mass flux in agreement with the experimental measurements for $U_f = 0.6\ m/s$ on the M1 mesh, but nothing indicates us that this results will still be the same on a finer mesh. The same thing could be said for the TOTAL drag law for $U_f = 0.95\ m/s$.

To conclude, the density is well predicted by the functional model for any superficial gas velocity, and by the TOTAL drag law for $U_f \geq 0.6\ m/s$. A good solid mass flux has been found on the M1 mesh but results on a finer mesh are needed to confirm the agreement that could have been obtained fortuitously.

Chapter 7

Conclusion

7.1 Recapitulation

This thesis was dedicated to the improvements of the two-fluid model used to simulate the fluidization of Geldart A particles. We focused on the strong overestimation of the bed expansion reported in bubbling and turbulent fluidized beds.

The Chapter 2 dealt with the statistical modelling of gas-particle flows. First, in the case of the simple shear flow, collisional terms have been upgraded in order to completely take shear-induced collisions into account. The relevant parameter was found to be:

$$T^* = T \,/\, (\gamma\, a)^2 \tag{7.1}$$

where T is the particle agitation, a is the particle radius and γ is the shear rate. For high values of T^*, collisions are driven by particle agitation and standard collisions models are applicables. In contrast, for law values of T^*, collisions are shear-driven and the two-fluid model failed to predict the correct particle agitation. By adapting the collisional terms as a function of T^*, both high Stokes number flows and low Stokes number flows have been fairly well predicted.

Then, we have looked at the hydrodynamic effects that occur during particle collisions. The model suggested by Legendre et al. (2006), which modify the restitution coefficient of a single particle, have been integrated at the macroscopic scale into the two-fluid model. Restitution coefficient appearing in collisional terms have been modified as a function of:

$$T_\beta = \frac{T}{V_\beta^2} \tag{7.2}$$

where $V_\beta = \frac{\beta}{2}\frac{a}{\tau_p}$ is the characteristic velocity describing the hydrodynamic effect and β a parameter measured by Legendre et al. (2006). Theoretical results have shown a well agreement with discrete particle simulations for low to medium particle concentrations.

Finally, the van der Waals forces have been implemented into the two-fluid model using the BBGKY hierarchy. The consequence is the addition of a cohesive pressure to the particle pressure:

$$P_c = -\alpha_p \rho_p \; \alpha_p g_0^b \; \frac{A}{m_p} \; \frac{1}{2} \; ln\left(\frac{d_p}{z_0}\right) \tag{7.3}$$

where A is the Hamaker constant representing the intensity of the van der Waals forces, z_0 the interatomic distance, m_p the particle mass and g_0^b a function of α_p that behaves like g_0.

None of these physical phenomena have been shown to be a possible explanation to the strong overestimation of the bed height found in numerical simulations. Consequently, the study has been then focus on the practical resolution of the two-fluid model equations, in particular on the effect of using coarse meshes.

In Chapter 3, a dimensional analysis has shown that the mesh convergence is achieved when the dimensionless mesh size Δ_G^* is small, where Δ_G^* is defined by:

$$\Delta_G^* = \frac{\Delta_G}{L} \; \left(\frac{L}{\tau_p^0 \, U_f}\right)^{\frac{1}{2}} \tag{7.4}$$

The filtered formalism has been applied to the two-fluid model equations and the unresolved part of the drag was shown to play a major role in the bed expansion. A correlation analysis has shown that the filtered drag could be expressed by:

$$\overline{\left(\frac{\alpha_p \rho_p}{\tau_p} \, \mathbf{V_r}\right)} = \frac{\overline{\alpha}_p \rho_p}{\widetilde{\tau}_p} \; \left(\widetilde{\mathbf{W}}_\mathbf{r} + \widetilde{\mathbf{V}}_\mathbf{d}\right) \tag{7.5}$$

where $\widetilde{\mathbf{V}}_\mathbf{d}$ is the subgrid drift velocity coming from subgrid inhomogeneities, defined by:

$$\widetilde{\mathbf{V}}_\mathbf{d} \; = \; \widetilde{\mathbf{U}}_{\mathbf{g@p}} - \widetilde{\mathbf{U}}_\mathbf{g} \tag{7.6}$$

where $\widetilde{\mathbf{U}}_{\mathbf{g@p}}$ is the filtered gas velocity seen by the particle phase.

In Chapter 4, we have suggested to close the subgrid drift velocity using a functional model, which assumes that the function of the subgrid drift velocity is to reduce the effective relative velocity. This leads for the filtered drag to:

$$\overline{\left(\frac{\alpha_p \rho_p}{\tau_p} \, V_{r,\alpha}\right)} = \frac{\overline{\alpha}_p \rho_p}{\widetilde{\tau}_p} \left(1 + f(\overline{\Delta}^*) \; h(\overline{\alpha}_p) \; K_{\alpha\alpha}\right) \widetilde{W}_{r,\alpha} \tag{7.7}$$

where $f(\overline{\Delta}^*)$ and $h(\overline{\alpha}_p)$ are closed using highly resolved simulations. $K_{\alpha\alpha}$ are constants adjusted using a dynamic procedure. Results obtained on coarse meshes were compared to fully resolved simulations, and a good agreement was found. Using the developed model, the bed expansion was insensitive to the mesh size.

The Chapter 5 was dedicated to the application of the structural modelling method to close the subgrid drift velocity. In particular, the gradient model has been investigated:

$$\overline{\alpha}_g\,\overline{\alpha}_p\,\widetilde{V}_{d,i} = \; C\,\overline{\Delta}^2\;\frac{\partial\overline{\alpha}_p}{\partial x_j}\;\frac{\partial\widetilde{U}_{g,i}}{\partial x_j} \tag{7.8}$$

A high correlation coefficient has been found and results of coarse-grid simulations were improved. Nevertheless, a sufficient fine mesh is needed.

Finally, in Chapter 6, the two models developed have been tested on an experimental pilot-scale turbulent fluidized bed of FCC particles. Measurements of the density within the bed and solid mass flux were provided by TOTAL, CReG, and have been compared to results obtained with the models developed. The functional model gave the correct bed density and the structural model provided the correct solid mass flux when a sufficiently fine mesh is used.

7.2 Discussion

Modifications of collisional terms taking into account shear-induced collisions were developed in the academic case of the simple shear flow. While results are fairly goods, an extension to realistic flow configurations is needed to make possible the application of these closures to complex geometries.

The hydrodynamic effects that occur during particle collisions have been shown to be negligible in dense gas-solid fluidized beds. However, in liquid-solid fluidized beds, where the particle agitation is lower, these effects may be dominant. A comparison between numerical simulations using the developed models and experimental measurements of particle agitation could be done.

The cohesive pressure found when integrating the van der Waals forces in the two-fluid model could be compared to discrete particle simulations using the soft-sphere model in order to validate its theoretical expression. For instance, a simple shear flow could be used. However, a particular attention should be paid to the decrease law of the potential interaction: the cohesive pressure intensity is proportional its integration over the whole space.

The dimensionless mesh size Δ_G^* was found empirically. As a consequence, its validity

is limited. However, such a law is very useful in order to estimate the mesh size needed to ensure the mesh convergence of numerical results. A generalisation of this law to circulating fluidized beds could be the object of extra studies.

The filtered drag was expressed in the term of a subgrid drift velocity, instead of an effective drag coefficient. We strongly believe that this approach is fruitful and should be considered in further works. For small filter sizes, a square dependence was mathematically proved.

The functional model suggested in Chapter 4 was shown to be efficiency. However, a lot of parameters - as the dependence on the filter size and on the particle volume fraction - were obtained using measures gathered in a particular fluidized bed. Its application is limited to dense fluidized beds, has shown in Chapter 6, where the particle mass flux was strongly underestimated.

The structural modelling is surely a promising approach. While structural models are still restricted to not-too-coarse meshes, the main advantage is their universality. As they are deduced by mathematical analysis, they are applicable to any fluidization regime.

Maybe a useful approach could be to combine the efficiency of functional models with the generality of structural models by using mixed models:

$$mixed\ model = structural\ model + functional\ model \tag{7.9}$$

To our point of view, mixed models should be taken into consideration as a possible solution to the prediction of the filtered drag.

Other terms appearing in the filtered equations have not been investigated in this study. For instance, the unresolved part of the buoyancy force and the Reynolds stress contribution. Structural modelling could be easily applied to these terms and probably good results could be obtained.

Appendix A

Two-Fluid Model Equations

The model is based on separate equations of mass and momentum for the gas phase and on mass, momentum and kinetic agitation for the particle phase. Equations are coupled through gas and particle volume fraction and inter-phase momentum transfer terms. In the following, subscript k = g refers to the gas phase and k = p to the particle phase. The following equations were derived by Balzer et al. (1995).

Gas and particle volume fraction, α_g and α_p have to satisfy:

$$\alpha_g + \alpha_p = 1 \tag{A.1}$$

Mass transport equation:

$$\frac{\partial}{\partial t}(\alpha_k \rho_k) + \frac{\partial}{\partial x_i}(\alpha_k \rho_k U_{k,i}) = 0 \tag{A.2}$$

with ρ_k density of the k phase and $U_{k,i}$ the i-component of its velocity .

Momentum transport equation:

$$\begin{aligned} \alpha_k \rho_k \left(\frac{\partial U_{k,i}}{\partial t} + U_{k,j} \frac{\partial U_{k,i}}{\partial x_j} \right) &= -\alpha_k \frac{\partial P_g}{\partial x_i} + \alpha_k \rho_k g_i \\ &+ I_{k,i} + \frac{\partial}{\partial x_j} \Sigma_{k,ij} \end{aligned} \tag{A.3}$$

with P_g the mean gas pressure, g_i the gravity i-component, $I_{k,i}$ the inter-phase momentum transfer without the mean gas pressure contribution, $I_{g,i} = -I_{p,i}$, and $\Sigma_{k,ij}$ the effective stress tensor of the phase k. For $k = g$, it is equal to the laminar viscous stress tensor. The

stress tensor for the particular phase is closed using a Boussinesq hypothesis:

$$\begin{aligned}\Sigma_{p,ij} &= \left(P_p - \lambda_p \frac{\partial U_{p,m}}{\partial x_m}\right)\delta_{ij} \\ &- \mu_p\left(\frac{\partial U_{p,i}}{\partial x_j} + \frac{\partial U_{p,j}}{\partial x_i} - \frac{2}{3}\frac{\partial U_{p,m}}{\partial x_m}\ \delta_{ij}\right)\end{aligned} \tag{A.4}$$

with P_p the particular pressure, $\mu_p = \alpha_p \rho_p\ (\nu_p^{kin} + \nu_p^{coll})$ the shear particular viscosity and λ_p the volume particular viscosity. P_p, ν_p^{kin}, ν_p^{coll} and λ_p are given by:

$$P_p = \frac{2}{3}\ \alpha_p \rho_p\ q_p^2\ (1 + 2\alpha_p g_0\ (1 + e_c)) \tag{A.5}$$

$$\lambda_p = \frac{4}{3}\ \alpha_p \rho_p\ \alpha_p g_0\ d_p\ (1 + e_c)\ \sqrt{\frac{2\, q_p^2}{3\,\pi}} \tag{A.6}$$

$$\nu_p^{kin} = \frac{1}{2}\ \tau_p\ T\ (1 + \alpha_p g_0\, \phi_c)\ (1 + \frac{\sigma_c}{2}\ \frac{\tau_p}{\tau_c})^{-1} \tag{A.7}$$

$$\nu_p^{coll} = \frac{4}{5}\ \alpha_p g_0\ (1 + e_c)\ (\nu_p^{kin} + d_p \sqrt{\frac{2}{3}\frac{q_p^2}{\pi}}) \tag{A.8}$$

with e_c particles elasticity coefficient, $\sigma_c = (1+e_c)(3-e_c)/5$ and $\phi_c = 2/5\ (1+e_c)(3e_c-1)$. τ_p is the particle relaxation time given by the drag law. The inter-particle collisions time τ_c is given by:

$$\frac{1}{\tau_c} = 24\ \frac{\alpha_p g_0}{d_p}\ \sqrt{\frac{2}{3}\frac{q_p^2}{\pi}} \tag{A.9}$$

The pair correlation function g_0 reflects the increase of the probability to find a particle at contact due to the close packing of particles. Lun and Savage (1986) give the following expression:

$$g_0 = \left(1 - \frac{\alpha_p}{\alpha_m}\right)^{-2.5\alpha_m} \tag{A.10}$$

which tends to infinity when the particle volume fraction α_p tends to $\alpha_m = 0.64$, the maximum solid fraction. The particle random kinetic energy q_p^2 - or so-called "granular temperature" -obeys the following transport equation which is derived from the particle pdf Boltzman-like equation:

$$\alpha_p \rho_p \left(\frac{\partial q_p^2}{\partial t} + U_{p,j}\frac{\partial q_p^2}{\partial x_j}\right) = \frac{\partial}{\partial x_j}\left(\alpha_p \rho_p (K_p^{kin} + K_p^{coll})\frac{\partial q_p^2}{\partial x_i}\right)$$

$$
\begin{aligned}
- \quad & \Sigma_{p,ij} \frac{\partial U_{p,i}}{\partial x_j} - 2 \, \frac{\alpha_p \rho_p}{\tau_p} \, q_p^2 \\
- \quad & \frac{1}{2}(1 - e_c^2) \, \frac{\alpha_p \rho_p}{\tau_c} \, \frac{2}{3} q_p^2
\end{aligned} \tag{A.11}
$$

with K_p^{kin} and K_p^{coll} the kinematic and collisional diffusivity respectively, given by:

$$
K_p^{kin} = \frac{2}{3} \, q_p^2 \tau_c \, (1 + \alpha_p g_0 \varphi_c)(\xi_c + \frac{9}{5} \frac{\tau_c}{\tau_p})^{-1} \tag{A.12}
$$

$$
K_p^{coll} = \frac{6}{5} \, \alpha_p g_0 \, (1 + e_c) \, (K_p^{kin} + \frac{10}{9} \, d_p \sqrt{\frac{2}{3} \frac{q_p^2}{\pi}}) \tag{A.13}
$$

with $\xi_c = (1 + e_c)(49 - 33e_c)/100$ and $\varphi_c = 3/5(1 + e_c)^2(2e_c - 1)$. The interface momentum transfert $I_{k,i}$ can be written as:

$$
I_{p,i} = \frac{\alpha_p \rho_p}{\tau_p} (U_{g,i} - U_{p,i}) \tag{A.14}
$$

with τ_p the particle relaxation time given by the Wen and Yu (1966) correlation:

$$
\frac{1}{\tau_p} = \frac{1}{\tau_p^{St}} \left(1 + 0.15 R_e^{0.687}\right) \alpha_g^{-2.7} \tag{A.15}
$$

with $R_e = \alpha_g \| \mathbf{U_g} - \mathbf{U_p} \| d_p / \nu_g$ and $\tau_p^{St} = \rho_p d_p^2 / (18 \mu_g)$ the Stokes drag time of an isolated spherical particle in the gas.

Appendix B

Unified theory

B.1 Coefficients definitions

$$f_{n,p}(u) = \int_u^{+\infty} (x-u)^n \; x^p \; e^{-x^2} dx \tag{B.1}$$

$f_{n,p}$ functions can be expressed with known functions (erf, exp, ...). I_n are defined by:

$$I_n = \int_0^{+\infty} x^n \; e^{-x^2} dx \tag{B.2}$$

$A_{n,p}$, $B_{n,p}$ and $D_{n,p}$ functions are defined b:

$$A_{n,p}(T^*) = \frac{1}{4\pi I_{n+p}} \int_{\mathbf{k}} f_{n,p}\left(\frac{k_x\, k_z}{\sqrt{T^*}}\right) \mathbf{dk} \tag{B.3}$$

$$B_{n,p}(T^*) = -\frac{15}{4\pi n I_{n+p-1}} \sqrt{T^*} \int_{\mathbf{k}} f_{n,p}\left(\frac{k_x\, k_z}{\sqrt{T^*}}\right) (k_x\, k_z) \mathbf{dk} \tag{B.4}$$

$$D_{n,p}(T^*) = \frac{3}{4\pi I_{n+p}} \int_{\mathbf{k}} f_{n,p}\left(\frac{k_x\, k_z}{\sqrt{T^*}}\right) k_z^2 \mathbf{dk} \tag{B.5}$$

where $T^* = T/(\gamma^2 a^2)$ is the dimensionless granular temperature.

B.2 Asymptotic behaviour

The Taylor development of $f_{n,p}$ around zero is:

$$f_{n,p}(u) = I_{n+p} - u \; n \; I_{n+p-1} + O(u^2) \tag{B.6}$$

$A_{n,p}$, $B_{n,p}$, and $D_{n,p}$ are build to tend to one when T^* goes to infinity. When T^* goes to zero, they are equivalent to:

$$A_{n,0} \sim_0 \frac{1}{T^{*n/2}} \times \frac{(-1)^n}{4\sqrt{\pi}\, I_n} \int_{kx\, kz<0} (k_x\, k_z)^n \ \mathbf{dk} \tag{B.7}$$

$$B_{n,0} \sim_0 \frac{(-1)^{n+1}}{T^{*(n-1)/2}} \times \frac{15}{4\sqrt{\pi}\, n I_{n-1}} \int_{kx\, kz<0} (k_x\, k_z)^{n+1} \ \mathbf{dk} \tag{B.8}$$

$$D_{n,0} \sim_0 \frac{1}{T^{*n/2}} \times \frac{3\cdot(-1)^n}{4\sqrt{\pi}\, I_n} \int_{kx\, kz<0} (k_x\, k_z)^n\, k_z^2 \ \mathbf{dk} \tag{B.9}$$

$$D_{2,1} \sim_0 \frac{4}{5\sqrt{\pi T^*}} \tag{B.10}$$

Using a formal calculation software, it can be shown that:

$$B_{3,0} = 1 + \frac{2}{21T^*} \tag{B.11}$$

$$B_{2,1} = 1 \tag{B.12}$$

B.3 Collisional terms of the unified theory

$$\begin{aligned} C_{ii} &= -(1-e_c^2)\ \frac{\alpha_p\rho_p}{\tau_c}\ T\ A_{3,0} \\ &+ 2\gamma\ \frac{4}{5}\ \alpha_p\rho_p\ \alpha_p g_0\ (1+e_c)\ (\gamma\, d_p\sqrt{\frac{T}{\pi}}\ B_{2,0} - \widehat{R}_{p,13}) \end{aligned} \tag{B.13}$$

$$\begin{aligned} C_{33} &= (1+e_c)\ \frac{\alpha_p\rho_p}{3\tau_c}\ T\ ((1+e_c)\ D_{3,0} - 2\ D_{2,1}) \\ &- \frac{1}{5}\ (1+e_c)(3-e_c)\ \frac{\alpha_p\rho_p}{\tau_c}\ \widehat{R}_{p,33} \end{aligned} \tag{B.14}$$

$$\begin{aligned} C_{13} &= -\frac{2}{5}\ \alpha_p\rho_p\ \alpha_p g_0(1+e_c)\ T\gamma\ (3(1+e_c)\ B_{3,0} - 4) \\ &- \frac{1}{5}\ (1+e_c)(3-e_c)\ \frac{\alpha_p\rho_p}{\tau_c}\ \widehat{R}_{p,13} \\ &- \gamma\ \frac{4}{5}\ \alpha_p\rho_p\ \alpha_p g_0\ (1+e_c)\ \widehat{R}_{p,33} \end{aligned} \tag{B.15}$$

Appendix C

Hydrodynamic effects

In the framework proposed by Jenkins and Richman (1985), the collisional terms can be written as:

$$C(\Psi) = \chi(\Psi) - \frac{\partial}{\partial x_j}\Theta_j(\Psi) \tag{C.1}$$

$\chi(\Psi)$ and $\theta_k(\Psi)$ are defined by:

$$\begin{aligned} \chi(\Psi) &= 2\ a^2 g_0 \int\int\int_{\mathbf{g}.\mathbf{k}>0} \Delta(\Psi)\ f(\mathbf{c_1},\mathbf{x}) f(\mathbf{c_2},\mathbf{x}) \\ &\times \left(1 + a\ k_i \frac{\partial}{\partial x_i} ln\left(\frac{f(\mathbf{c_2},\mathbf{x})}{f(\mathbf{c_1},\mathbf{x})}\right)\right)(\mathbf{g}\cdot\mathbf{k})\, d\mathbf{k}\ d\mathbf{c_1} d\mathbf{c_2} \end{aligned} \tag{C.2}$$

$$\begin{aligned} \Theta_j(\Psi) &= -4\ a^3 g_0 \int\int\int_{\mathbf{g}.\mathbf{k}>0} \delta(\Psi_1)\ f(\mathbf{c_1},\mathbf{x}) f(\mathbf{c_2},\mathbf{x}) \\ &\times \left(1 + a\ k_i \frac{\partial}{\partial x_i} ln\left(\frac{f(\mathbf{c_2},\mathbf{x})}{f(\mathbf{c_1},\mathbf{x})}\right)\right)(\mathbf{g}\cdot\mathbf{k})\, k_j\ d\mathbf{k}\ d\mathbf{c_1} d\mathbf{c_2} \end{aligned} \tag{C.3}$$

with $\Delta(\Psi)$ the variation of Ψ during the collision of two particles and $\delta(\Psi_1)$ the variation of Ψ for the particle of velocity $\mathbf{c_1}$.

Then, χ_{ij} and Θ_{ij} are defined by:

$$\chi_{ij} = \chi(m_p c_i c_j) \tag{C.4}$$

$$\Theta_{ij} = \Theta_j(m_p c_i) \tag{C.5}$$

Based on the simple laws for a binary collision, we obtain:

$$\delta(m_p\ \mathbf{c_1}) = -\frac{1}{2}\ (1+e_{pp})\ \ (\mathbf{g}\cdot\mathbf{k})\ \ \mathbf{k} \tag{C.6}$$

$$\Delta(m_p\ c_i\ c_i) = \frac{1}{2}\ (1+e_{pp})\ \ ((1+e_{pp})\,(\mathbf{g}\cdot\mathbf{k})\ \ k_ik_j - (k_ig_j + k_jg_i)) \tag{C.7}$$

with $\mathbf{g} = \mathbf{c_1} - \mathbf{c_2}$ and $\mathbf{k} = \mathbf{x_2} - \mathbf{x_1}$. We can then derive the expressions for χ_{ij} and Θ_{ij}. The only modification of the study of Jenkins and Richman (1985) is that e_{pp} is now a function of $(\mathbf{g}\cdot\mathbf{k})$:

$$e_{pp} = e_0\ exp(-\frac{V_\beta}{\mathbf{g}\cdot\mathbf{k}}) \tag{C.8}$$

where $V_\beta = \frac{\beta}{2}\frac{a}{\tau_p}$. Integrating the collisional terms χ_{ii}, χ_{22}, χ_{12}, Θ_{22} and Θ_{12} gives:

$$\chi_{ii} = -T\ \frac{\phi\ \rho_p}{\tau_c}\ \left(1-(R_{32}\ e_0)^2\right) \tag{C.9}$$

$$\begin{aligned}
\chi_{33} &= \frac{1}{3}\ \frac{\phi\ \rho_p}{\tau_c}\ T\ \left(1+2\ R_{31}\ e_0+(R_{32}\ e_0)^2\right) - \frac{2}{3}\ \frac{\phi\ \rho_p}{\tau_c}\ T\ \ (1+R_{31}\ e_0)\\
&+ \frac{4}{15}\ \frac{\phi\ \rho_p}{\tau_c}\ \hat{T}_{33}\ \left(1+2\ R_{51}\ e_0+(R_{52}\ e_0)^2\right)\\
&- \frac{1}{15}\ \frac{\phi\ \rho_p}{\tau_c}\ \hat{T}_{33}\ \left(1+2\ R_{31}\ e_0+(R_{32}\ e_0)^2\right)\\
&- \frac{8}{15}\ \frac{\phi\ \rho_p}{\tau_c}\ \hat{T}_{33}\ \ (1+R_{51}\ e_0) - \frac{4}{15}\ \frac{\phi\ \rho_p}{\tau_c}\ \hat{T}_{33}\ \ (1+R_{31}\ e_0)
\end{aligned} \tag{C.10}$$

$$\begin{aligned}
\chi_{13} &= \frac{12}{5}\ \phi\ \rho_p\ \phi\ g_0\ T\ \hat{D}_{p,13}\ \ (2\ (1+R_{41}\ e_0)+(1+R_{21}\ e_0))\\
&- \frac{12}{5}\ \phi\ \rho_p\ \phi\ g_0\ T\ \hat{D}_{p,13}\ \ \left(1+2\ R_{41}\ e_0+(R_{42}\ e_0)^2\right)\\
&+ \frac{4}{15}\ \frac{\phi\ \rho_p}{\tau_c}\ \hat{T}_{13}\ \ \left(1+2\ R_{51}\ e_0+(R_{52}\ e_0)^2\right)\\
&- \frac{1}{15}\ \frac{\phi\ \rho_p}{\tau_c}\ \hat{T}_{13}\ \ \left(1+2\ R_{31}\ e_0+(R_{32}\ e_0)^2\right)\\
&- \frac{8}{15}\ \frac{\phi\ \rho_p}{\tau_c}\ \hat{T}_{13}\ \ (1+R_{51}\ e_0) - \frac{4}{15}\ \frac{\phi\ \rho_p}{\tau_c}\ \hat{T}_{13}\ \ (1+R_{31}\ e_0)
\end{aligned} \tag{C.11}$$

$$\begin{aligned}\Theta_{33} &= 2\ \phi\ \rho_p\ \phi\ g_0\ T\ \ (1 + R_{21}\ e_0) \\ &+ \frac{4}{10}\ \phi\ \rho_p\ \phi\ g_0\ \hat{T}_{33}\ \ (3\ (1 + R_{41}\ e_0) - (1 + R_{21}\ e_0))\end{aligned} \tag{C.12}$$

$$\begin{aligned}\Theta_{13} &= \frac{4}{10}\ \phi\ \rho_p\ \phi\ g_0\ \hat{T}_{13}\ \ (3\ (1 + R_{41}\ e_0) - (1 + R_{21}\ e_0)) \\ &- \frac{16}{5}\ \phi\ \rho_p\ \phi\ g_0\ a\ \sqrt{\frac{T}{\pi}}\ \hat{D}_{p,13}\ \ (1 + R_{31}\ e_0)\end{aligned} \tag{C.13}$$

where $\hat{D}_{p,ij}$ the anisotropic part of the tensor $D_{p,ij} = \frac{1}{2}(\frac{\partial U_{p,i}}{\partial x_j} + \frac{\partial U_{p,j}}{\partial x_i})$ and $\hat{T}_{ij} = T a_{ij}$. R_{np} are functions of $T_\beta = \frac{T}{V_\beta^2}$ defined by:

$$R_{np} = \left(\frac{1}{I_n}\int_0^{+\infty} e^{-p/(2\ T_\beta^{1/2} u)}\ u^n\ e^{-u^2}\ du\right)^{\frac{1}{p}} \tag{C.14}$$

Appendix D

Taylor development for the subgrid drift velocity

Using Taylor expansions, a mathematical expression of the subgrid drift velocity can be written in function of gradient of the filtered values. This method is adapted from works on LES in single phase flows (Clark et al., 1979). Let us consider a variable f which is a function of space and time. A Taylor series expansion of f around $\mathbf{x_0}$ leads to:

$$\begin{aligned} f(\mathbf{x}) \;&\simeq\; f(\mathbf{x_0}) \;+\; \left.\frac{\partial f}{\partial x_i}\right|_{\mathbf{x_0}} (x_i - x_{0,i}) \\ &+\; \frac{1}{2}\left.\frac{\partial^2 f}{\partial x_i \partial x_j}\right|_{\mathbf{x_0}} (x_i - x_{0,i})\,(x_j - x_{0,j}) + \;\ldots \end{aligned} \tag{D.1}$$

Multiplying this expansion by $G(\mathbf{x_0} - \mathbf{x})$ and integrating $\mathbf{x}$ over the whole space leads to:

$$\overline{f} \;\simeq\; f \;+\; \frac{\partial f}{\partial x_i}\,\overline{I}_i \;+\; \frac{1}{2}\frac{\partial^2 f}{\partial x_i \partial x_j}\,\overline{I}_{ij} \;+\; \ldots \tag{D.2}$$

were $\overline{I}_i$ and $\overline{I}_{i,j}$ are defined as follows:

$$\overline{I}_i = \iiint G(\mathbf{u})\; u_i \;\mathbf{du} \tag{D.3}$$

$$\overline{I}_{ij} = \iiint G(\mathbf{u})\; u_i u_j \;\mathbf{du} \tag{D.4}$$

Assuming that the kernel G is an even function, we obtained $\overline{I}_i = 0$ and $\overline{I}_{i,j\neq i} = 0$. Multiplying Eq. D.1 by $G(\mathbf{x_0} - \mathbf{x})\ \alpha_k(\mathbf{x})$ and integrating $\mathbf{x}$ over the whole space leads to:

$$\overline{\alpha_k f} \ \simeq\ \overline{\alpha_k}\ f\ + \frac{\partial f}{\partial x_i}\ \overline{\alpha}_k \widetilde{I}_i^k\ +\ \frac{1}{2}\frac{\partial^2 f}{\partial x_i \partial x_j}\ \overline{\alpha}_k \widetilde{I}_{ij}^k\ +\ \ldots \tag{D.5}$$

were $\widetilde{I}_i^k$ and $\widetilde{I}_{i,j}^k$ are defined as follows:

$$\widetilde{I}_i^k = \frac{1}{\overline{\alpha}_k} \iiint G(\mathbf{u})\ u_i\ \alpha_k(\mathbf{x_0} + \mathbf{u})\ \mathbf{du} \tag{D.6}$$

$$\widetilde{I}_{ij}^k = \frac{1}{\overline{\alpha}_k} \iiint G(\mathbf{u})\ u_i u_j\ \alpha_k(\mathbf{x_0} + \mathbf{u})\ \mathbf{du} \tag{D.7}$$

Performing a taylor series expansion of α_k around $\mathbf{x_0}$ and putting it in Eqs. D.6 and D.7 leads to:

$$\widetilde{I}_i^k \simeq \frac{1}{\overline{\alpha}_k}\frac{\partial \alpha_k}{\partial x_j}\ \overline{I}_{ij}\ +\ \ldots \tag{D.8}$$

$$\widetilde{I}_{ij}^k \simeq \frac{\alpha_k}{\overline{\alpha}_k}\ \overline{I}_{ij}\ +\ \ldots \tag{D.9}$$

Now using Eqs. D.2, D.5, D.8 and D.9 for both α_p, α_g and $U_{g,i}$ leads to the following expressions for $\widetilde{U}_{g,i}$ and $\widetilde{U}_{g@p,i}$:

$$\widetilde{U}_{g,i}\ \simeq\ U_{g,i}\ +\ \frac{1}{\overline{\alpha}_g}\frac{\partial \alpha_g}{\partial x_j}\frac{\partial U_{g,i}}{\partial x_j}\ \overline{I}_{jj}\ +\ \frac{1}{2}\frac{\partial^2 U_{g,i}}{\partial x_j \partial x_j}\ \overline{I}_{jj}\ +\ \ldots \tag{D.10}$$

$$\widetilde{U}_{g@p,i}\ \simeq\ U_{g,i}\ +\ \frac{1}{\overline{\alpha}_p}\frac{\partial \alpha_p}{\partial x_j}\frac{\partial U_{g,i}}{\partial x_j}\ \overline{I}_{jj}\ +\ \frac{1}{2}\frac{\partial^2 U_{g,i}}{\partial x_j \partial x_j}\ \overline{I}_{jj}\ +\ \ldots \tag{D.11}$$

Then subtracting Eq. D.10 to Eq. D.11 leads to the following expression for the drift velocity:

$$\overline{\alpha}_p\ \overline{\alpha}_g\ \widetilde{V}_{d,i} =\ \frac{\overline{\Delta}^2}{12}\ \frac{\partial \alpha_p}{\partial x_j}\ \frac{\partial U_{g,i}}{\partial x_j}\ +\ O(\overline{\Delta}^4) \tag{D.12}$$

where the characteristic length scale $\overline{\Delta}$ is defined by:

$$\overline{\Delta}^2 = 12\ I_{11} = 12\ I_{22} = 12\ I_{33} \tag{D.13}$$

In the case of the continuous box or top-hat filter definied as follows:

$$G(\mathbf{u}) = \begin{cases} 1/\Delta_B^3 & \text{if } max(u_x, u_y, u_z) < \Delta_B/2 \\ \\ 0 & \text{otherwise} \end{cases} \tag{D.14}$$

we have:

$$\overline{I}_{11} = \overline{I}_{22} = \overline{I}_{33} = \frac{1}{12}\ \Delta_B^2 = \frac{1}{12}\ \overline{\Delta}^2 \tag{D.15}$$

In the case of the spectral cut-off filter, Eq. D.2 and so on model Eq. D.12 are not valid since $\overline{I}_{11} = \overline{I}_{22} = \overline{I}_{33} = \infty$. In the case of the discrete version of the box filter, as defined in section 3.5, we have:

$$\overline{\Delta}^2 = \Delta_B^2\ \left(1 - \left(\frac{\Delta_D}{\Delta_B}\right)^2\right) \tag{D.16}$$

Appendix E

Inverse scale similarity models

E.1 Inverse Bardina model

The Bardina model in LES of single phase turbulent flows can be seen as a model where the velocity $\mathbf{u}$ is approximated by the filtered velocity $\overline{\mathbf{u}}$ in the subgrid tensor τ_{ij}:

$$\mathbf{u} \simeq \overline{\mathbf{u}} \;\Rightarrow\; \overline{u_i\,u_j} - \overline{u}_i\,\overline{u}_j \;\simeq\; \overline{\overline{u}_i\,\overline{u}_j} - \overline{\overline{u}}_i\overline{\overline{u}}_j \tag{E.1}$$

This is a second order approximation. A same order approximation can be directly made on the subgrid tensor:

$$\tau_{i,j} \simeq \overline{\tau}_{i,j} \;\Rightarrow\; \overline{\overline{u_i\,u_j}} - \overline{\overline{u}_i\,\overline{u}_j} \;\simeq\; \overline{u_i\,u_j} - \overline{u}_i\,\overline{u}_j \tag{E.2}$$

By noting $\widehat{(.)}$ the inverse of $\overline{(.)}$ (such as $\forall\phi,\ \phi = \widehat{\overline{\phi}}$) we get from Eq. E.2:

$$\overline{u_i\,u_j} - \overline{u}_i\,\overline{u}_j \;\simeq\; \widehat{\overline{u_i\,u_j}} - \widehat{\overline{u}_i\,\overline{u}_j} \tag{E.3}$$

Then, introducing $\widehat{\overline{\mathbf{u}}}$ in Eq. E.3 such as to see the Germano identity Germano (1992):

$$\overline{u_i\,u_j} - \overline{u}_i\,\overline{u}_j \;\simeq\; (\widehat{\overline{u_i\,u_j}} - \widehat{\overline{u}}_i\,\widehat{\overline{u}}_j) - (\widehat{\overline{u}_i\,\overline{u}_j} - \widehat{\overline{u}}_i\,\widehat{\overline{u}}_j) \tag{E.4}$$

As $\widehat{(.)}$ is the inverse of $\overline{(.)}$ we have:

$$\widehat{\overline{u_i\,u_j}} - \widehat{\overline{u}}_i\,\widehat{\overline{u}}_j = u_i\,u_j - u_i\,u_j = 0 \tag{E.5}$$

Finally, reporting Eq. E.5 in Eq. E.4, we get what we call the inverse Bardina model:

$$\overline{u_i\,u_j} - \overline{u}_i\,\overline{u}_j \;=\; -\,(\widehat{\overline{u}_i\,\overline{u}_j} - \widehat{\overline{u}}_i\,\widehat{\overline{u}}_j) \tag{E.6}$$

in reference to the original Bardina model:

$$\overline{u_i\,u_j} - \overline{u}_i\,\overline{u}_j \;=\; \overline{\overline{u}_i\,\overline{u}_j} - \overline{\overline{u}}_i\,\overline{\overline{u}}_j \tag{E.7}$$

The original Bardina model is based on a second application of the implicit filter. The inverse Bardina model is based on the application of the inverse of the implicit filter. Moreover the constant of similitude is found to be equal to -1 in the inverse Bardina model instead of 1 in the original form.

The application of the inverse Bardina model to the subgrid drift tensor leads to:

$$\overline{\alpha_p\,U_{g,i}} - \overline{\alpha}_p\,\overline{U}_{g,i} = -\,(\widehat{\overline{\alpha}_p\,\widetilde{U}_{g,i}} - \widehat{\overline{\alpha}}_p\,\widehat{\widetilde{U}}_{g,i}) \tag{E.8}$$

E.2 Inverse LMK model

The corresponding LMK model, called the inverse LMK model, writes as follow:

$$\tau_i = C_s\,(\widehat{\overline{\alpha}_p\,\widetilde{U}_{g,i}} - \widehat{\overline{\alpha}}_p\,\widehat{\widetilde{U}}_{g,i}) \tag{E.9}$$

where $\widehat{(.)}$ is a test filter that amplify high frequencies ($\widehat{\Delta} < 0$), and $C_s < 0$ is the constant of similitude.

Negatives values of C_f in Eq. 5.20 lead to a test filter that amplify the high frequencies, as shown in Figure E.2. Moreover, test filter defined by Eq. 5.20 verifies:

$$\widehat{G}_k(-C_f) = 1 + (1 - \widehat{G}_k(C_f)) \tag{E.10}$$

that can be interpreted as a second order development of the Van Cittert (1931) method that gives the inverse of a filter:

$$G^{-1} = \sum_{p=0}^{\infty} (Id - G)^p = Id + (Id - G) + \cdots \tag{E.11}$$

As $\widehat{G}$ with $C_f > 0$ is an approximation of the implicit filter $\overline{G}$, $\widehat{G}$ with $C_f < 0$ is an approximation of $\overline{G}^{-1}$. By noting $\widehat{Q}_k = \widehat{G}_k$ for $C_f < 0$, we have $\widehat{Q}_k \cdot \overline{G}_k \simeq 1$. Figure E.2 compares the product $\widehat{Q}_k \cdot \overline{G}_k$ to the identity function for different values of $C_f < 0$.

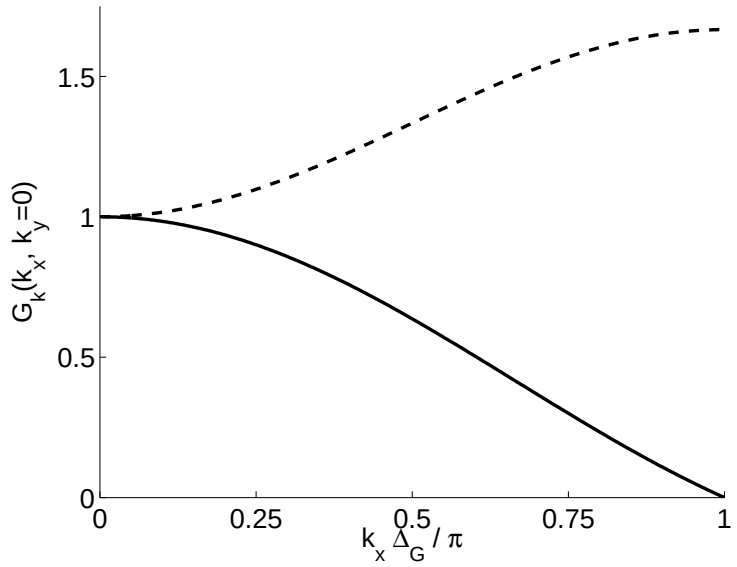

Figure E.1: Transfert functions. —— : implicit filter, - - - : $C_f = -1/6$.

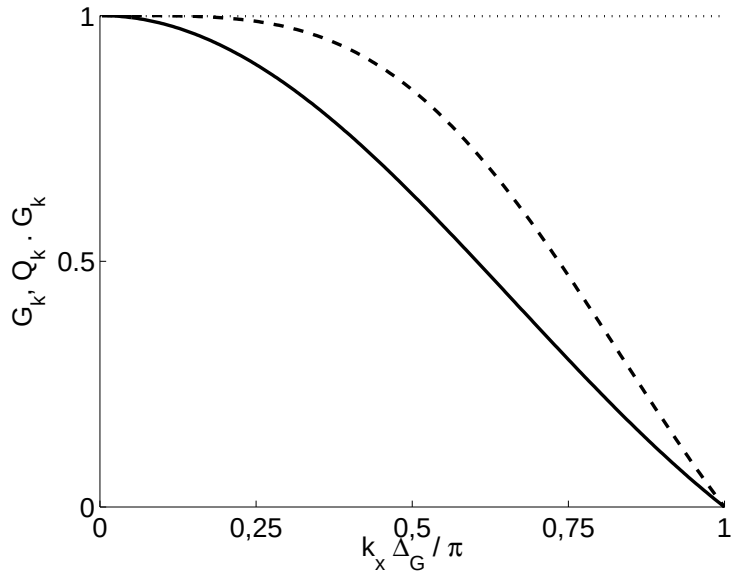

Figure E.2: Transfert functions. —— : implicit filter $\overline{G}_k$, - - - : $\widehat{Q}_k \cdot \overline{G}_k$ for $C_f = -1/6$, ····· : identity function.

Consequently, using test filter defined by Eq. 5.20 with $C_f < 0$ are practical implementations of inverse LMK model. Hence constants of similitude C_s are found to be negative.

Bibliography

Abbas, M., Climent, E., Parmentier, J. F. and Simonin, O. (2010), 'Flow of particles suspended in a sheared viscous fluid: Effects of finite inertia and inelastic collisions', *AIChE Journal* (in Press).

Abbas, M., Climent, E. and Simonin, O. (2009), 'Shear-induced self-diffusion of inertial particles in a viscous fluid', *Physical Review E* **79**(3), 36313.

Agrawal, K., Loezos, P. N., Syamlal, M. and Sundaresan, S. (2001), 'The role of meso-scale structures in rapid gas–solid flows', *Journal of Fluid Mechanics* **445**, 151–185.

Allen, M. P. and Tildesley, D. J. (1990), *Computer simulation of liquids*, Oxford University Press, USA.

Andrews IV, A. T., Loezos, P. N. and Sundaresan, S. (2005), 'Coarse-grid simulation of gas-particle flows in vertical risers', *Ind. Eng. Chem. Res* **44**(16), 6022–6037.

Balzer, G., Boelle, A. and Simonin, O. (1995), 'Eulerian gas-solid flow modelling of dense fluidized bed', *Fluidization* **8**, 1125.

Bardina, J., Ferziger, J. H. and Reynolds, W. C. (1983), Improved turbulence models based on large eddy simulation of homogeneous, incompressible, Technical report, turbulent flows. Tech. Rep. TF-19, Department of Mechanical Engineering, Stanford University.

Beetstra, R., Van der Hoef, M. A. and Kuipers, J. A. M. (2007), 'Drag force of intermediate Reynolds number flow past mono-and bidisperse arrays of spheres', *AIChE Journal* **53**(2), 489–501.

Boelle, A., Balzer, G. and Simonin, O. (1995), 'Particle-phase stress tensor with gas influence in simple shear dense suspensions', *Gas-Particle Flows, FED* **228**.

Campbell, C. S. (1990), 'Rapid granular flows', *Annual Review of Fluid Mechanics* **22**(1), 57–90.

Carnahan, N. F. and Starling, K. E. (1969), 'Equation of state for nonattracting rigid spheres', *The Journal of Chemical Physics* **51**, 635.

Chang, H. and Louge, M. (1992), 'Fluid dynamic similarity of circulating fluidized beds', *Powder Technology* **70**(3), 259–270.

Chapman, S. and Cowling, T. G. (1970), *The mathematical theory of non-uniform gases*, Cambridge University Press.

Clark, R. A., Ferziger, J. H. and Reynolds, W. C. (1979), 'Evaluation of subgrid-scale models using an accurately simulated turbulent flow', *Journal of fluid mechanics* p. 1.

De Wilde, J. (2005), 'Reformulating and quantifying the generalized added mass in filtered gas-solid flow models', *Physics of fluids* **17**, 113304.

De Wilde, J. (2007), 'The generalized added mass revised', *Physics of fluids* **19**, 058103.

Deen, N. G., Van Sint Annaland, M., Van der Hoef, M. A. and Kuipers, J. A. M. (2007), 'Review of discrete particle modeling of fluidized beds', *Chemical Engineering Science* **62**(1-2), 28–44.

Detamore, M. S., Swanson, M. A., Frender, K. R. and Hrenya, C. M. (2001), 'A kinetic-theory analysis of the scale-up of circulating fluidized beds', *Powder technology* **116**(2-3), 190–203.

Ding, J. and Gidaspow, D. (1990), 'A bubbling fluidization model using kinetic theory of granular flow', *AIChE Journal* **36**(4), 523–538.

Elimelech, M., Williams, R., Gregory, J. and Jia, X. (1998), *Particle deposition and aggregation: measurement, modelling and simulation*, Butterworth-Heinemann.

Ergun, S. (1952), 'Fluid flow through packed columns', *Chem. Eng. Prog* **48**(2), 89–94.

Ferschneider, G. and Mege, P. (1996), 'Eulerian simulation of dense phase fluidized beds', *Oil & Gas Science and Technology* **51**(2), 301–307.

Gao, J., Lan, X., Fan, Y., Chang, J., Wang, G., Lu, C. and Xu, C. (2009), 'CFD modeling and validation of the turbulent fluidized bed of FCC particles', *AIChE Journal* **55**(7).

Geldart, D. (1973), 'Types of gas fluidization', *Powder Technology* **7**(5), 285–292.

Germano, M. (1986), 'A proposal for a redefinition of the turbulent stresses in the filtered Navier–Stokes equations', *Physics of Fluids* **29**, 2323.

Germano, M. (1992), 'Turbulence: the filtering approach', *Journal of Fluid Mechanics* **238**, 325–336.

Germano, M., Piomelli, U., Moin, P. and Cabot, W. H. (1991), 'A dynamic subgrid-scale eddy viscosity model', *Physics of Fluids A: Fluid Dynamics* **3**, 1760.

Gibilaro, L. G., Di Felice, R., Waldram, S. P. and Foscolo, P. U. (1985), 'Generalized friction factor and drag coefficient correlations for fluid-particle interactions', *Chemical engineering science* **40**(10), 1817–1823.

Gidaspow, D. (1994), *Multiphase flow and fluidization: continuum and kinetic theory descriptions*, Academic Pr.

Gidaspow, D., Bezburuah, R. and Ding, J. (1992), Hydrodynamics of circulating fluidized beds: Kinetic theory approach, *in* 'Fluidization VII: proceedings of the Seventh Engineering Foundation Conference on Fluidization, May 3-8, 1992, Brisbane, Australia', Amer Inst of Chemical Engineers, p. 75.

Glicksman, L. R. (1984), 'Scaling relationships for fluidized beds', *Chemical engineering science* **39**(9), 1373–1379.

Glicksman, L. R., Hyre, M. R. and Farrell, P. A. (1994), 'Dynamic similarity in fluidization', *International Journal of Multiphase Flow* **20**, 331–386.

Glicksman, L. R., Hyre, M. and Woloshun, K. (1993), 'Simplified scaling relationships for fluidized beds', *Powder Technology* **77**(2), 177–199.

Grad, H. (1949), 'On the kinetic theory of rarefied gases', *Comm. Pure Appl. Math* **2**(4), 331–407.

He, X. and Doolen, G. D. (2002), 'Thermodynamic foundations of kinetic theory and lattice Boltzmann models for multiphase flows', *Journal of Statistical Physics* **107**(1), 309–328.

Heynderickx, G. J., Das, A. K., De Wilde, J. and Marin, G. B. (2004), 'Effect of Clustering on Gas- Solid Drag in Dilute Two-Phase Flow', *Ind. Eng. Chem. Res* **43**(16), 4635–4646.

Hill, R. J., Koch, D. L. and Ladd, A. J. C. (2001), 'Moderate-Reynolds-number flows in ordered and random arrays of spheres', *Journal of Fluid Mechanics* **448**, 243–278.

Hoomans, B. P. B., Kuipers, J. A. M., Briels, W. J. and Van Swaaij, W. P. M. (1996), 'Discrete particle simulation of bubble and slug formation in a two-dimensional gas-fluidised bed: a hard-sphere approach', *Chemical Engineering Science* **51**(1), 99–118.

Horio, M., Ishii, H., Kobukai, Y. and Yamanishi, N. (1989), 'A scaling law for circulating fluidized beds', *Journal of Chemical Engineering of Japan* **22**(6), 587–592.

Horio, M., Nonaka, A., Sawa, Y. and Muchi, I. (2004), 'A new similarity rule for fluidized bed scale-up', *AIChE Journal* **32**(9), 1466–1482.

Hosseini, S. H., Rahimi, R., Zivdar, M. and Samimi, A. (2009), 'CFD simulation of gas-solid bubbling fluidized bed containing FCC particles', *Korean Journal of Chemical Engineering* **26**(5), 1405–1413.

Igci, Y., Andrews IV, A. T., Sundaresan, S., Pannala, S. and O'Brien, T. (2008), 'Filtered two-fluid models for fluidized gas-particle suspensions', *AIChE Journal* **54**(6).

Jenkins, J. T. and Richman, M. W. (1985), 'Grad's 13-moment system for a dense gas of inelastic spheres', *Archive for Rational Mechanics and Analysis* **87**(4), 355–377.

Joseph, G. G., Zenit, R., Hunt, M. L. and Rosenwinkel, A. M. (2001), 'Particle–wall collisions in a viscous fluid', *Journal of Fluid Mechanics* **433**, 329–346.

Kuipers, J. A. M., Van Duin, K. J., Van Beckum, F. P. H. and Van Swaaij, W. P. M. (1992), 'A numerical model of gas-fluidized beds', *Chemical Engineering Science* **47**(8), 1913–1924.

Kunii, D. and Levenspiel, O. (1991), *Fluidization engineering*, Butterworth-Heinemann.

Legendre, D., Zenit, R., Daniel, C. and Guiraud, P. (2006), 'A note on the modelling of the bouncing of spherical drops or solid spheres on a wall in viscous fluid', *Chemical Engineering Science* **61**(11), 3543–3549.

Lele, S. K. (1992), 'Compact finite difference schemes with spectral-like resolution', *Journal of Computational Physics* **103**(1), 16–42.

Li, J. and Kuipers, J. A. M. (2003), 'Gas-particle interactions in dense gas-fluidized beds', *Chemical Engineering Science* **58**(3-6), 711–718.

Li, J. and Kwauk, M. (1994), *Particle-fluid two-phase flow: The energy-minimization multi-scale method*, Metallurgical Industry Press: Beijing, P.R. China.

Lilly, D. K. (1992), 'A proposed modification of the Germano subgrid-scale closure method', *Physics of Fluids A: Fluid Dynamics* **4**, 633.

Liu, S., Meneveau, C. and Katz, J. (2006), 'On the properties of similarity subgrid-scale models as deduced from measurements in a turbulent jet', *Journal of Fluid Mechanics* **275**, 83–119.

Lun, C. K. K., Jeffrey, D. J., Savage, S. B. and Chepurniy, N. (1984), 'Kinetic theories for granular flow: inelastic particles in Couette flow and slightly inelastic particles in a general flowfield', *Journal of Fluid Mechanics* **140**, 223–56.

Lun, C. K. K. and Savage, S. B. (1986), 'The effects of an impact velocity dependent coefficient of restitution on stresses developed by sheared granular materials', *Acta Mechanica* **63**(1), 15–44.

Makkawi, Y. T., Wright, P. C. and Ocone, R. (2006), 'The effect of friction and inter-particle cohesive forces on the hydrodynamics of gas–solid flow: A comparative analysis of theoretical predictions and experiments', *Powder Technology* **163**(1-2), 69–79.

McKeen, T. and Pugsley, T. (2003), 'Simulation and experimental validation of a freely bubbling bed of FCC catalyst', *Powder Technology* **129**(1-3), 139–152.

Oltrogge, R. D. (1972), Gas fluidized beds of fine particles, PhD thesis, University of Michigan.

Peirano, E., Delloume, V. and Leckner, B. (2001), 'Two- or three-dimensional simulations of turbulent gas–solid flows applied to fluidization', *Chemical Engineering Science* **56**(16), 4787–4799.

Richardson, J. F. and Zaki, W. N. (1954), 'Sedimentation and fluidisation: Part I', *Chemical Engineering Research and Design* **32**(a), 35–53.

Sagaut, P. (2001), *Large Eddy Simulation for Incompressible Flows*, Springer-Verlag Berlin Heidelberg, Tiergartenstrasse 7, Postfach 10 51 60, Heidelberg, D-6900, Germany,.

Sangani, A. S., Mo, G., Tsao, H. K. and Koch, D. L. (1996), 'Simple shear flows of dense gas-solid suspensions at finite Stokes numbers', *Journal of Fluid Mechanics* **313**, 309–341.

Smagorinsky, J. (1963), 'General circulation experiments with the primitive equations', *Monthly weather review* **91**(3), 99–164.

Syamlal, M. and O'Brien, T. J. (1989), Computer simulation of bubbles in a fluidized bed, *in* 'AIChE Symp. Ser', Vol. 85, pp. 22–31.

Tsao, H. K. and Koch, D. L. (1995), 'Simple shear flows of dilute gas-solid suspensions', *Journal of Fluid Mechanics* **296**, 211–246.

Tsuji, Y., Kawaguchi, T. and Tanaka, T. (1993), 'Discrete particle simulation of two-dimensional fluidized bed', *Powder Technology* **77**(1), 79–87.

Van Cittert, P. H. (1931), 'Effect of slit width upon distribution of intensity in spectral lines, Part II', *Z. Phys* **69**, 298–308.

Van der Hoef, M. A., Beetstra, R. and Kuipers, J. A. M. (2005), 'Lattice-Boltzmann simulations of low-Reynolds-number flow past mono-and bidisperse arrays of spheres: results for the permeability and drag force', *Journal of fluid mechanics* **528**, 233–254.

Van der Hoef, M. A., Ye, M., van Sint Annaland, M., Andrews, A. T., Sundaresan, S. and Kuipers, J. A. M. (2006), 'Multiscale modeling of gas-fluidized beds', *Advances in Chemical Engineering* **31**, 66.

Van Wachem, B. G. M., Schouten, J. C., Van den Bleek, C. M., Krishna, R. and Sinclair, J. L. (2001), 'Comparative analysis of CFD models of dense gas–solid systems', *AIChE Journal* **47**(5), 1035–1051.

Wang, J. (2009), 'A Review of Eulerian Simulation of Geldart A Particles in Gas-Fluidized Beds', *Industrial Engineering Chemistry Research* **48**, 5567–5577.

Wang, J., Ge, W. and Li, J. (2008), 'Eulerian simulation of heterogeneous gas-solid flows in CFB risers: EMMS-based sub-grid scale model with a revised cluster description', *Chemical Engineering Science* **63**(6), 1553–1571.

Wang, J. and Liu, Y. (2010), 'Emms-based eulerian simulation on the hydrodynamics of a bubbling fluidized bed with fcc particles', *Powder Technology* **197**(3), 241 – 246.

Wang, J., Van der Hoef, M. A. and Kuipers, J. A. M. (2009), 'Why the two-fluid model fails to predict the bed expansion characteristics of Geldart A particles in gas-fluidized beds: A tentative answer', *Chemical Engineering Science* **64**(3), 622–625.

Wang, J., van der Hoef, M. A. and Kuipers, J. A. M. (2010), 'Coarse grid simulation of bed expansion characteristics of industrial-scale gas-solid bubbling fluidized beds', *Chemical Engineering Science* **65**(6), 2125 – 2131.

Wang, W. and Li, J. H. (2007), 'Simulation of gas-solid two-phase flow by a multi-scale CFD approach-Extension of the EMMS model to the sub-grid level', *Chemical Engineering Science* **62**(1-2), 208–231.

Wen, C. Y. and Yu, Y. H. (1966), Mechanics of fluidization, *in* 'Chem. Eng. Prog. Symp. Ser', Vol. 62, pp. 100–111.

Xie, H. Y. (1997), 'The role of interparticle forces in the fluidization of fine particles', *Powder Technology* **94**(2), 99–108.

Yang, F. L. and Hunt, M. L. (2006), 'Dynamics of particle-particle collisions in a viscous liquid', *Physics of Fluids* **18**, 121506.

Yang, W. C. (2007), 'Modification and re-interpretation of Geldart's classification of powders', *Powder Technology* **171**(2), 69–74.

Ye, M., Van der Hoef, M. A. and Kuipers, J. A. M. (2004), 'A numerical study of fluidization behavior of Geldart A particles using a discrete particle model', *Powder Technology* **139**(2), 129–139.

Ye, M., Van der Hoef, M. A. and Kuipers, J. A. M. (2005*a*), 'From discrete particle model to a continuous model of Geldart A particles', *Chemical Engineering Research and Design* **83**(7), 833–843.

Ye, M., Van der Hoef, M. A. and Kuipers, J. A. M. (2005*b*), 'The effects of particle and gas properties on the fluidization of Geldart A particles', *Chemical engineering science* **60**(16), 4567–4580.

Zhang, D. Z. and VanderHeyden, W. B. (2002), 'The effects of mesoscale structures on the macroscopic momentum equations for two-phase flows', *International Journal of Multiphase Flow* **28**(5), 805–822.

Zimmermann, S. and Taghipour, F. (2005), 'CFD modeling of the hydrodynamics and reaction kinetics of FCC fluidized-bed reactors', *Ind. Eng. Chem. Res* **44**(26), 9818–9827.